ABSTRACT

Title of Document: SILICON NANOCRYSTALS: BIOCOMPATIBLE FLUORESCENT NANOLABEL

Jonghoon Choi, Doctor of Philosophy, 2008

Directed By: Associate Professor, Nam Sun Wang, Department of Chemical and Biomolecular Engineering

This study discusses a synthesis, characterization, bioconjugation, and biological responses of fluorescent silicon nanocrystals (SiNCs).

First, the efficient method of synthesizing fluorescent SiNCs is presented employing an electrochemical reduction of trichloro(octyl)silane. Miligram amount of bright fluorescent SiNCs is obtained with well-defined nanocrystalline structures. Octyl passivation of the surface provides SiNCs a monodispersity, hydrophobicity and physical stability.

Second, physical and chemical characteristics of synthesized SiNCs are described based on the nanoparticle size and surface chemistry information measured by different techniques: transmission electron microscopy (TEM), X-ray energy dispersive spectroscopy (EDX), X-ray powder diffraction (XRD), dynamic light

scattering (DLS), UV-VIS absorption spectroscopy (Abs), photoluminescence spectroscopy (PL), and Fourier Transform Infrared spectroscopy (FT-IR).

Next, potential applications of SiNCs as a fluorescent nanolabel are highlighted by studying the covalent, multiple attachments of fluorescent SiNCs to the target biomolecules. Streptavidin is tagged by several SiNCs through covalent linkage while it retains its characteristic affinity to biotin molecules. SiNCs-Streptavidin-biotin complexes are characterized by FT-IR spectroscopy for each step of conjugation. SiNCs retain their brightness of blue fluorescence after the final conjugation with biotinylated microbeads.

Finally, biological responses of SiNCs are assessed by *in vitro* assay experiments with murine macrophages. Cytotoxicity of SiNCs is not pronounced until their concentration reaches up to 20 μg/ml. Inflammatory responses of SiNCs are not activated because of their small size (< 5nm in diameter) which allows them pass through the macrophage's defense mechanism. SiNCs penetrate the macrophage cells by pinocytosis and are observed by fluorescence microscopy and optical Z-stacks.

Presented studies on the synthesis, characterizations, bio-tagging, and biological responses of SiNCs will benefit research in broad areas of nano-bio science and facilitate the development of small, bright, biocompatible, and multifunctional nanolabels for biological applications.

SILICON NANOCRYSTALS: BIOCOMPATIBLE FLUORESCENT NANOLABEL

By

Jonghoon Choi.

Dissertation submitted to the Faculty of the Graduate School of the
University of Maryland, College Park, in partial fulfillment
of the requirements for the degree of
Doctor of Philosophy
2008

Advisory Committee:
Associate Professor Nam Sun Wang, Chair
Associate Professor Sheryl H. Ehrman
Associate Professor Srinivasa R. Raghavan
Associate Professor John P. Fisher
Dr. Vytautas Reipa (NIST)

Foreword

"It is only with the heart that one can see rightly;
what is essential is invisible to the eye"

-Antoine de Saint-Exupery

Dedication

To my beloved family, and Jesus Christ my savior

Acknowledgements

Past four years feels like a glimpse of time to me. Lots of good and bad things have happened but whether they were good or bad memories, they have benefited my life in US. It is a great pleasure of me to look back past four years and remember the days that I suffered as well as laughed. I truly believe that without the support of my family, friends, colleagues, and Jesus Christ, I couldn't have made it through here. I would like to acknowledge all those loved ones here and thank you all for trusting and supporting me.

During my Ph. D. study, I was in very unusual situation that I have three thesis co-advisors in three different institutions. I cannot help acknowledging these three great mentors and experts in different fields that I have had. First of all, I'd like to thank my advisor at University of Maryland, Prof. Nam Sun Wang for his advice and mentoring during my M.S. and Ph. D. studies. I have learned a lot in many respects from his warm and friendly attitude toward other people. Second, I'd like to acknowledge another advisor and good colleague at National Institute of Standards and Technology, Dr. Vytas Reipa for his invaluable support, and advice not only on the researches we had but also on many memories we shared for past three years. The last but not least, I'd like to thank my advisor at Food and Drug Administration, Dr. Vickie Hitchins for her mentoring and helps. Her energetic and joyful attitudes made everyone, especially myself, feel comfortable in and out side the lab. I am really fortunate to have them as my advisors, mentors and friends.

I'd like to thank to all my colleagues at NIST and FDA for their support. I could gain lots of experiences and skills while I worked with them that I may not learn from a

textbook. Sharing ideas and spending time together with you friends are always full of fun!

To all my Korean friends in Maryland and Virginia, I would like to appreciate you all for good memories we share and your continuous support. I'd like to thank you KBS and KUMC brothers and sisters for sharing life together and being each other's light house in our lives. To my family in Korea, I do and will always love you all. Finally, I thank Jesus Christ for his immortal love and being the Lord of our lives all the time.

Table of Contents

List of Figures

Figure 1.4 Photoluminescence spectra of tryptophan and silicon nanoparticles excited at 270 nm. Each spectra curve has been fitted with log normal distribution to integrate the area below the curves to calculate total amount of photons emitted.

Figure 1.5 (A) - TEM image, showing spherical, well dispersed SiNCs. (B) - particle size distribution histogram, acquired from (A). (C) - X-ray energy dispersive spectra of SiNCs.

Figure 1.6 (A) - high resolution transmission electron microscopy (HrTEM) image of electrochemically reduced silicon nanocrystals. Scale bar is 5 nm. (B) - electron diffraction pattern, confirming the nanocrystalline structure. (C) - X-ray diffraction pattern of the dried SiNC powder.

Figure 1.7 Fast Fourier Transform (FFT) analysis of HrTEM images (A). Yellow box (256 x 256 pixels) was used for the lattice fringe spacing calculation. A distance between the two points of the FFT image (yellow arrow) in the diffractogram was then used to calculate the distance between fringes (3.14 ± 0.04 Å).

Figure 1.8 Electron diffraction patterns of SiNCs. Inner most ring corresponds to 3.10 ± 0.02 Å lattice spacing, which fits well Si (1 1 1) structure. Second ring (lattice spacing = 1.89 ± 0.03 Å) is very close to the silicon (2 2 0) lattice structure. Third ring (Lattice spacing = 1.66 ± 0.03 Å) was assigned to Si (3 1 1).

Figure 1.9 Optical property and surface chemistry of electrochemically reduced silicon nanoparticles: (A) - Normalized photoluminescence spectra of SiNCs. Inset shows a fluorescence image of silicon nanocrystal suspension under 365 nm illumination. (B) – infrared spectrum of dry SiNCs.

Figure 2.1 Schematic representation of the silicon nanocrystal and protein molecule covalent conjugation. (a) - octane attachment to SNs, (b) – bi-functional cross-linker (ATFB, SE) reaction with the octane methyl groups, (c) – amide bond formation between the streptavidin and activated crosslinker, (d) – test of the SN-streptavidin complex functionality by exposing it to the biotinylated polystyrene microbeads.

Figure 2.2 Photoluminescence spectra of freshly prepared silicon nanoparticles in toluene – (a), following octane surface derivatization - (b), and streptavidin conjugation - (c); λ_{exc} = 340 nm. Insets show the fluorescence images of fresh and derivatized particle under UV excitation.

Figure 2.3 FTIR transmission spectra for dried films of: A – silicon nanoparticles, following the reaction with 1-octene (step a in Fig. 2.1); B – spectrum of pure bi-linker ATFB, SE; C – silicon nanoparticles subsequent to UV assisted reaction with bi-linker (step b in Fig. 2.1), and D –product of the conjugation reaction (step c in Fig. 2.1).

Figure 2.4 Native gel electrophoresis image and fluorescence intensity profiles from the eluted bands of neat streptavidin - (a), and SN - streptavidin conjugates - ((b), (c) and (d)). Variation of elution times between (b), (c) and (d) wells reflect different relative concentrations of the crosslinker tagged SNs to the streptavidin in the final reaction mix (v:v); (b) 1:2, (c) 1:1, and (d) 2:1. Electrophoresis conditions: U = 200V, t = 2 h. Mobile buffer: Tris-HCl, pH 8.0. Peaks between 8 to 9 represent neat streptavidin, and from 12 to 14 - conjugation products.

Figure 2.5 Capillary electrophoresis analysis of silicon nanoparticle/streptavidin conjugation reactants: (a) SNs with attached hetero bi-functional crosslinker (ATFB, SE), (b) neat streptavidin, (c) SN-streptavidin conjugate. Inset shows the elution of a neutral molecule (Mesityl oxide, see text). Running buffer: Tris-glycine 0.2 M, pH 8, capillary dimensions: L = 50 cm, ID = 0.1 mm. Applied voltage: U = 20 kV, absorbance detector at 200 nm.

Figure 2.6 Fluorescence microscopy images of 2μm diameter biotinylated polystyrene micro beads, following their exposure to silicon nanoparticle – streptavidin complex: (a) - biotinylated polystyrene beads, exposed to the neat streptavidin (control) - phase image, and (b) - fluorescence image; (c) polystyrene beads exposed to a silicon nanoparticle-streptavidin complex - phase image, and (d) - fluorescence image.

Figure 3.1 (A) FT-IR spectra of silicon nano- and microparticles. Silicon oxide band (~1038 cm^{-1}) was dominant in both nano- and microparticle spectra after thermal sterilization. (B) Photoluminescence spectra and images of silicon nanoparticles before (a) and after (b) 300 °C thermal treatment.

Figure 3.2 (A) High resolution transmission electron microscopy (HrTEM) of thermal treated Si nanoparticles. (B) Energy dispersive X-ray spectroscopy (EDS) of Si nanoparticles shown in (A) for an analysis of the elemental composition Spectra contained intense Si (1.74 keV), O (0.53 keV) and TEM substrate Cu (0.83, 8.05, and 8.90 keV) peaks. (C) Size distribution histograms obtained from the dynamic light scattering measurements of Si nano and microparticles.

Figure 3.3 Effect of SNs and SMs on cell survival percentage in RAW 264.7 cells based on trypan blue dye exclusion (A) and MTT (B) assay. Cells were treated with different concentrations (0.1-200 μg/ml) of SNs and SMs for 24 and 48 h. At the end of exposure period, trypan blue stain was added to an aliquot of cells to assess the cell live/dead ratio (A). MTT was introduced into wells containing cells incubated for 24h or 48 hr with SNs or SMs measured with a fluorescence plate reader. * and $^{\#}$ indicate a statistical difference from the control, $p<0.05$.

Figure 3.4 (A) NO production in RAW macrophages treated with SNs or SMs with and without LPS. NO secretion in the media was assessed using the DAN nitric oxide fluorescent assay. The white bar shows NO levels for samples without LPS injection, and black bar represents samples with SNs or SMs in the presence of 1 ng/ml LPS.

(B) IL-6 and (C) TNF-α production in RAW 264.7 cells; SNs (1-200 μg/ml) and SMs (1-100 μg/ml) were incubated for 24 hr. * indicates a statistical difference to the levels in the supernatants in the control, $p<0.05$.

Figure 3.5 Phase (i), fluorescence (ii), and combined (iii) images of RAW 264.7 macrophages incubated (24 h) with red fluorescent (λ_{em}. 640 nm) silicon nanoparticles (<4 nm diam.). A: Control (no SNs present), B: SNs ,20 μg/ml, C: SNs, 50 μg/ml; scale bar: 30 μm.

Figure 3.6 Fluorescence images of RAW and L929 Cells with silicon nanoparticles. (A) RAW cells incubated with particles for 24 h, observed with DAPI filter set (~350 nm). (B) RAW cells incubated with particles for 24h, observed with UV filter set (~270 nm). (C) L929 cells incubated with particles for 24h, nucleus stained with DAPI, and observed with DAPI filter set. (D) RAW cells incubated with particles for 1h, nucleus stained with DAPI, and observed with DAPI filter set.

Figure 3.7 Z stack fluorescence image of RAW cells treated with 10 μg/ml Si nanoparticles for 24h. (A) Crossed section (white lines) on the red fluorescence spot is from inside the cell confirmed by side views. (B) 3D rendered images of (A) shows internal association of SNs with RAW cells.

Chapter 1: Study Introduction

1.1 Introduction

Because of the superior photo stability, narrow range of emission, broad excitation wavelength, multiple possibilities of modification, quantum dots have gathered much attention from engineering and scientists who are interested in bio markers, sensors or drug targeting [1]~[8]. Commercially available binary quantum dots from Qdot have been successfully applied for above purposes during the last 10 years and reported in a vast number of literatures. Although quantum dots are useful as a tagging material, they also have several disadvantages. First and the most serious demerits of binary quantum dot is that it is toxic to cells. Most popular components of binary quantum dots are cadmium / serenide which are deleterious to cells. Because of the intrinsic toxicity of binary quantum dot, very thick surface coating is required. The final size of quantum dot is almost twice as thick as the initial core size and hinders the applications of qdots in a cell. Figure 1.1 shows the general structure of binary quantum dots reported by Qdot Company. Another drawback of binary quantum dot is its blinking behavior when a single binary qdot is observed with confocal fluorescent microscope [9][10]. Its blinking behavior hinders the tracking of qdot targeted bio molecule in a bio system.

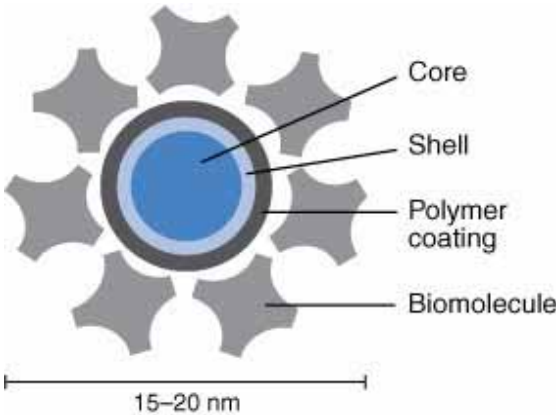

Figure 1.1 Drawing of typical commercially available binary quantum dot. Image courtesy of Invitrogen Co.

Because of drawbacks of binary quantum dots, silicon nanocrystal has been studied to overcome the demerits of commercially available qdots and be used as a substituting fluorophore with traditional organic dyes. Silicon is basically non toxic to cells so that it does not require a thick surface coating to prevent exposure of core to the environment. Therefore, its average size remains close to its core size.

Figure 1.2 compares the size of silicon nanocrystal and binary qdots with various materials. Because of its smaller average sizes (<5 nm in dia.), it can penetrate cell membrane or cell nucleus [2] to use qdots as a bio tagging material inside a bio system. Another important characteristic of silicon nanocrystal is that its blinking behavior is reported to be less problematic. Si nanocrystal is at keeping track of bio conjugates in a system.

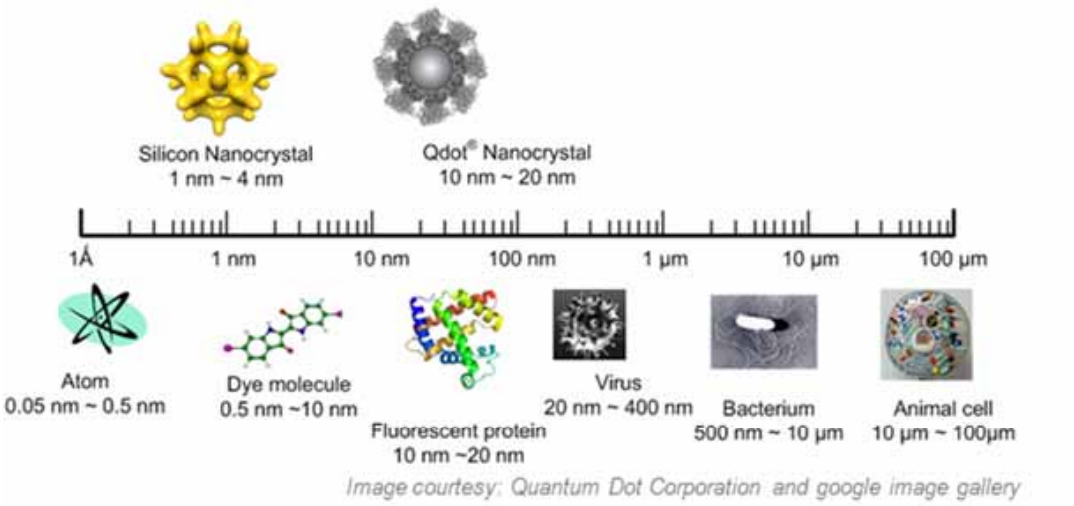

Figure 1.2 Comparison of sizes among silicon nanocrystal and Qdot nanocrystal with other materials. Image courtesy of Invitrogen Co.

Bulk Si is a rather inefficient light emitter due to the indirect-band gap electronic structure, requiring a phonon to balance electron momentum during interband transition. Fortunately, momentum requirements are relaxed in 1-5 nm dia Si crystals as a result of so-called quantum confinement effects that allows for efficient light emission. Silicon nanocrystals are increasingly studied due to their unique physicochemical properties [12] including photoluminescence in the visible part of the electromagnetic spectrum. Significant progress in studying related phenomena in II-VI compound semiconductor quantum dots and successful photonic applications [13][14] have re-energized interests in nanoscale Si, a phenomenon discovered back in the 1950's [15]. First observation of fluorescence from silicon was performed by Lehigh Canham in 1980s. Photoluminescent SN, along with C and SiC based nanoparticles, are considered bio-inert [16] and could lead to the development of smaller biocompatible probes [17][18] that are potentially will facilitate their use in biomedical field. Moreover, SN surface is open to various chemical functionalizations thus offering numerous stabilization and bioconjugation options [19].

Si nanocrystal preparation methods in general are more complicated than the well-established protocols for the II-VI compound based nanoparticles. Published procedures, including chemical synthesis [20], silane chemical [21] or electrochemical [22] reduction, laser assisted pyrolysis [23] and wet Si wafer etching in HF [24], provide milligram quantities of size dispersed Si nanocrystal. A rather straightforward procedure of the electrochemical Si wafer etching [17][24] is based on protocols developed for obtaining nano-porous Si [25]. Anodic wafer etching is followed by sonication that partially crumbles porous Si film, resulting in a

nanoparticle suspension [17]. Immediately after etching, particle surface is hydrogen atom passivated and can be oxidized or substituted by a variety of organic groups using post-etching functionalization [19]. Typically particles of various sizes and shapes are produced during such procedures represented by a wide range of physicochemical properties. Narrow particle size distribution is desirable in most applications due to the strong size dependence of the particle electronic structure when particle diameter is less than 5 nm [26]. Therefore techniques to homogenize Si nanoparticle preparations using centrifugation [26], selective precipitation [27] size exclusion chromatography and capillary electrophoresis [28], are actively pursued.

1.2 Summary of prior work

1.2.1 Synthesis and size control

Our group had reported the synthesis of SNs by the anodic etching of Si wafer followed by the ultrasonication. Etched wafer photoluminescence is tuned by varying etching parameters such as electrolyte composition, current density, or Si doping. However, when the nanoporous film on a surface is converted into nanoparticles, their photoluminescence is highly affected by the solvent. Among non-quenching solvents, most of the PL observed in a fresh particle suspension is in the red-orange spectral range, which indicates that the average diameter of photoluminescent particles is around 3.5~4.5 nm. Hydrogen terminated Si nanoparticle PL wavelength and intensity can be tuned using photo-induced dissolution in a HF/HNO_3 acid mixture (Fig.1.3). By measuring both absorbance and PL during particle dissolution, I have tracked the Si nanoparticle band-gap growth with shrinking crystal size. Etching

of Si nanoparticle methanol suspension in the HF/HNO_3 acid mixture increases PL QY up to 60%. Microsecond PL decay rates are consistent with indirect radiative recombination mechanism in particles exhibiting red to green PL. Together with high quantum yield it implies a slow nonradiative recombination and reflect a relatively defect-free particle structure. Our simple etching procedure can be employed to control particle size and prepare bright Si nanoparticle suspensions with emissions spanning the visible range, required for biological fluorescence tagging (Fig 1.4.).

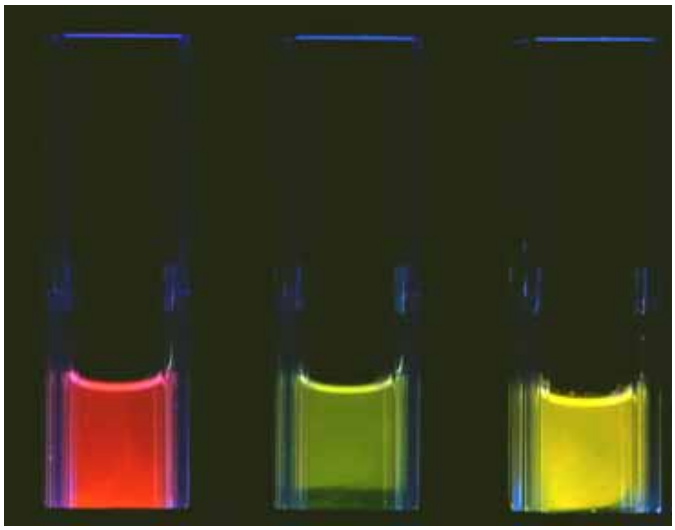

Figure 1.3 Si particle suspension photoluminescence recorded during the various stages of the photo-catalyzed dissolution in the acid mixture. λ_{ex} = 360 nm.

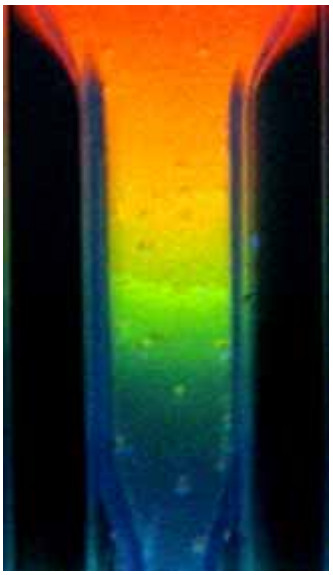

Figure 1.4 Multicolor photoluminescence pattern in the stationary Si nanoparticle suspension during the UV catalyzed acid dissolution. Sample cell was illuminated at 340 nm through the bottom cell window.

1.2.2 Surface fuctionalization and purification of conjugates

In order to functionalize a surface of SNs, I used 4-azido-2,3,5,6-tetrafluorobenzoic acid, succinimidyl ester (ATFB, SE) which is a bi-functional crosslinker with a photo reactive moiety and an amine reactive group. The overall process of biomolecule conjugation to silicon nanocrystals is shown in Figure 1.5. Following synthesis of H-terminated Si nano-particle, their surface is derivatized with carbo-hydro group and the ATFB hetero bi functional linker is introduced to attach the amine reactive group. Subsequently, Streptavidin was coupled to octane terminated silicon nanocrystals with a bi functional crosslinker. Photoreactive fluorinated functional group connects to the alkyl terminated SNs, while succinimidyl ester group reacts with amine groups of streptavidin.

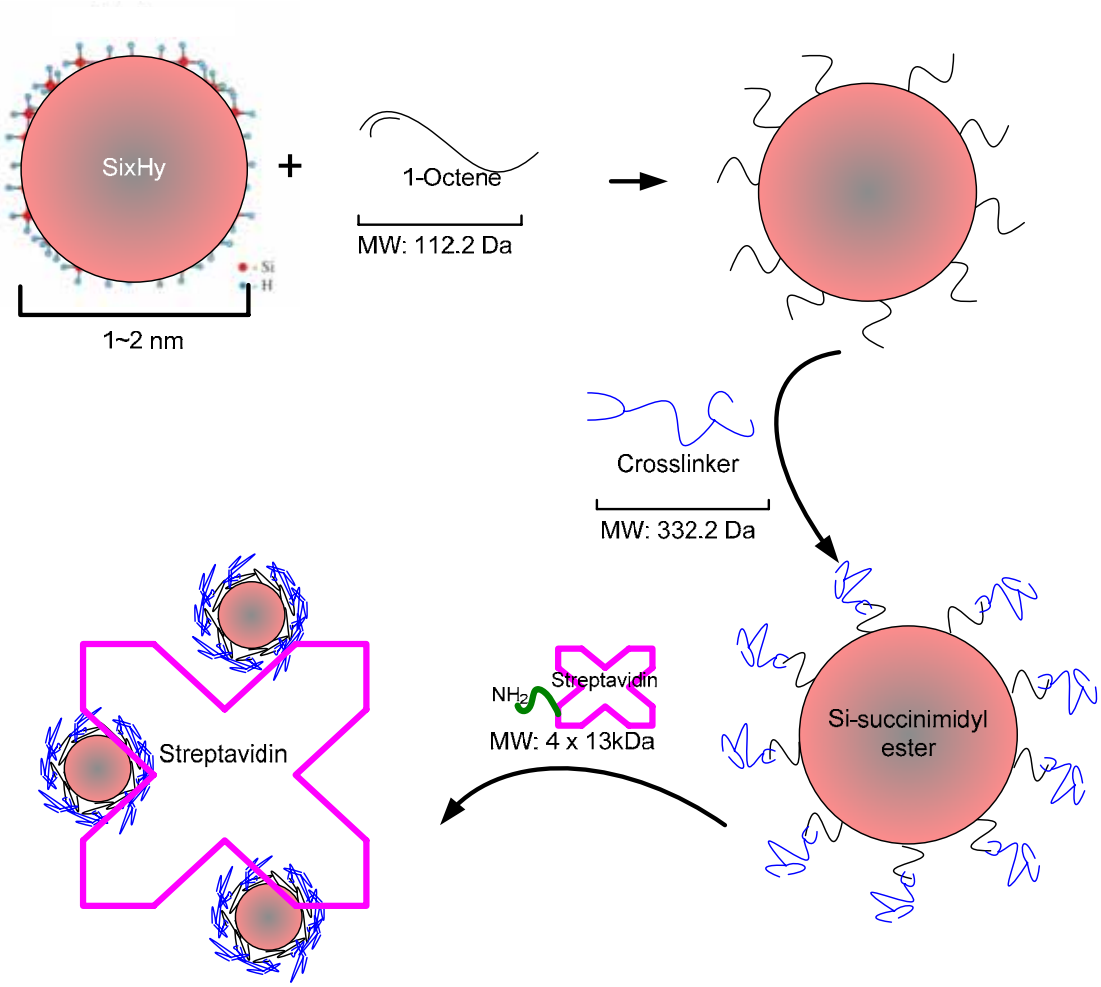

Figure 1.5 Overall SNs - bio molecule conjugation procedure

Surface functionalized SNs with 1-octene showed blue and bright fluorescence. Level of fluorescence intensity has dropped in the course of sequential conjugation procedures (Fig 1.6) but a degree of dropping was not significant (30% decrease of fluorescence intensity). Decreased intensity of fluorescence peak at 400 nm which corresponds to the presence of SNs and emerging of new broad peak at around 430 nm from the conjugated product indirectly confirms the successful binding of SNs on the targeted streptavidin.

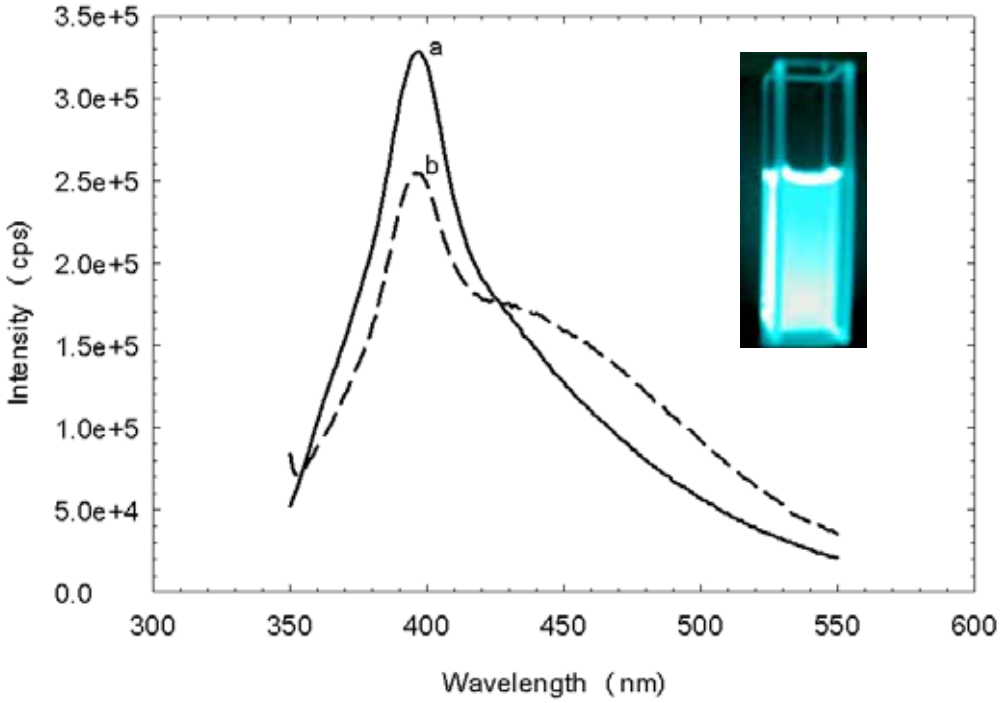

Figure 1.6 Fluorescence spectra of octane covered SNs (a) and streptavidin marked with SNs (b) with the excitation of 340 nm.

Figure 1.7 shows separated bands of SNs-streptavidin complexes and neat streptavidin from gel electrophoresis. When I compared with neat streptavidin, SNs-streptavidin conjugates have an earlier elution and elongated band. Since gel electrophoresis was performed in a native condition where elution of the band depends on the morphological shape and the native charges of the analytes, earlier elution of SNs-streptavidin conjugates is explained with additional surface charges of streptavidin resulted from the binding of SNs. The spreading of band which came from SNs-streptavidin conjugates suggests that conjugated products are not mono-dispersed in molecular weight and surface charges. Since SNs produced from lateral etching and followed sonication of Si wafer has broad size distributions, conjugated streptavidin also becomes to have broad size or molecular weight spread. At the same time, the elongated band is clear evidence that conjugations between SNs and streptavidin have been accomplished with different binding efficiencies. More bindings of SNs to one streptavidin would result in further elution of it because of negatively increased net surface charge of conjugate. However, clarification of eluted band based either on molecular weight or surface charge is not trivial because of following shortcomings that I will investigate further. First of all, the quantitative correlation of eluted band with conjugate's molecular weight and surface charge is not so simple because it is unclear how surface charges are changing along with the different sizes of nanoparticle. Furthermore, I haven't investigated yet how critical the effect of changing molecular weight and surface charges of SNs is on the efficiency of binding to streptavidin. Even though there are several points I should

investigate deeply in the future, a clear difference of conjugates' elution time from neat streptavidin promises high possibility in purification and separation of desired conjugated products from unreacted intermediates and proteins which would help to boost up the labeling efficiency of biotinylated biomaterials.

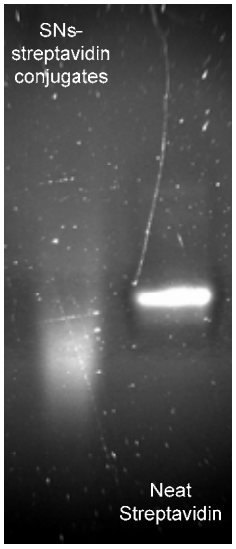

Figure 1.7 Native gel electrophoresis with streptavidin conjugated SNs and neat streptavidin. 200V, 2 hour elution, and a mobile buffer: Tris-HCl, pH 6.8.

1.3 Reference

[1] Medintz, I. L; Uyeda, H. T.; Goldman E. R.; Mattoussi H. "Quantum dot bioconjugates for imaging, labelling and sensing", *Nature Materials* **2005**, *4*, 435-446.

[2] Clarke, S. J.; Hollmann C. A.; Zhang, Z.; Suffern, D.; Bradforth, S. E.; Dimitrijevic, N. M.; Minarik, W. G.; Nadeau, J. L. "Photophysics of dopamine modified quantum dots and effects on biological systems", *Nature Materials* **2006**, *5*, 409-417.

[3] Sun, B.; Marx, E.; Greenham, N. C. "Photovoltaic Devices Using Blends of Branched CdSe Nanoparticles and Conjugated Polymers", *Nano Lett.* **2003**, *3*, 961-963.

[4] Watt, A.; Thomsen, E.; Meredith, P.; Rubinsztein-Dunlop, H. "A new approach to the synthesis of conjugated polymer–nanocrystal composites for heterojunction optoelectronics", *Chem. Commun.* **2004,** 2334-2335.

[5] Larson, D. R.; Zipfel, W. R.; Williams, R. M.; Clark, S. W.; Bruchez, M. P.; Wise, F. W.; Webb, W. W.; "Water-Soluble Quantum Dots for Multiphoton Fluorescence Imaging in Vivo", *Science* **2003**, *300*, 1434-1436.

[6] Imamoglu, A.; Awschalom, D. D.; Burkard, G.; DiVincenzo, D. P.; Loss, D.; Sherwin, M.; Small, A. "Quantum Information Processing Using Quantum Dot Spins and Cavity QED", *Phys. Rev. Lett.* **1999**, *83*, 4204-4207.

[7] Redl, F. X.; Cho, K. S.; Murray, C. B.; O'Brien, S. "Three-dimensional binary superlattices of magnetic nanocrystals and semiconductor quantum dots", *Nature* **2003**, *423*, 968-971.

[8] Haremza, J. M.; Hahn, M. A.; Krauss, T. D.; Chen, S.; Calcines, J. "Attachment of Single CdSe Nanocrystals to Individual Single-Walled Carbon Nanotubes", *Nano Lett.* **2002**, *2*, 1253-1258.

[9] Korberling, F.; Mews, A.; Basche, T. "Oxygen-Induced Blinking of Single CdSe Nanocrystals", *Advanced Materials* **2001**, *13*, 672-676.

[10] Yao, J.; Larson, D. R.; Vishwasrao, H. D.; Zipfel, W. R.; Webb W. W.; "Blinking and nonradiant dark fraction of water-soluble quantum dots in aqueous solution", *Proc. of Nat. Aca. of Sci. of USA* **2005**, *102*, 14284-14289.

[11] Choi, J.; Wang, N. S.; Reipa, V.; *Langmuir*, in revision.

[12] Cullis, A. G.; Canham, L. T.; Calcott, D. J.; "The structural and luminescence properties of porous silicon", *J. Appl. Phys.* **1997**, *82*, 909-965.

[13] Trindade, T.; O'Brien, P.; Pickett, N.L.; "Nanocrystalline Semiconductors: Synthesis, Properties, and Perspectives", *Chem. Mater.* **2001**, *13*, 3843-3858.

[14] Michalet, X.; Pinaud, F.F.; Bentolila, L.A.; Tsay, J.M.; Doose, S.; Li, J.J.; Sundaresan, G.; Wu, A.M.; Gambhir, S.S.; Weiss, S.; "Quantum Dots for Live Cells, in Vivo Imaging, and Diagnostics", *Science* **2005**, *307*, 538-544.

[15] Uhlir, A.; *Bell Syst. Tech. J.* "Electrolytic shaping of germanium and silicon", **1956**, *35*, 333-347.

[16] Reboredo, F.A.; Galli, G.; "Theory of Alkyl-Terminated Silicon Quantum Dots", *J. Phys. Chem. B.* **2005**, *109*, 1072-1078.

[17] Wang, L.; Reipa, V.; Blasic, J. "Silicon Nanoparticles as a Luminescent Label to DNA", *Bioconjugate Chem.* **2004**, *15*, 409-412.

[18] Ding, z.; Quinn, M. B.; Haram, A. K.; Pell, L. E.; Korgel, B. A.; Bard, A. L.

"Electrochemistry and Electrogenerated Chemiluminescence from Silicon Nanocrystal Quantum Dots", *Science* **2002**, *296*, 1293-1297.

[19] Buriak, J.M.; "Organometallic Chemistry on Silicon and Germanium Surfaces", *Chem. Rev.* **2002**, *102*, 1271-1308.

[20] Bley, R.A.; Kauzlarich, S.M.; "A Low-Temperature Solution Phase Route for the Synthesis of Silicon Nanoclusters", *J. Am. Chem. Soc.* **1996**, *118*, 12461-12462.

[21] Heath, J.R.; "A Liquid-Solution-Phase Synthesis of Crystalline Silicon", *Science* **1992**, *258*, 1131-1133.

[22] Aihara, S.; Ishii, R.; Fukuhara, M.; Kamata, N.; Terunuma, D.; Hirano, Y.; Saito, N.; Aramata, M.; Kashimura, S.; "Electroreductive synthesis and optical characterization of silicon nanoparticles", *J. Non-Cryst. Sol.* **2001**, *296*, 135-138.

[23] Hua, F.; Swihart, M. T.; Ruckenstein, E. "Efficient Surface Grafting of Luminescent Silicon Quantum Dots by Photoinitiated Hydrosilylation", *Langmuir* **2005**, *21*, 6054-6062.

[24] Yamani, Z.; Ashhab, S.; Nayfeh, A.; Thompson, W. H.; Nayfeh, M. "Red to green rainbow photoluminescence from unoxidized silicon nanocrystallites", *J. Appl. Phys.* **1998**, *83*, 3929-3931.

[25] Jung, K. H.; Shih, S.; Hsieh, T. Y.; Kwong, D. L.; Lin T. L. "Intense photoluminescence from laterally anodized porous Si", *Appl. Phys. Lett.* **1991**, *59*, 3264-3266.

[26] Belomoin, G.; Therrien, J.; Smith, A.; Rao, S.; Twesten, R.; Chaieb, S.; Nayfeh, M. H.; Wagner, L.; Mitas, L. "Observation of a magic discrete family of ultrabright Si nanoparticles", *Appl Phys Lett.* **2002**, *80*, 841-843.

[27] Wilson, W.L.; Szajowski, P.F.; Brus, L.E.; “Quantum Confinement in Size-Selected, Surface-Oxidized Silicon Nanocrystals”, *Science* **1993**, *262*, 1242-1244.

[28] Rogozhina, E.V.; Eckhoff, D.A.; Gratton, E.; Braun, P.V.; “Carboxyl functionalization of ultrasmall luminescent silicon nanoparticles through thermal hydrosilylation”, *J. Mater. Chem.* **2006**, *16*, 1421-1431

Chapter 2: Electrochemical Synthesis of Silicon Nanocrystals

2.1 Introduction

Since the discovery of the intense photoluminescence in the porous silicon, [1] silicon nanocrystals (SiNCs) are attracting a growing interest for a variety of potential applications [2]. Nanoparticle physicochemical properties can be tuned in the wide range by adjusting particle size in the quantum confinement range (d<5nm), suggesting fresh design in photonics, photovoltaics and catalysis [3]. Moreover, material biocompatibility entails applications for *in-vitro* biological tagging [for a review, see ref. 2a], and as a platform for drug delivery [2].

Significant quantities of the nanoparticle material would be required for practical applications, however, most current procedures typically provide microgram to milligram quantities of silicon nanoparticles. Published synthesis methods can be classified into the top-down (wafer etching [4], laser ablation [5]) and bottom-up (inverse micelle synthesis [6], high pressure silane supercritical [2g], plasma [7], silane pyrolysis [8] and solution based reduction synthesis [9]) broad categories. Every method has its own merits and limitations. Top-down wafer etching is low cost procedure and is potentially suitable for mass nanoparticle production. However, it typically gives a wide size distribution of nanoparticles and requires separate process for surface functionalization. Inverse micelle bottom-up synthesis has been demonstrated to yield a monodisperse particle sizes while encountering difficulties with obtaining a crystalline structure. Laser ablation has been extensively used to

make industrial quantities of various material nanoparticles [5a] albeit particles sizes typically exceed the upper limit for the quantum confinement effect (d>10 nm). Low temperature reductive chlorosilane condensation based synthesis potentially may lead to inexpensive Si nanocrystal mass production [9]. These processes use metallic Na, K, or their derivatives as reducing agents for tetrachlorosilane and typically generate several reaction byproducts. A typical procedure includes product purification and a separate Si nanoparticle surface passivation step [9b].

Electrochemical reduction by its very nature does not require chemical reduction agents thus minimizing reaction byproducts [10]. It is routinely used in organic synthesis reactions, including polysilane condensation from dichloromethylphenylsilane [11]. The electroreductive coupling of organodichlorosilanes with mercury electrode was reported in 1970's [12a] as a method to form disilane, but was not effective in the preparation of polysilane [12b]. Only recently polysilane formation by way of chlorosilane electroreduction has been achieved by Kogai et al. [11a] using catalytic amounts of anodically dissolved Mg^{2+}. The polymerization of dichloromethylphenylsilane was carried out by using carbon electrodes and pre-electrolysis technique to give linear polymers of up to 17000 molecular weight. Reductive condensation of trichlorosilanes forms 3-dimensional Si networks and can eventually result in crystalline Si particles [13]. Submicrometer-sized silicon single crystals were prepared when octyltrichlorosilane was reduced by metallic sodium at high pressure and temperature over several days. Recently, Aihara et al. [14] described synthesis of the 3 nm Si nanoparticles using electrochemical reduction of tetrachlorosilane. Amorphous Si particles demonstrated room

temperature photoluminescence and were covered by surface-oxide. Tetrachlorosilane can be reduced in non-aqueous electrolytes at potentials lower than -3.6 V (vs. Pt quasi-reference electrode) [15]. Here we demonstrate ultra-small Si nanocrystal formation by means of ultrasound assisted electrochemical octyltrichlorosilane reduction that produces octane terminated Si nanocrystals in a single step. Our choice of octyltrichlorosilane as a reaction precursor was motivated by its reported ability to limit the resulting Si nanoparticle size [13]. The described procedure allows to make SiNC's with alkyl surface termination, is clean, relatively simple, and potentially scalable to industrial quantities.

2.2 Materials and Methods

2.2.1 Electrochemical reduction cell

Figure 2.1 depicts the scheme of electrochemical reduction cell. Figure 2.2 shows Mg electrodes (7.7 mm dia., 25 mm length, 99.9%, Alfa Aesar, Ward Hill, MA) designed for a good contact and reactivity in the electrochemical cell. Two pairs of electrodes are served as cathodes and anodes, respectively. Electrodes were held by the polytetrafluoroethylene (PTFE) holder which was also serving as a cap for the reaction cell. PTFE cap has a hole in the middle to introduce a Ti sonication bar equipped with the ultra sound converter (model# CL4, Fischer Scientific, Pittsburgh, PA) connected to a high power sonic dismembrator (model# 550, Fischer Scientific, Pittsburgh, PA) into the reduction cell. Also there were several small holes to inlet reagents and outlet products as well as to provide nitrogen to a cell for purging the solution (Fig. 2.1).

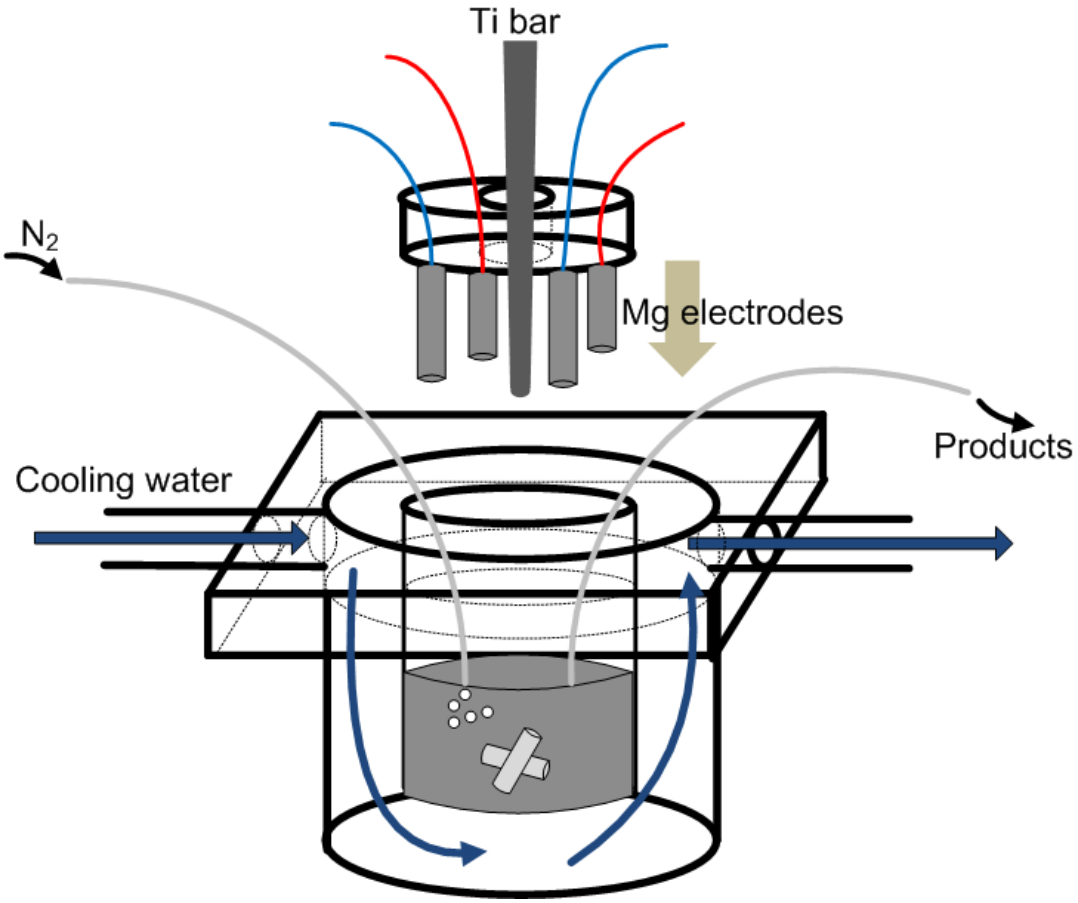

Figure 2.1 Scheme of the electrochemical reduction cell.

A magnetic stirrer was positioned on the bottom of the cell to ensure thorough mixing of the solution. Electrochemical cell was temperature controlled by the surrounding cooling tubes at 4°C. Electrochemical cell with Mg electrodes and sonication bar was located in the drying, nitrogen environment glove box (855-AC, Plas Labs, Lansing, MI). Each pair of electrodes was connected to the power source (model# 363 potentiostat, EG&G PARC, Oak Ridge, TN) and frequency function generator (model# 29, Wavetek, San Diego, CA) outside the glove box to generate pulse currents with the period of 30 sec. Before the solution was prepared, the glove box was flushed with the several cycle of filling nitrogen and vacuuming. Completely dried, temperature controlled, and full nitrogen environment was maintained for the rest of procedures.

2.2.2 Reagents preparation and product purification

100 ml of anhydrous tetrahydrofuran (THF; Sigma-Aldrich, St. Louis, MO) was introduced in the reaction cell (Fig. 2.1~2) and purged with N_2 for 30 min to completely remove any dissolved water molecules in the solvent. Next, 1 mg of lithium perchlorate (Sigma-Aldrich, St. Louis, MO) was added to the THF solution. Then, 10 ml of trichloro(octyl)silane (Sigma-Aldrich, St. Louis, MO) was introduced in the cell and mixed well. After complete mixing, the solution was kept stirred by the magnetic stirrer, purged with nitrogen and sonicated, the reducing reaction was progressed at the current density of 10 mA/cm^2 with the periodic alteration of charges for every 30 sec.

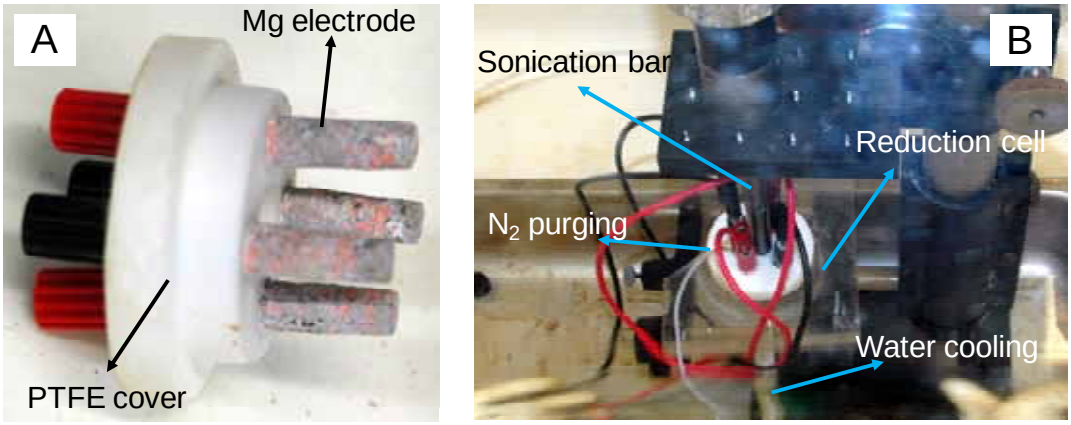

Figure 2.2 Electrochemical reducing cell. A: four electrodes serving for cathodes and anodes. B: Fully equipped setting of reduction cell.

Parameters for a 10MHz DDS function generator were 0.3 Hz frequency, 50 ohm, and 600 mV DC. During the reduction, the color of the solution turned into yellow and gradually changed to brown and black in accordance with the reaction time.

Figure 2.3 depicts polymerization of octyltrichlorosilane tetrachloride on the magnesium electrode with the supply of lithium perchloride electrolytes in anhydrous tetrahydrofuran (Fig. 2.3) The electrochemical reducing reaction was stopped at desired length of reducing time which was determined by the electrical energy that has been given to the cell (3F). Reduced product was taken from the cell and purified by way of the hexane/methanol extraction. Solvent extraction is adapted here to separate SiNCs based on their relative solubilities in immiscible liquids, hexane and methanol. Sample was poured into the hexane/methanol solution (1:1 volume ratio) and let sit for 2 hr. For further purification of the reduced product, several repetition of solvent extract can be applied. More hydrophobic Si particles were collected from the hexane layer and filtered through 0.2 μm PTFE syringe filter. Filtered product was transparent to visible light while it was blue fluorescent under 360 nm UV excitation.

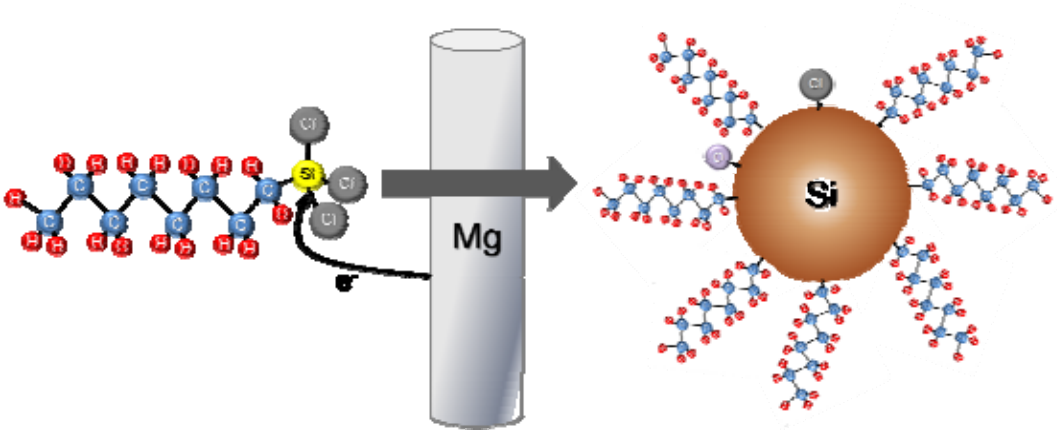

Figure 2.3 Electrochemical reduction synthesis of silicon nanocrystals

2.2.3 TEM, EDS, and XRD analysis

10 µl SiNCs suspension in hexane was dropped on a carbon film copper grid (Ted Pella Inc., Redding, CA) and dried completely by using nitrogen. Another drop of 10 µl SiNCs suspension was put on the same grid and dried again to increase the concentration on the grid. Two more drops of 10 µl SiNCs suspension were added and the solvent was evaporated. Size and shape of SiNCs was studied by using a transmission electrom microscopy.

High resolution transmission electron microscopy (HrTEM) was conducted with a JEOL 2100F field emission transmission electron microscope (JEOL Ltd., Tokyo, Japan). Acclerating voltage of TEM was set to 160 k. The electron gun was ZrO/W(100) field emission and had point to point length of 0.19 nm. Resolution of the HrTEM was 0.10 nm and spot size was set to 0.5 nm. Image was recored by using a CCD camera equipped with the microcope.

Element composition analysis of SiNCs-incubated cell samples were determined using energy dispersive x-ray spectroscopy (EDS, INCAx-sight, Oxford Ins., Oxfordshire, United Kingdom). Nanoparticles observed with TEM were simultaneously interacted with an electromagnetic radiation, analyzed by X-rays emitted by the SiNCs in response to being hit with the electromagnetic radiation. Since each element has a unique atomic structure allowing X-rays, the characteristic of an element's atomic structure could be indentified uniquely from each other. EDS was measured for real-time of 30 sec and the beam power was set to 200 kV.

Elevation angle was 18.7 degree. Each peak obtained was analyzed by using an established spectral data for each elements.

The XRD pattern of prepared powder sample was collected using a Bruker C2 Discover X-ray diffractometer with CuKα sealed X-ray tube, and Göbbel mirror, spanning from 8 to 93 degree. HiStar (GADDS) detector was used for real-time data collection, 2D diffractometry and quality patterns from dry SiNCs sample deposited on glass slide.

2.2.4 Photoluminescence, absorption and FTIR measurement

SiNCs were introduced in the quartz cuvette and photoluminescence (PL) was recorded by using a spectrofluorimeter (model LM800, SLM Inc., Urbana, IL) with the shifts of excitation filter settings from 260 to 350 nm. PL spectra of SNs at each excitation wavelength were normalized by their PL intensity and plotted together in order to compare the peak shiftings.

Absorption spectra of SiNCs were measured for SiNCs suspension in a 1 cm quartz cuvette with the reference cuvette containig pure hexane. UV/VIS spectometer (Lambda 850, Perkin Elmer, Waltham, MA) was used for absorption measurement and UV win lab (ver. 5.15, Perkin Elmer, Waltham, MA) was utilized for data collection and analysis. Absoprtion spectra was scanned from 200 to 600 nm for possible absorption peaks which are the signature of silicon crystals. UV and VIS lamps were D2 and Tungsten, respectively. Photomultiplier gain was set to 30 and the intergration time was 0.52 sec. Data interval was 2 nm and the attenuation of sample

and reference beam was set at 100%. Slit width was set to 2 nm and the lamp change over wavelength was set to 319.2 nm.

Aliquot of SNs suspension was deposited on KBr crystal IR cards (ICL, Garfield, NJ) and dried with N_2 for the Fourier transform infra red (FT-IR) spectra. To increase the concentration of deposited SiNCs, four more dropping and drying processes were follwed. Then, the sample depositted IR cards were introduced in the FT-IR spectrometer (IFS 66, Bruker optics Inc., Billerica, MA) in order to evalutate the surface chemical composition. Spectrometer was set to a resolution of 4 cm^{-1}, a KBr was used for IR beamsplitter and the scanner velocity was set to 10.0 kHz. An aperture was 6 mm and deuterated triglycine sulfate (DTGS) detector was used.

2.2.5 Quantum efficiency

Quantum efficiency of silicon nanoparticles was measured using a UV fluorescence standard tryptophan (QE=0.12). By comparing the photoluminescence and absorbance of silicon nanoparticles with a standard at the excitation wavelength, the quantum efficiency can be estimated using (Equation 2.1).

$$Q_{si} = Q_{st} \times \frac{F_{si}}{F_{st}} \times \frac{OD_{st}}{OD_{si}} \qquad \text{(Eq. 2.1)}$$

Where Q_{st} (12%) and Q_{si} are the quantum efficiency of tryptophan and silicon nanoparticles, F_{st} and F_{si} are the integrated emissions of tryptophan and silicon nanoparticles from 200 to 600 nm. OD_{st} and OD_{si} are the optical densities of tryptophan and silicon nanoparticles at the excitation wavelength.

Fig. 2.4 shows PL spectra obtained from silicon nanoparticles and tryptophan

standard. Each curve was then fitted with log normal distribution (Curve fitting by Sigmaplot ver. 9.0, Systat Software, Inc. San Jose, CA) and integrated from 200 to 600 nm in order to calculate the total number of photons emitted (Integrating calculations by Mathcad ver. 12.1, Mathsoft Engineering & Education, Inc. Needham, MA).

Equation 2.2 describes integration of a log normal distribution function used for fitting PL curves.

$$\int_{w_1}^{w_2} a \cdot \exp\left[-0.5 \left(\frac{\ln\left(\frac{x}{x_o} \right)}{b} \right)^2 \right] dx \qquad \text{(Eq. 2.2)}$$

Where w_1 and w_2 are the initial and final wavelengths (200 and 600 nm).

Integration results were entered into Eq. 2.1 to calculate the quantum efficiency of silicon nanoparticles ($Q = 13.1 \pm 0.5\%$).

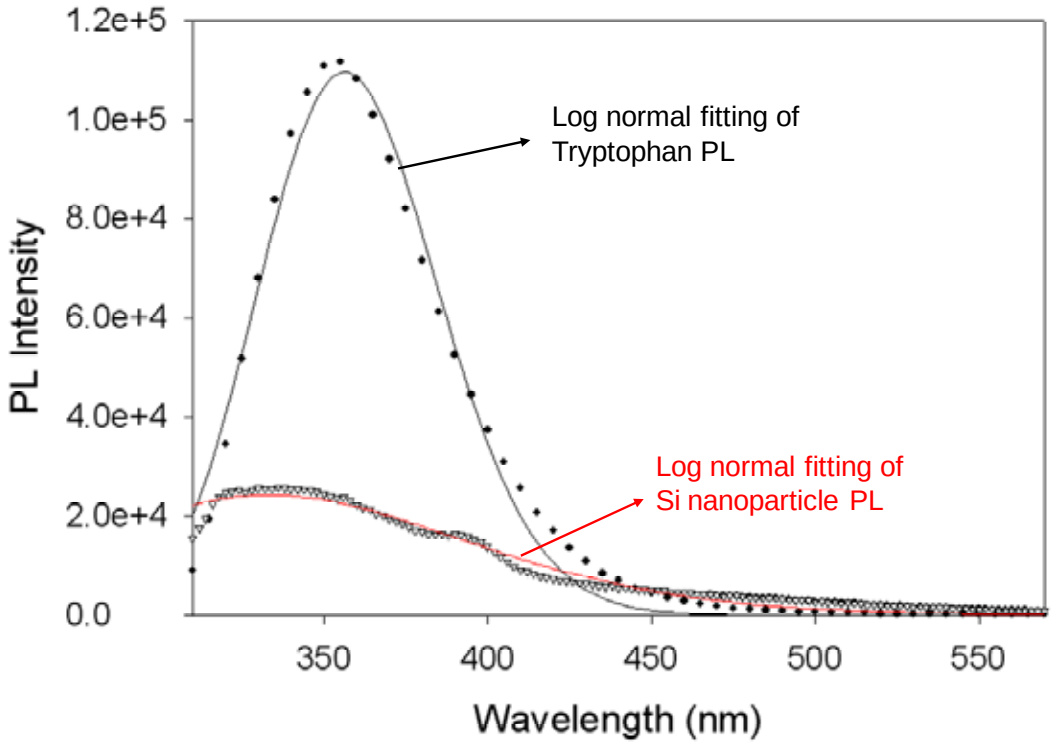

Figure 2.4 Photoluminescence spectra of tryptophan and silicon nanoparticles excited at 270 nm. Each spectra curve has been fitted with log normal distribution to integrate the area below the curves to calculate total amount of photons emitted.

2.2.6 Product yield calculation

Product yield was calculated by using Beer–Lambert law.

$$A = \log_{10} \frac{I_0}{I_1} = \frac{4\pi k}{\lambda} lc \qquad \text{(Eq. 2.3)}$$

where, A is the absorbance of the sample, I_0 is the incident light, I_1 is the intensity of the light after sample, k - sample extinction coefficient, λ - wavelength, l - path length and c - concentration. Using typical values: A= 0.015 cm^{-1}, λ = 300 nm, k = 10^{-4} $M^{-1}cm^{-1}$, l = 1 cm, particle concentration in the suspension was estimated, c = 0.358 mM. Assuming the average particle diameter as 3.2 nm, the formula weight w = 6.21E+04 (g/mol). Therefore, total particle weight in a 1 ml of product solution is 22.2 mg. Given the 200 fold dilution of the reaction mixture during extraction and purification, total product weight in the 110 ml solution is estimated at 2.44 g. Given that 10.7g (10 ml) of octyltrichlorosilane was used in the reaction, the estimated product yield: $Yield\ (\%) = \frac{Product\ amount(g)}{Initial\ amount(g)} = \frac{2.44g}{10.7g} \cong 22.8\%$

2.3 Results and Discussion

2.3.1 TEM and EDS results

Synthesized silicon nanoparticles were first characterized by using transmission electron microscopy (TEM), and X-ray energy dispersive spectroscopy (EDS) (Fig. 2.5). EDS contains distinct features at 1.74 keV attributable to Si, 0.53 keV to O, and 0.28 keV to C. C and Cu signal originated from the grid material (Fig. 2.5, C). The presence of oxygen reflects partial particle surface oxidation. Average size of Si nanoparticles was measured as 3.5 nm from TEM (Fig. 2.5, B).

Nanoparticle crystalline structure was validated by observation of lattice fringes in HrTEM images (Fig. 2.6, A), X-ray powder diffraction pattern (Fig. 2.6, C) and local area electron diffraction patterns of SiNCs (Fig. 2.6, B), all confirming cubic Si lattice.

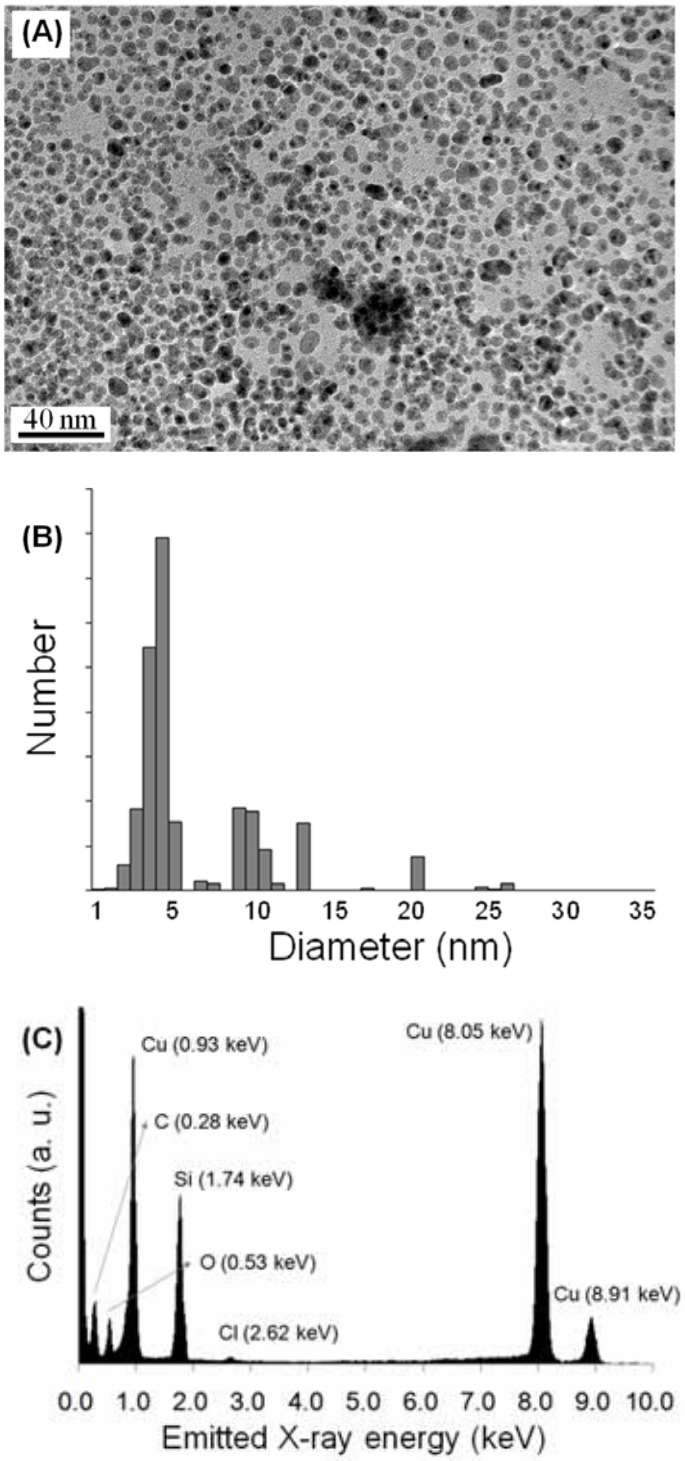

Figure 2.5 (A) - TEM image, showing spherical, well dispersed SiNCs. (B) - particle size distribution histogram, acquired from (A). (C) - X-ray energy dispersive spectra of SiNCs.

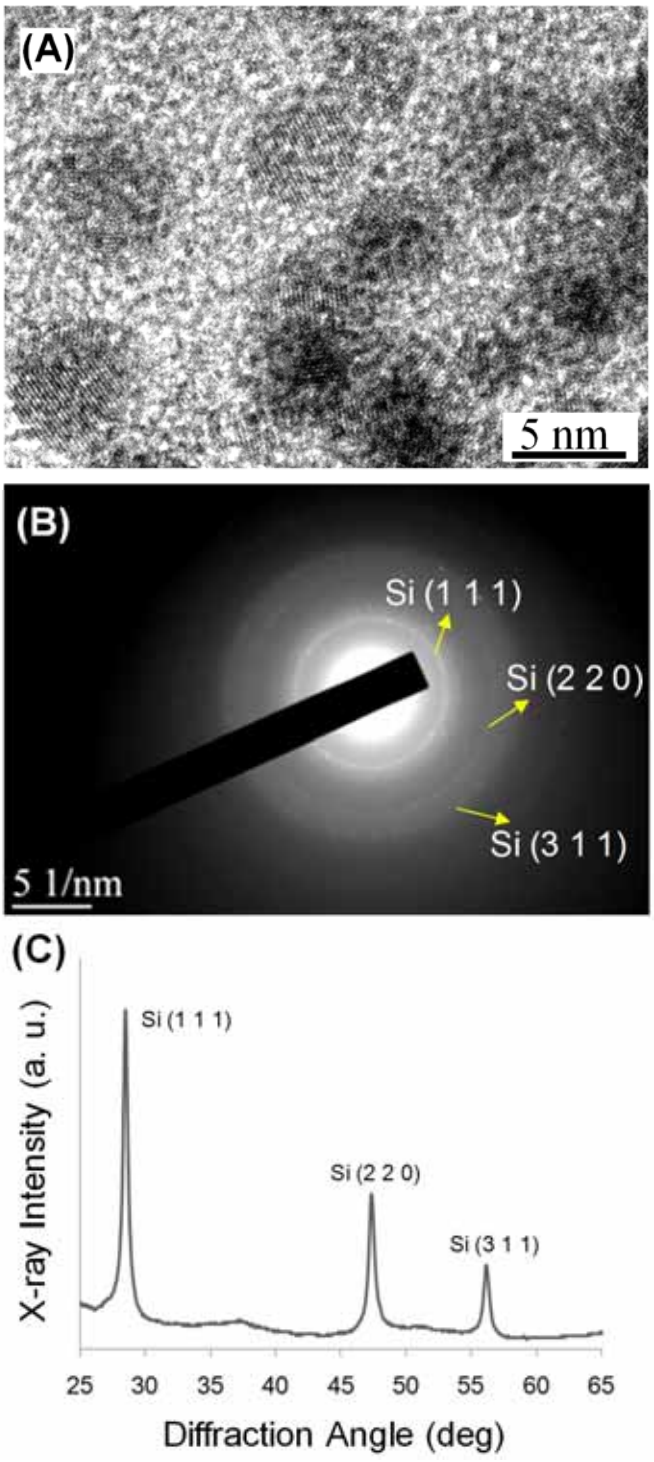

Figure 2.6 (A) - high resolution transmission electron microscopy (HrTEM) image of electrochemically reduced silicon nanocrystals. Scale bar is 5 nm. (B) - electron diffraction pattern, confirming the nanocrystalline structure. (C) - X-ray diffraction pattern of the dried SiNC powder.

2.3.2 Analysis of the lattice fringe spacing

Lattice spacing of synthesized silicon nanoparticles was calculated by three different methods: FFT analysis of the HrTEM image, electron diffration pattern, and X-ray powder diffraction. First, we employed the image analysis of high resoultion TEM (Fig. 2.7) to bring the diffractometry image which showed an characteristic points perpendicular to the lattice fringes. Fast Fourier Transform (FFT) of selected area in the HrTEM image (yellow square in Fig. 2.7) produced diffractogram depicted in Fig. 2.7. A distance between the two points in the diffractogram (Fig. 2.7), which is perpendicular to the fringes in the original image, is proportional to the reciprocal of the actual spacing between fringes. Based on the scale in the diffractogram, we obtained the lattice spacing of 3.14 ± 0.04 Å, which corresponds to the (1 1 1) spacing of the cubic silicon lattice.

Lattice spacing was also calculated using Si nanoparticle eletron diffraction patterns (Fig. 2.8). Since each rings in the diffraction pattern corresponds to the different crystal structure, at least three different crystallografic orientations are visible in the sample, shown in Fig. 2.8. The closest to the center and the brightest ring corresponds to silicon (1 1 1) crystal structure. Ring diameter measurement was used to calculate the characteristic distance between lattice fringes at 3.10 ± 0.02 Å. Next ring in the pattern corresponds to the silicon (2 2 0) crystal structure. The third ring, somewhat diffused ring, was assigned to the silicon (3 1 1) crystal structure based on the diameter value. Other, less intense, diffuse rings are from the carbon film or amorphous structures.

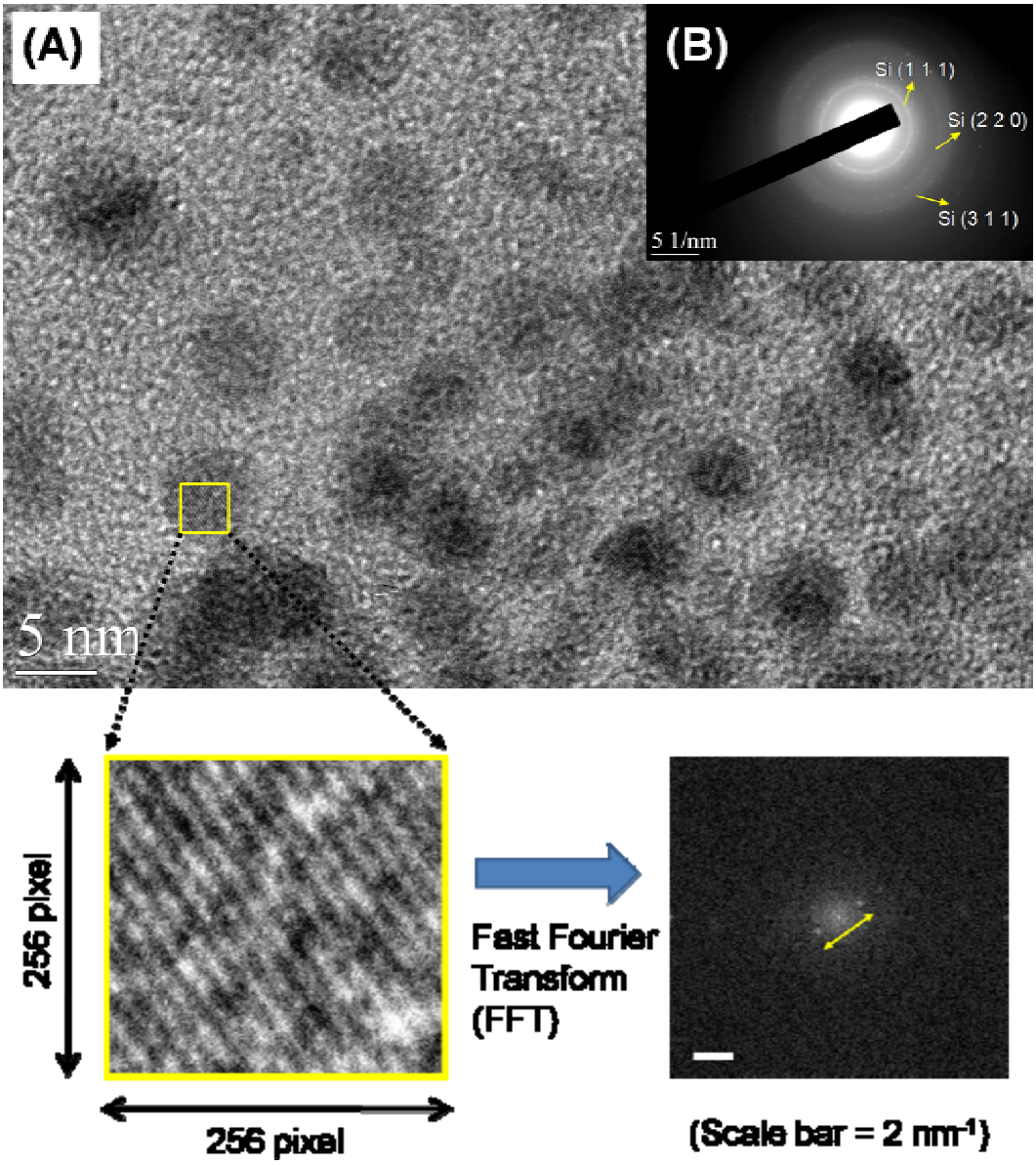

Figure 2.7 Fast Fourier Transform (FFT) analysis of HrTEM images (A). Yellow box (256 x 256 pixels) was used for the lattice fringe spacing calculation. A distance between the two points of the FFT image (yellow arrow) in the diffractogram was then used to calculate the distance between fringes (3.14 ± 0.04 Å).

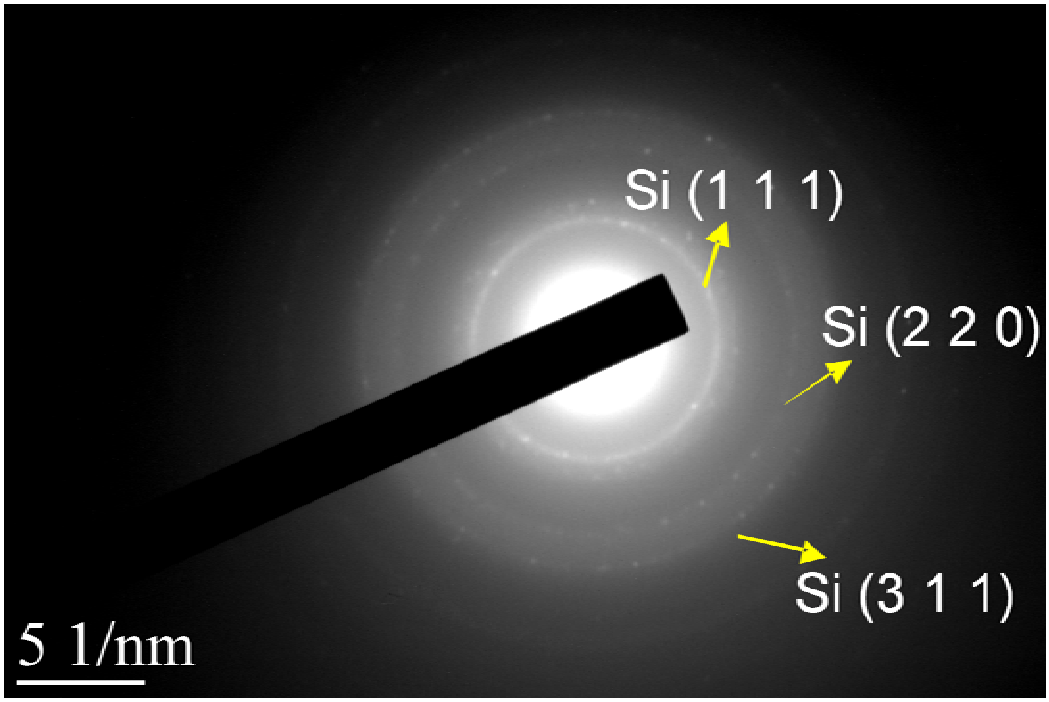

Figure 2.8 Electron diffraction patterns of SiNCs. Inner most ring corresponds to 3.10 ± 0.02 Å lattice spacing, which fits well Si (1 1 1) structure. Second ring (lattice spacing = 1.89 ± 0.03 Å) is very close to the silicon (2 2 0) lattice structure. Third ring (Lattice spacing = 1.66 ± 0.03 Å) was assigned to Si (3 1 1).

2.3.3 PL, Abs and FTIR results

Photoluminescence (PL) emission of Si nanoparticles shifted with excitation wavelength, also suggesting the quantum confinement (Fig 2.9, A). Maximum PL intensity the electrochemically synthesized SiNC suspension in hexane was measured at the excitation wavelength of 300 nm. Quantum yield (Q=10%) was measured relative to the Tryptophan standard, Q_{st}= 0.21 at λ_{ex}= 295 nm. PL intensity did not degrade under extended UV exposure, a typical feature of polysilanes [16].

UV-VIS absorbance (Fig. 2.9. A) edge is at approximately 350 nm, corresponding to the bandgap Eg~ 3.5 eV, a value consistent with the quantum confinement in the single nanometer range Si nanocrystals [6a].

Fourier transform infrared spectra (FTIR, Fig. 2.9. B), recorded on dry Si particles dispersed as a neat film on KBr crystal display characteristic features of the surface alkyl termination (CH_3 2955, 2872, 1378 cm^{-1}; CH_2 2924, 2854, 1466 cm^{-1}, and C-C 888 cm^{-1}), and asymmetric stretches from the surface oxide entities (O-Si-O, 1115 cm^{-1}). It is notable that Si-Cl (567 cm^{-1}) stretching mode was relatively weak, indicating full chlorosilane reduction. Nanocrystal surface octane termination could be expected, given the stabilization of Si-C bond in the reaction precursor [17] (Figure 2.9, B).

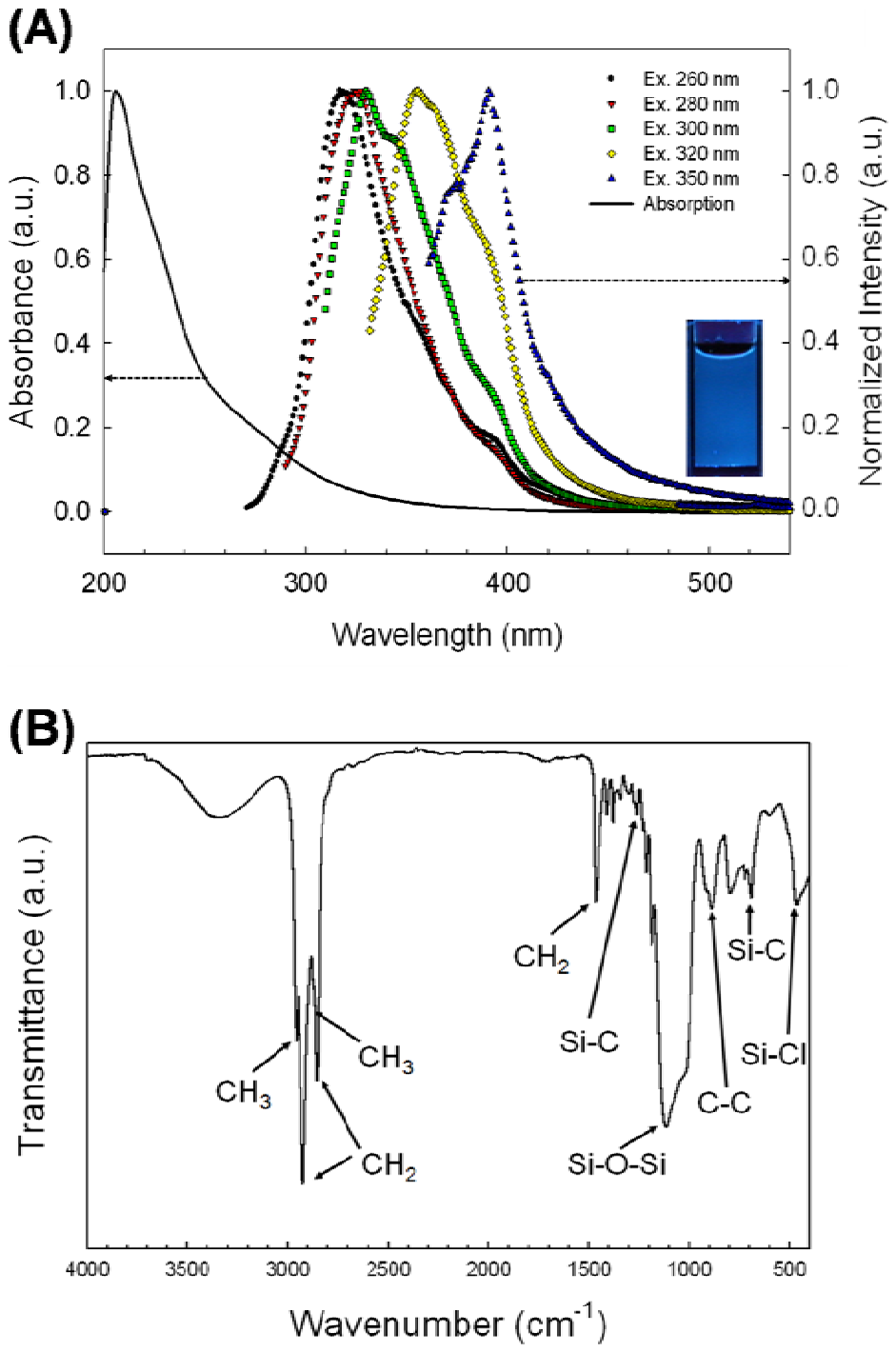

Figure 2.9 Optical property and surface chemistry of electrochemically reduced silicon nanoparticles: (A) - Normalized photoluminescence spectra of SiNCs. Inset shows a fluorescence image of silicon nanocrystal suspension under 365 nm illumination. (B) – infrared spectrum of dry SiNCs.

2.4 Summary

In summary, single nanometer range photoluminescent silicon nanocrystals were prepared at room temperature and ambient pressure using a direct electrochemical reduction of octyltrichlorosilane from the non-aqueous electrolyte. Resulting octane termination provides a stable passivation and could serve as a platform for further particle functionalization. A simple and scalable procedure potentially could address the requirement for stable ultrasmall Si nanocrystals in optoelectronic, photovoltanics and bioassay industries.

2.5 Reference

[1] Canham, L. T. *Appl. Phys. Lett.* **1990**, *57*, 1046-4048.

[2] (a) O'Farrell, N.; Houlton, A.; Horrocks, B. R. *Int. J. Nanomedicine*. **2006**, *1*, 451-472. (b) Brus, L. *Adv. Mater.* **1993**, *5*, 286-288. (c) Lockwood, D. J. *Light emission in silicon from physics to devices*; Academic Press: San Diego, CA, **1998**; p. 253-284. (d) Wang, L.; Reipa, V.; Blasic, J. *Bioconjugate Chem*. **2004**, *15*, 409-412. (e) Warner, J. H.; Hoshino, A.; Yamamoto, K.; Tilley R. D. *Angew. Chem., Int. Ed.* **2005**, *44*, 4550-4554. (f) Choi, J.; Wang, N. S.; Reipa, V. *Bioconjugate Chem.* **2008**, *19*, 680-685. (g) Ding, Z.; Quinn, B. M.; Haram, S. K.; Pell, L. E.; Korgel, B. A.; Bard, A. J. *Science* **2002**, *296*, 1293-1297.

[3] (a) Stupca, M.; Alsalhi, M.; Al Saud, T.; Almuhanna, A.; Nayfeh, M. H. *Applied Physics Letters* **2007**, *91*, 0631071-0631073. (b) Vrček, V.; Slaoui, A.; Muller, J.C. *Thin Solid Films* **2004**, *384*, 451-452.

[4] (a) Choi, J.; Tung, S.; Wang, N. S.; Reipa, V. *Nanotechnology* **2008**, *19*, 0857151-0857158. (b) Choi, J.; Wang, N. S.; Reipa, V. *Langmuir* **2007**, *23*, 3388-3394. (c) Belomoin, G.; Therrien, J.; Smith, A.; Rao, S.; Twesten, R.; Chaieb, S.; Nayfeh, M. H.; Wagner, L.; Mitas, L. *Appl Phys Lett.* **2002**, *80*, 841-843.

[5] (a) Carlisle, J. A.; Dongol, M.; Germanenko, I. N.; Pithawalla, Y. B.; El-Shall, M. S. *Chem. Phys. Lett.* **2000**, *326*, 335-340. (b) Carlisle, J. A.; Germanenko, I. N.; Pithawalla, Y. B.; El-Shall, M. S. *J. Electron Spectrosc. Relat. Phenom.* **2001**, *114-116*, 229-234.

[6] (a) Wilcoxon, J. P.; Samara, G. A.; Provencio, P. N. *Phys. Rev. B.* **1999**, 60, 2704-2714. (b) Warner, J. H.; Hoshino, A.; Shiohara, A.; Yamamoto, K.; Tilley, R. D. *Proc. SPIE* **2006**, *6096*, 6096071-6096078.

[7] Mangolini, L.; Thimsen, E.; Kortshagen, U. *Nano Lett.* **2005**, *5*, 655-659.

[8] Hua, F.; Swihart, M. T.; Ruckenstein, E. *Langmuir* **2005**, *21*, 6054-6062.

[9] (a) Baldwin, R. K.; Pettigrew, K. A.; Garno, J. C.; Power, P. P.; Liu, G.; Kauzlarich, S. M. *J. Am. Chem. Soc.* **2002**, *124*, 1150-1151. (b) Zou, J.; Baldwin, R. K.; Pettigrew, K. A.; Kauzlarich, S.M. *Nano Lett.* **2004**, *4*, 1181-1186.

[10] Sperry, J. B.; Wright, D. L. *Chem. Soc. Rev.* **2006**, *35*, 605-621.

[11] (a) Kogai, Y.; Ishifune, M.; Uchida, K.; Kashimura, S. *Electrochemistry* **2005**, 73, 419-423. (b) Shono, T.; Kashimura, S.; Ishifune, M.; Nishida, R. *J. Chem.*

Soc. Chem. Commu. **1990**, 1160-1161. (c) Ishifune, M.; Kashimura, S.; Kogai, Y.; Fukuhara, Y.; Kato, T.; Bu, H.; Yamashita, N.; Murai, Y.; Murase, H.; Nishida, R. *J. Organomet. Chem.* **2000**, *611*, 26-31.

[12] (a) Hengge, E.; Litscher, G. *Angew. Chem.* **1976**, *88*, 414-414. (b) Hengge, E.; Firgoi, H. *J. Organomet. Chem.* **1981**, *212*, 155-161.

[13] Heath, J. R. *Science* 1992, **258**, 1131-1133.

[14] Aihara, S.; Ishii, R.; Fukuhara, M.; Kamata, N.; Terunuma, D.; Hirano, Y.; Saito, N.; Aramata, M.; Kashimura, S. *J. Non-cryst. Solids* **2001**, *291*, 135-138.

[15] Nishimura, Y.; Fukunaka Y. *Electrochim. Acta.* **2007**, *53*, 111-116.

[16] (a) Miller, R. D.; Michl, J. *Chem. Rev.* **1989**, *89*, 1359-1410. (b) Bianconi, P. A.; Weidman, T. W. *J. Am. Chem. Soc.* **1988**, *110*, 2342-2344.

[17] Pawlenko, S. *Organosilicon Chemistry*; de Gruyter: New York, NY, **1986**; p 8.

Chapter 3: Bioconjugation of Silicon Nanocrystals

3.1 Introduction

Semiconductor quantum dots were recently recognized to have distinct advantages over organic fluorescent materials in biological tagging applications. Organic dyes are prone to photo bleaching under intense laser excitation, are vulnerable to the environmental factors such as temperature, oxidation, acidity, and interaction with certain ions that hamper their application in biological assays. In this regard stable, and efficient binary semiconductor quantum dots offer an attractive platform free of the above problems. Typically, they have size dependent narrow emission bands and a wide excitation range that permits a multicolor bioanalysis under the single wavelength excitation.

Various approaches of conjugating semiconductor quantum dots to biomolecules have been reported [1~14, for review, see ref. 1~5]. Water solubility, high fluorescence yield, and compatibility with the analytical protocol media are principal requirements for the practical fluorophore–biomolecule complexes. Binary quantum dot surface modifications for biological applications can be categorized to hydroxyls [6], peptides/proteins [7~9], thiols [10~11], block copolymers [12~13], and dendrimers [14]. However, regardless of surface derivatization, the bio application of binary quantum dots is hampered by their inherent chemical toxicity [15~19, for review, see ref. 15]. Consequently, the core materials (Cd/Se, Cd/S, In/P, etc.) require thick, complicated surface coating procedures to prevent toxic material contact with

the biosystem. Typically, this leads to a significant increase in the final particle size, and can markedly reduce their application area. Furthermore, such surface modifications often affect the fluorescence quantum yield and spectral properties, both of which hamper the reproducibility of the analysis. In this context, the need for the simple and efficient bioconjugation strategies using nontoxic photoluminescent nanoparticles is evident.

Photoluminescent silicon nanoparticles (SNs) are very appealing in the development of smaller biocompatible probes [20~23] as they are expected to be less hazardous than binary semiconductor based quantum dots. Moreover, silicon surface is open to various chemical functionalizations, thus offering numerous stabilization and bioconjugation options [24]. Sato et al. [25] reacted hydrogen terminated silicon nanocrystals with acrylic acid to form surface carboxyl functionalities, while Warner et al. used amine termination to ensure SN water solubility [22]. Such approaches allow engineering the desired functionality into silicon nanoparticles, increasing nanoparticle monodispersity, and preventing their aggregation that may complicate a bioanalysis. Here we explore a cross linker-bridged covalent attachment of octane modified SNs to streptavidin molecules that could be implemented in hybridization based assays as these often rely on streptavidin-biotin interactions.

Previously we have reported a conjugation process that describes anchoring of photoluminescent Si nanoparticles to a single stranded DNA in aqueous solutions [20]. In this study, we describe the procedure to covalently link SN's to streptavidin molecules that offers access to the protein bio-labeling, and may find application *in vitro* assays that rely on antibodies, cell receptors, and cell tracing probes. Covalent

bonding between the bifunctional crosslinker and a nanoparticle ensures complex stability throughout preparative sample treatments.

We employ 4-azido-2,3,5,6-tetrafluorobenzoic acid, succinimidyl ester (ATFB, SE), which is a bi-functional cross linker with a photo reactive diazirine and an amine reactive functionality. The four step process scheme is shown in Figure 3.1. Following nanoparticle preparation, hydrogen termination of SNs is substituted with a hydrocarbon moiety using a hydrosilylation reaction. Next, the ATFB bi-functional linker is attached under UV activation, and provides a bond to protein amine groups. Subsequently, the SNs-succinimidyl ester conjugate is exposed to streptavidin and form SN-Streptavidin complex via amide linkage. Since the cross linker has the UV reactive end, it allows to selectively couple the diazirine group to the methyl groups of the SN-bound hydrocarbon. SN photoluminescence measurements after each step of the procedure verify both the conjugation and photoluminescence efficiency. Finally, we test the tagged streptavidin functionality by reacting the nanoparticle-protein complex with the biotinylated polystyrene micro beads. Reported straightforward and efficient conjugation strategy, and assessment of tagged protein functionality demonstrate silicon nanoparticle potential as an efficient, stable, and bio compatible nano- probe.

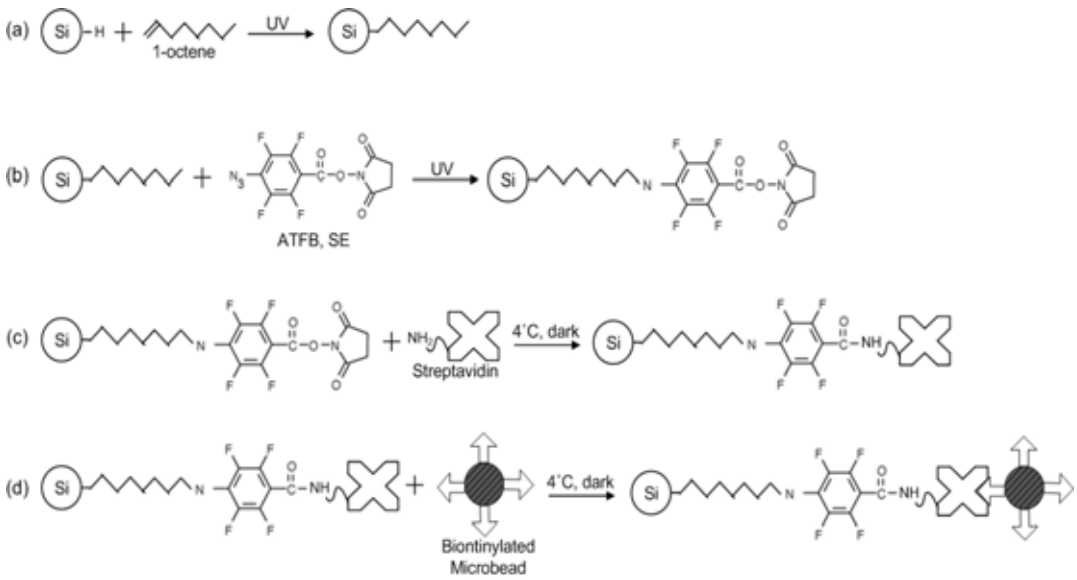

Figure 3.1 Schematic representation of the silicon nanocrystal and protein molecule covalent conjugation. (a) - octane attachment to SNs, (b) – bi-functional cross-linker (ATFB, SE) reaction with the octane methyl groups, (c) – amide bond formation between the streptavidin and activated crosslinker, (d) – test of the SN-streptavidin complex functionality by exposing it to the biotinylated polystyrene microbeads.

3.2 Materials and Methods

3.2.1 Nanoparticle preparation

Silicon nanoparticles were prepared using wafer anodic etch in HF based electrolyte. Both sides of the silicon wafer (As doped, <111> oriented, 0.001 ohm-cm to 0.01 ohm-cm conductivity, Virginia Semiconductor, Inc., Fredericksburg, VA) were electrochemically etched in the HF: H_2O: Ethanol (2:1:1, volume ratio) mixture. A lateral etching [20~21, 26~28] was performed in the Teflon cell that accommodates a 100 mm diameter round Si wafer placed between two Si cathodes. Electric contact was provided to the top edge of the vertically mounted wafer and electrolyte was slowly pumped into the cell, hence providing a solution/air boundary, rising along the wafer surface. Total etch time typically was about 4 h per 100 mm diameter wafer at 120 mA constant current, supplied by a galvanostat (Model 363, EG&G Inc., Princeton, NJ). Following anodic etching, the wafer was rinsed several times in deionized water, methanol (HPLC grade, Mallinckrodt Chemicals, Phillipsburg, NJ) and blow-dried with nitrogen gas. Dry wafers displayed an intense orange-red luminescence when excited with a 360 nm light. Next, the wafers were sonicated (Neytech, Bloomfield, CT) in a deaerated 10:1 (v:v) mixture of toluene : 1-octene for two hours under vigorous N_2 purging. The resulting particle suspension exhibited broadband red-orange photoluminescence under 365 nm excitation.

3.2.2 Surface functionalization

Following sonication, 20 ml of the Si nanoparticle suspension in toluene: 1-octene was placed in the quartz cuvette (Rayonet, Branford ,CT) under the N_2 blanket and exposed to 250 nm UV light for 30 min. inside the photo-chemical reactor (RMR-600) (Rayonet, Branford ,CT). The PL color turned to intense blue as a result of the photo-assisted hydrosilylation. Finally, the 1-octane derivatized silicon nanoparticle suspension was filtered by passing through the silica gel column.

In the next step of the conjugation protocol the bifunctional cross linker 4-azido-2,3,5,6-tetrafluorobenzoic acid, succinimidyl ester (ATFB, SE) (Invitrogen, Carlsbad, CA) is attached to the surface of SNs. A 100 μl batch of octane covered SNs suspension was mixed with 10 μl 4-azido-2,3,5,6-tetrafluorobenzoic acid succinimidyl ester (ATFB, SE) solution (c = 15 mM) in anhydrous carbon tetrachloride. The reaction mixture was exposed to UV light (λ= 365 nm) inside the UV reactor for 5 min. followed by complete solvent evaporation under N_2 flow. Consequently, fluorinated aryl azide of ATFB reacts with methyl groups of silicon – bound octane and forms C-N bond (Figure 3.1, b).

Covalent link to the protein molecules was completed by producing the amide bond between the bi-linker succinimidyl ester functionality and available streptavidin amine groups (protein molecule has about 100 exposed amines [29]).

3.2.3 SiNCs - Streptavidin conjugation

Dry, succinimidyl ester terminated SiNCs were redissolved in a 100 µl of anhydrous dimethyl sulfoxide (DMSO) and slowly added to a 100 µl of 0.1 M sodium bicarbonate buffer, containing 10 µg of purified streptavidin (Pierce, Rockford, IL). The reaction was carried out in the dark for 1 h under magnetic stirring. Reaction products were analyzed using the native gel electrophoresis. A 15 % Tris-HCl polyacrylamide gel (Bio-Rad, Hercules, CA) was injected with 1µL samples containing the reaction product, and the native streptavidin as control in the separate wells. After 2 h of native gel electrophoresis at 150 V in Tris buffer, the gel was dyed using the MicrowaveBlue protocol (Protiga, Frederick, MD) for protein staining, and imaged in the MultiImage light cabinet (Alpha Innotech, San Leandro, CA), using both visible light and UV excited fluorescence modes.

3.2.4 Functionality test of nanoparticle-protein conjugates

Functionality of the silicon nanoparticle - streptavidin complex was tested by mixing SN-streptavidin conjugates with a suspension of biotin coated polystyrene micro beads (average diameter d = 2 µm) (Polysciences, Warrington, PA). Prior to mixing, fresh micro beads were separated from their native supernatant by spinning at 10,000xG for 5 minutes. Next, micro beads were washed 3 times by resuspending them in phosphate buffer saline / bovine serum albumin blocking buffer (0.1 M, pH 7.4), followed by centrifugation. A batch of diluted micro bead solution was incubated with the SN-streptavidin conjugate for 30 min at 4°C, and the supernatant

was separated from the mixture by centrifugation. Finally, biotinylated beads were washed in PBS/BSA binding buffer at least three times.

3.2.5 Characterization of Streptavidin-SiNCs conjugates

FTIR spectra of reaction products and intermediates were recorded using samples deposited on PTFE IR cards (ICL, Garfield, NJ) on a Bruker IFS 66 (Bruker optics Inc., Billerica, MA) spectrometer.

Fluorescence spectroscopy was used to assess silicon nanoparticle photoluminescent properties after each step of the conjugation procedure. Emission spectra were acquired using 360 nm excitation on a SLM LM800 spectrofluorimeter (SLM Inc., Rochester, NY). Samples were contained in the 3 mm optical path-length quartz cells. Polystyrene micro beads were imaged with fluorescence microscope (Olympus BX50, Tokyo, Japan), using samples spread on glass microscope slides. Images were recorded with SPOT-RT KE digital cameras (Diagnostic Instruments, Sterling Heights, MI) and processed using imaging software (SPOT, version 4.0, Diagnostic Instruments, Sterling Heights, MI).

3.3 Results and Discussion

3.3.1 Optical properties of SiNCs

Fresh silicon nanoparticles, suspended in toluene:octene mixture, displayed red-orange photoluminescence with maximum emission at 600 nm (Fig. 3.2). However, the emission experienced blue shift with maximum at 400 nm following UV assisted derivatization with 1-octene. Similar effect was earlier reported by Ruckenstein, who suggested a change in emission mechanism upon hydrosilylation [30]. The blue emission intensity slightly decreased after anchoring to the protein molecule (Fig. 3.2). Decreased intensity at 400 nm, which is typical to octane derivatized SNs, and the appearance of a new broad feature around 450 nm in the emission spectrum of the final product suggests perturbations in nanocrystal electronic structure due to the covalent bond to the target protein.

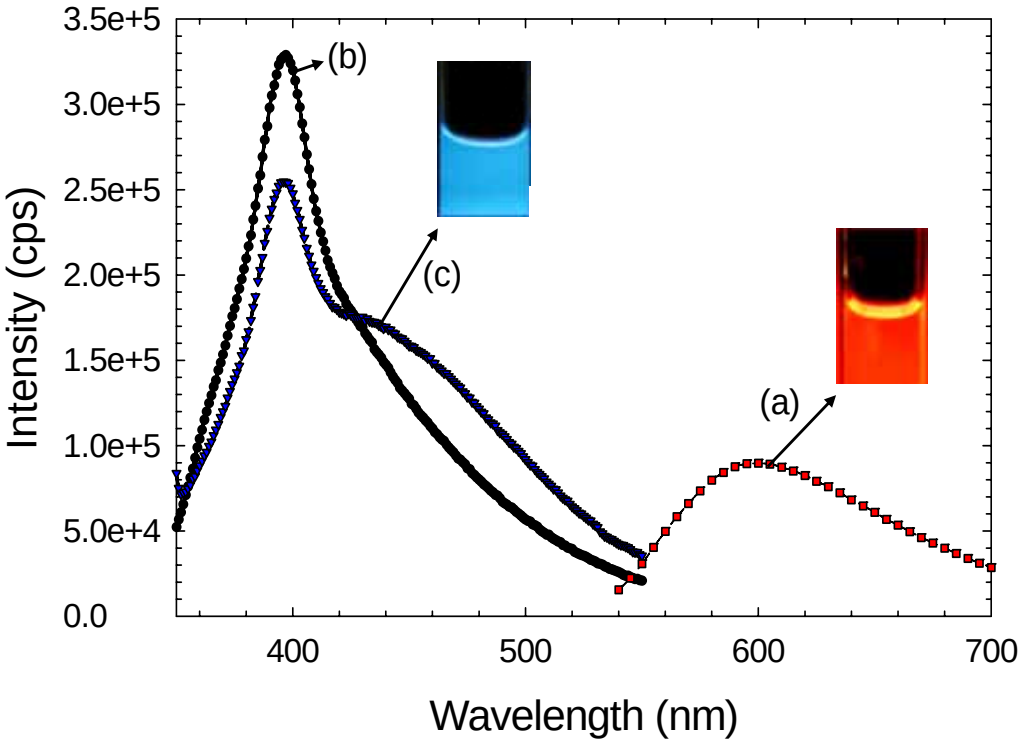

Figure 3.2 Photoluminescence spectra of freshly prepared silicon nanoparticles in toluene – (a), following octane surface derivatization - (b), and streptavidin conjugation - (c); λ_{exc} = 340 nm. Insets show the fluorescence images of fresh and derivatized particle under UV excitation.

3.3.2 Surface chemistry analysis of surface modified nanoparticle

Figure 3.3 shows the FTIR spectra of silicon nanoparticles recorded during various stages of the protein conjugation procedure. Spectrum recorded following the UV assisted hydrosilylation (Fig. 3.3, A) contains features, assigned to Si-C stretch (1274 cm^{-1}), C-H stretch (2965, 2928, 2964 cm^{-1}) and methylene bending (1463 cm^{-1}) modes, and is consistent with the silicon nanoparticle surface bound alkane. Vibrational spectrum gets more complicated subsequent to the reaction with the 4-azido-2,3,5,6-tetrafluorobenzoic acid succinimidyl ester (ATFB, SE) ,Fig. 3.3, C, suggesting the anchoring of the bilinker molecule to the octane derivatized silicon particles. Notably, the disappearance of the aryl azide stretch at 2130 cm^{-1}, a prominent peak in the pure compound spectrum (Fig. 3.3, B) indicates that this group has been converted to nitrene in a photocatalyzed reaction. In addition, several peaks represent the fluorobenzoic acid moiety (1104, 1648, and 1155 cm^{-1}) and octane (1275, 2395 cm^{-1}) that was conjugated in the prior step.

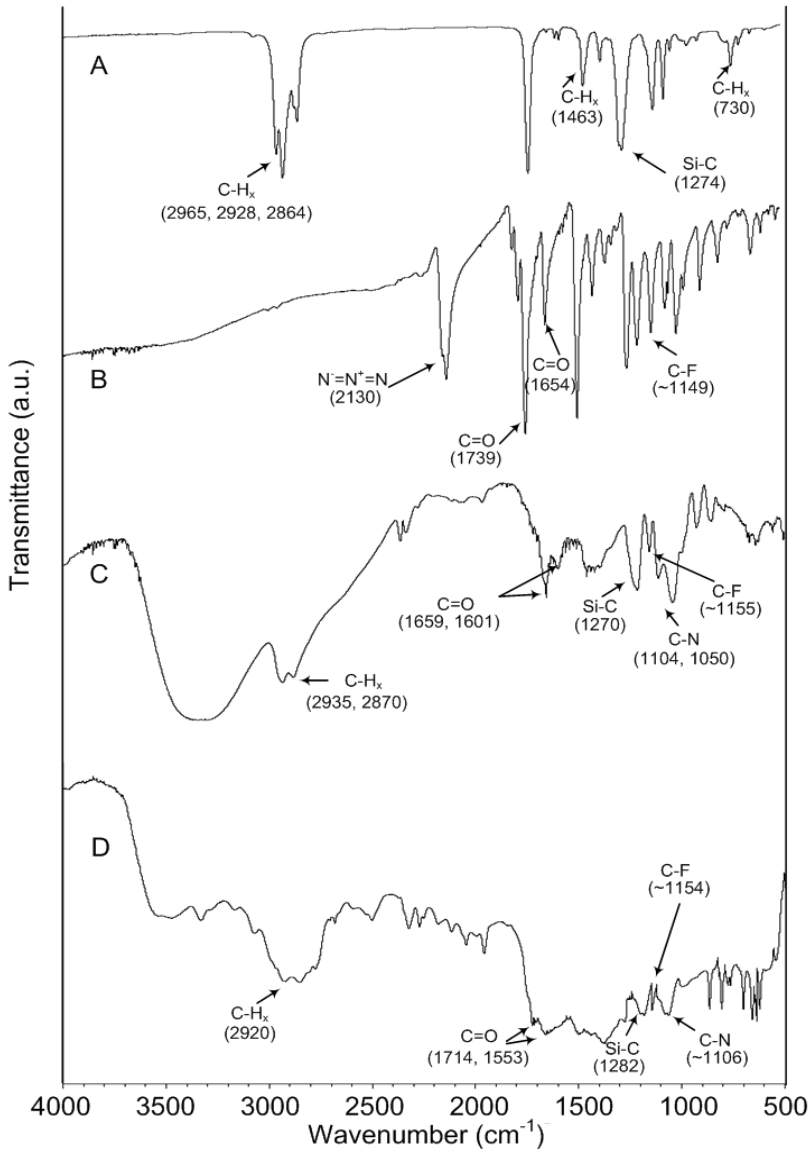

Figure 3.3 FTIR transmission spectra for dried films of: A – silicon nanoparticles, following the reaction with 1-octene (step a in Fig. 2.1); B – spectrum of pure bi-linker ATFB, SE; C – silicon nanoparticles subsequent to UV assisted reaction with bi-linker (step b in Fig. 2.1), and D –product of the conjugation reaction (step c in Fig. 2.1).

3.3.3 Purification of Streptavidin-SiNCs conjugates

The native electrophoresis gel image in Figure 3.4 contains separate bands corresponding to the SNs-streptavidin complex and free streptavidin. Compared to free streptavidin, the protein-nanoparticle complex elutes earlier and displays an elongated band. The elution time in native electrophoresis experiment is governed by the analytes morphological shape and charge, therefore earlier elution of the SNs-streptavidin complex is consistent with the extra negative charge due to linked SNs. The polydispersity in the eluted complex charge and molecular weight notably broadens conjugate gel features. One likely source of such polydispersity is silicon nanoparticle size polydispersity prior to conjugation [26] that is typical for SNs, produced by breaking up of the nanoporous silicon film. Also, variation in nanoparticle binding efficiency will result in conjugate composition distribution. Complexes with higher number of SNs per protein molecule will carry larger net negative charge and, consequently, will elute earlier. Additional experiments will be required to establish quantitative relation between the eluted band position and the conjugate molecular weight/charge ratio. Nevertheless, current gel result confirms the formation of the covalent SNs-protein complex and suggests the pathway for further conjugate purification. Gel electrophoresis demonstrates that SNs-streptavidin conjugates have higher negative net charge compared to the neat streptavidin (Fig. 3.4).

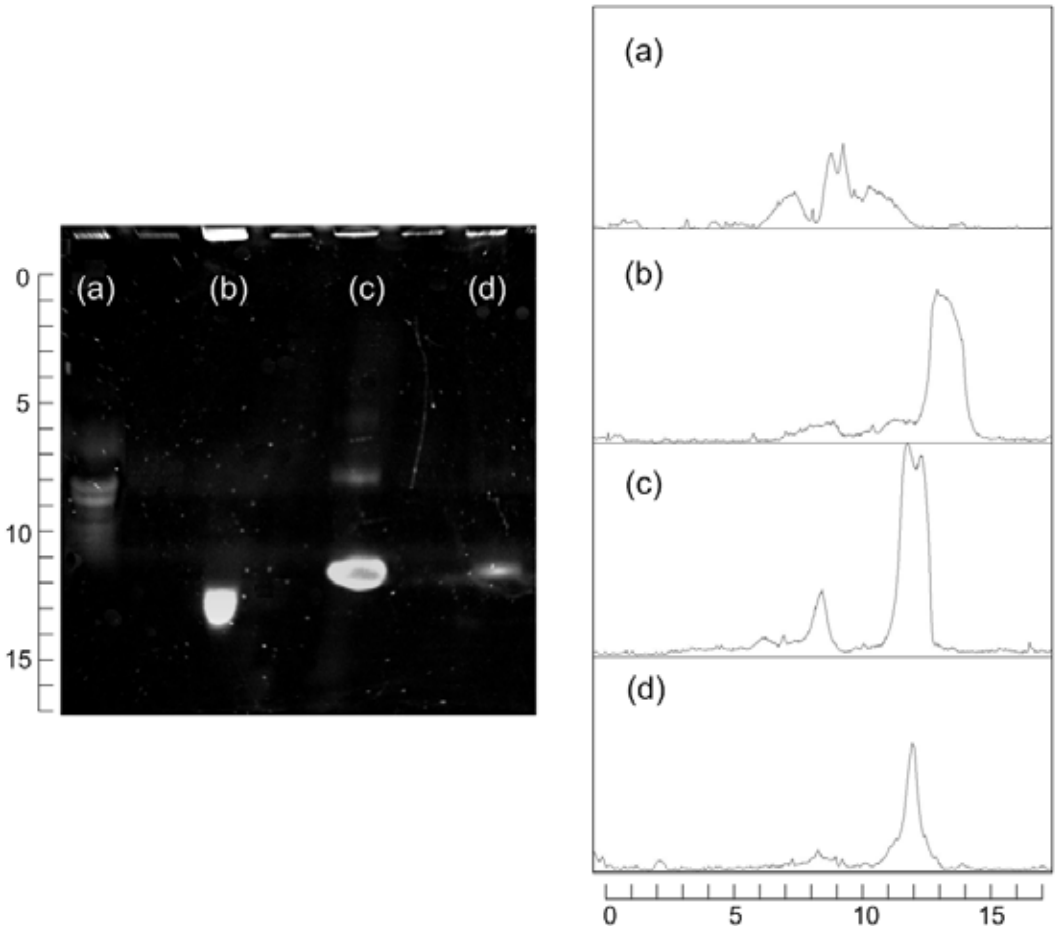

Figure 3.4 Native gel electrophoresis image and fluorescence intensity profiles from the eluted bands of neat streptavidin - (a), and SN - streptavidin conjugates - ((b), (c) and (d)). Variation of elution times between (b), (c) and (d) wells reflect different relative concentrations of the crosslinker tagged SNs to the streptavidin in the final reaction mix (v:v); (b) 1:2, (c) 1:1, and (d) 2:1. Electrophoresis conditions: U = 200V, t = 2 h. Mobile buffer: Tris-HCl, pH 8.0. Peaks between 8 to 9 represent neat streptavidin, and from 12 to 14 - conjugation products.

3.3.4 Number of SiNCs on each Streptavidin

Further analysis of the conjugation products was performed using capillary electrophoresis (CE). High sensitivity, small samples, and rapid elution facilitated CE application in various fields of analytical chemistry [31~34, for review, see ref. 31]. Recently, Eckhoff et al. demonstrated CE separation of amine functionalized silicon nanoparticles, using the fluorescence detection [33]. The analyte surface charge determines its mobility inside the CE capillary and allows charge based nanoparticle separations. Consequently, the elution time series, produced by UV absorbance detection, can be related to the discrete silicon nanoparticle charges. Separation of surface derivatized silicon nanoparticles, free streptavidin, and conjugate complex based on their net charge allows assessing the conjugation efficiency. Given that streptavidin charge varies with the coupled SiNCs number affects the elution time, it also allows to estimate the number of conjugated nanoparticles in the protein-SiNCs complex.

Both capillary and gel electrophoresis rely on charge mobility in the electric field, therefore we have maintained similar conditions in both experiments (buffer, pH, and temperature). In a first step we have determined the apparent velocities υ_{ap} for our sample components - SiNCs, streptavidin, SiNCs-streptavidin conjugates:

$$\upsilon_{ap} = \frac{L_{id}}{t_m} \qquad \text{(Eq. 3.1)}$$

where L_{id} - distance from the inlet to the detector, and t_m - travel time of the sample from inlet to the detector point in the capillary. In order to account for the electroosmotic component, we have calibrated our CE system using neutral molecule,

mesityl oxide, (SigmaAldrich Inc., St. Lewis, MO) at identical experimental conditions and have estimated the electroosmotic velocity, υ_{eo} (Eq. 3.2):

$$\upsilon_{eo} = \frac{L_{id}}{t_{m,n}} \qquad \text{(Eq. 3.2)}$$

Where υ_{eo} is electroosmotic velocity and $t_{m,n}$ is the time for a neutral to arrive at the detector. Consequently, the actual sample velocity inside the capillary (υ_{ac}), can be calculated from (Eq. 3.3):

$$\upsilon_{ac} = \upsilon_{ap} - \upsilon_{eo} = \frac{L_{id}}{t_m} - \frac{L_{id}}{t_{m,n}} \qquad \text{(Eq. 3.3)}$$

Sample mobility μ_{ep} is a product of velocity and electrical field inside the capillary $\mu_{ep} = \upsilon_{ac} E$, and can be calculated when the net charge q and Stokes radius r are both known (Eq. 3.4):

$$\mu_{ep} = \frac{q}{6\pi\eta r} \qquad \text{(Eq. 3.4)}$$

here η - solvent viscosity.

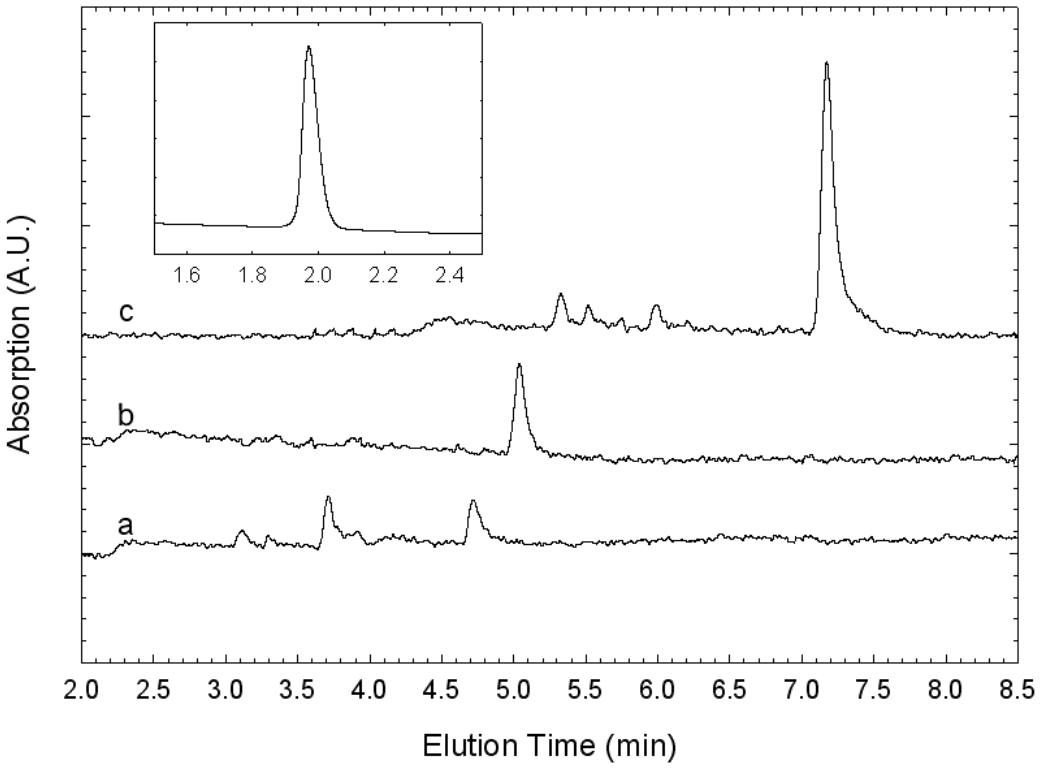

Figure 3.5 Capillary electrophoresis analysis of silicon nanoparticle/streptavidin conjugation reactants: (a) SiNCs with attached hetero bi-functional crosslinker (ATFB, SE), (b) neat streptavidin, (c) SiNCs-streptavidin conjugate. Inset shows the elution of a neutral molecule (Mesityl oxide, see text). Running buffer: Tris-glycine 0.2 M, pH 8, capillary dimensions: L = 50 cm, ID = 0.1 mm. Applied voltage: U = 20 kV, absorbance detector at 200 nm.

By combining equations 3 and 4, we obtain a relationship between the charge q and sample elution time, t_m (Eq. 3.5):

$$q = 6\pi \cdot \eta \cdot r \cdot \left(\frac{L_{id}}{t_m} - \frac{L_{id}}{t_{m,n}} \right) \cdot E \qquad \text{(Eq. 3.5)}$$

where electric field strength $E = V/L_t$, V - total applied voltage, and L_t - total capillary length. Consequently, based on equation 3.5, we can assign each detected CE peak a net charge value, and estimate the number of nanoparticles in the SNs-protein complex.

Figure 3.5 shows CE trace recorded using the UV absorbance detector (wavelength = 200 nm). Capillary inlet was connected to the anode, hence negative analytes will elute later than neutral or positive molecules. Silanol (Si-OH) groups of the silica capillary interior wall turn into negatively charged silanoates (Si-O-) at pH 8, and attract buffer cations, forming a positive solution layer. This layer is dragged toward the cathode due to the electroosmosis, while negatively charged analytes move in the opposite direction and experience a delayed elution (Fig. 3.5).

Four elution peaks on at 3.1, 3.3, 3.7 and 4.8 min (Fig. 3.5a) were analyzed within the range of expected nanoparticle size and surface charge. Based on the photoluminescence emission wavelength and nanocrystal size relationship [23], we have estimated that silicon particles with radii, $r < 0.84$ nm should be responsible for the observed blue photoluminescence of our samples (Fig. 2.2). However, a change in emission mechanism due to surface functionalization can markedly affect this relationship [30]. The two strongest elution peaks at 3.7 and 4.8 min were assigned net charges $q_1 = -1$ and $q_2 = -2$ that correspond to particles with $r_1 = 0.5$ nm and $r_2 =$

0.84 nm respectively. The elution peak of the neat streptavidin (Fig. 3.5, b, at time 5.2 min), corresponds to a net charge -13 at our experimental conditions (pH 8). Recently Bradley et. al. discussed the possible origin of the net negative streptavidin charge in basic solutions [29], and concluded that multiple exposed histidine residues are deprotonated at elevated pH. Notably, our CE derived protein charge estimate (q_{St} = -13 at pH 8.0) is consistent with the neat streptavidin zeta potential value (~50 mV) [35].

The strongest feature in Fig. 3.5, c (t = 7.2 min) corresponds to the net charge from -17 to -18, depending on the associated nanoparticle radius (0.5 or 0.84 nm), therefore, streptavidin molecule acquires an additional net charge from -4 to -5 due to silicon nanoparticle attachment.

3.3.5 Biotin-Streptavidin-SiNC conjugation

Strong association between streptavidin and biotin is widely exploited in biological assays, and we have to ensure that streptavidin retains its binding capacity after attachment to silicon nanoparticles. The fluorescence microscopy image in the right panel of the Fig. 3.6 (d) displays streptavidin/SiNCs conjugate binding to the biotinylated polystyrene micro-beads, following incubation as described in the experimental section. Comparison of images on Fig. 3.6 (a, b versus c, d panels), shows that the majority of complex exposed micro beads are associated with the photoluminescent silicon nanoparticles.

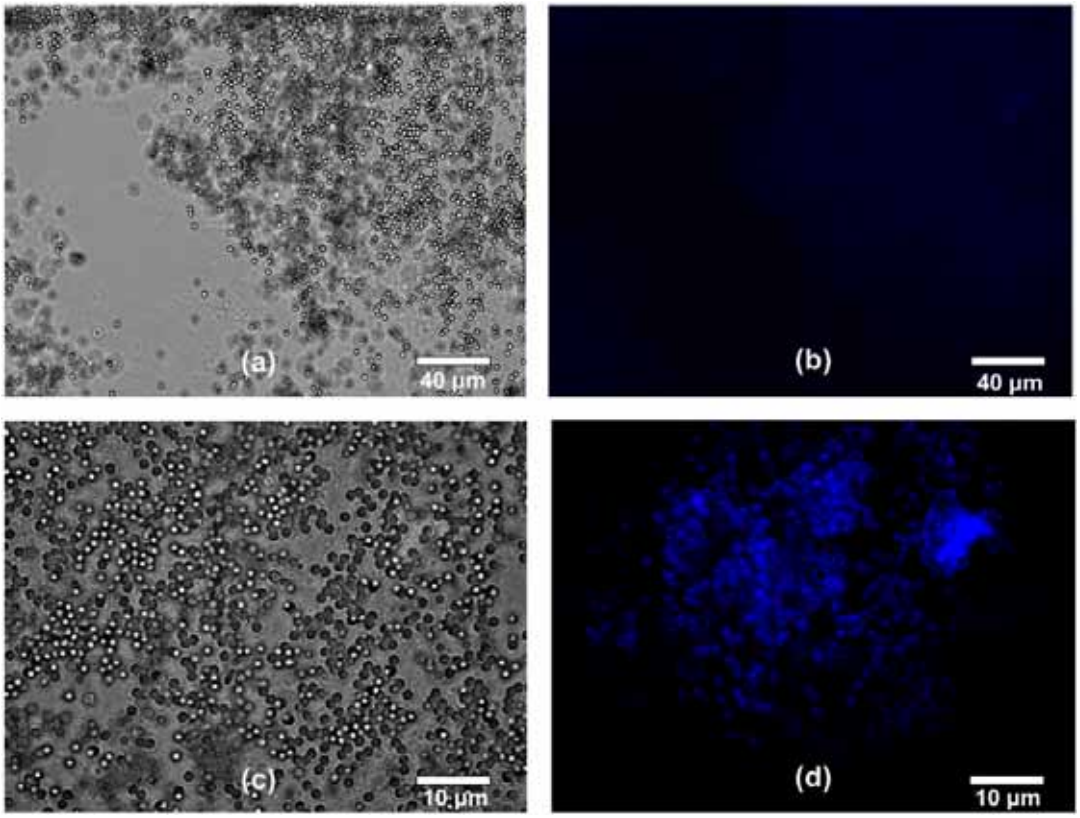

Figure 3.6 Fluorescence microscopy images of 2µm diameter biotinylated polystyrene micro beads, following their exposure to silicon nanoparticle – streptavidin complex: (a) - biotinylated polystyrene beads, exposed to the neat streptavidin (control) - phase image, and (b) - fluorescence image; (c) polystyrene beads exposed to a silicon nanoparticle-streptavidin complex - phase image, and (d) - fluorescence image.

The photoluminescence intensity variations between biotinylated beads reflect the heterogeneity in nanoparticle brightness and/or binding efficiency. A slight polystyrene bead aggregation, visible in c, d panels of Fig. 3.6 may be caused by the multivalent streptavidin-biotin interactions.

3.4 Summary

We have covalently coupled streptavidin with the photoluminescent silicon nanoparticles using a multistep photo-assisted reaction and a bifunctional cross-linker. The characteristic blue nanoparticle photoluminescence was retained in the silicon quantum dot-protein complex. Faster elution of the nanoparticle-streptavidin complex in the native gel electrophoresis indicates extra negative charge of the conjugate due to linked silicon nanoparticles. Typically from 4 to 5 silicon nanoparticles are bound to streptavidin molecule as determined from the capillary electrophoresis analysis. Streptavidin molecules retain their binding capability to the biotin subsequent to the conjugation protocol. Covalent attachment of small, efficient and non-toxic photoluminescent silicon quantum dots to streptavidin provides a convenient pathway for biomolecules labeling in biotin-streptavidin affinity based assays.

3.5 Reference

[1] Medintz, I. L., Uyeda, H. T., Goldman, E. R., and Mattoussi, H. (2005) Quantum dot bioconjugates for imaging, labelling and sensing. Nat. Mat. 4, 435-446.

[2] Klostranec, J. M., and Chan, W.C.W. (2006) Quantum dots in biological and biomedical research: recent progress and present challenges. Adv. Mater. 18, 1953-1964.

[3] Hermanson, G. T. (1996) Bioconjugate techniques, Academic Press, California.

[4] Alivisatos, P. (2004) The use of nanocrystals in biological detection. Nat. Biotechnol. 22, 47-52.

[5] Michalet, X., Pinaud, F. F., Bentolila, L. A., Tsay, J. M., Doose, S., Li, J. J., Sundaresan, G., Wu, A. M., Gambhir, S. S., and Weiss, S. (2005) Quantum dots for live cells, in vivo imaging, and diagnostics. Science 307, 538-544.

[6] Pathak, S., Choi, S., Arnheim, N., and Thompson, M. E. (2001) Hydroxylated quantum dots as luminescent probes for in situ hybridization. J. Am. Chem. Soc. 123, 4103-4104.

[7] Clarke, S. J., Hollmann, C. A., Zhang, Z., Suffern, D., Bradforth, S. E., Dimitrijevic, N. M., Minarik, W. G., and Nadeau, J. L. (2006) Photophysics of dopamine-modified quantum dots and effects on biological systems. Nat. Mat. 5, 409-417.

[8] Bäumle, M., Stamou, D., Segura, J., Hovius, R., and Vogel, H. (2004) Highly fluorescent streptavidin-coated CdSe nanoparticles: Preparation in water, characterization, and micropatterning. Langmuir 20, 3828-3831.

[9] Bottini, M., Cerignoli, F., Dawson, M. I., Magrini, A., Rosato, N., and Mustelin, T. (2006) Full-length single-walled carbon nanotubes decorated with streptavidin-conjugated quantum dots as multivalent intracellular fluorescent nanoprobes. Biomacromolecules 7, 2259-2263.

[10] Wu, S., Zhao, X., Zhang, Z., Xie, H., Tian, Z., Peng, J., Lu, Z., Pang, D., and Xie, Z. (2006) Quantum-dot labeled DNA probes for fluorescence in situ hybridization (FISH) in the microorganism Escherichia coli. ChemPhysChem 7, 1062-1067.

[11] Wolcott, A., Gerion, D., Visconte, M., Sun, J., Schwartzberg, A., Chen, S., and Zhang, J. Z. (2006) Silica-coated CdTe quantum dots functionalized with thiols for bioconjugation to IgG proteins. J. Phys. Chem. B 110, 5779-5789.

[12] Pellegrino, T., Manna, L., Kudera, S., Liedl, T., Koktysh, D., Rogach, A. L., Keller, S., Radler, J., Natile, G., and Parak, W. J. (2004) Hydrophobic nanocrystals coated with an amphiphilic polymer shell: A general route to water soluble nanocrystals. Nano Lett. 4, 703-707.

[13] Gao, X, Cui, Y., Levenson, R. M., Chung, L. W. K., and Nie, S. (2004) In vivo cancer targeting and imaging with semiconductor quantum dots. Nat. Biotechnol. 22, 969-977.

[14] Guo, W., Li, J. J., Wang, Y. A., and Peng, X. (2003) Conjugation chemistry and bioapplications of semiconductor box nanocrystals prepared via dendrimer bridging. Chem. Mater. 15, 3125-3133.

[15] Hardman, R. (2006) A toxicologic review of quantum dots: Toxicity depends on physicochemical and environmental factors. Environ. Heal. Persp. 114, 165-172.

[16] Derfus, A. M., Chan, W. C. W., and Bhatia, S. N. (2004) Probing the cytotoxicity of semiconductor quantum dots. Nano Lett. 4, 11-18.

[17] Fischer, H. C., Liu, L. C., Pang, K. S., and Chan, W. C. W. (2006) Pharmacokinetics of nanoscale quantum dots: In vivo distribution, sequestration, and clearance in the rat. Adv. Func. Mat. 16, 1299-1305.

[18] Tsay, J. M., and Michalet, X., (2005) New light on quantum dot cytotoxicity. Chem. & Bio. 12, 1159-1161.

[19] Kirchner, C., Liedl, T., Kudera, S., Pellegrino, T., Javier, A. M., Gaub, H. E., Stolzle, S., Fertig, N., and Parak, W. J. (2005) Cytotoxicity of colloidal CdSe and CdSe/ZnS nanoparticles. Nano Lett. 5, 331-338.

[20] Wang, L., Reipa, V., and Blasic, J. (2004) Silicon nanoparticles as a luminescent label to DNA. Bioconjugate Chem. 15, 409-412.

[21] Ding, Z., Quinn, M. B., Haram, A. K., Pell, L. E., Korgel, B. A., and Bard, A. L. (2002) Electrochemistry and electrogenerated chemiluminescence from silicon nanocrystal quantum dots. Science 296, 1293-1297.

[22] Warner J. H., Hoshino, A., Yamamoto, K., and Tilley, R. D. (2005) Water-soluble photoluminescent silicon quantum dots. Angew. Chem. Int. Ed. 44, 4550-4554.

[23] Warner J. H., Hoshino, A., Shiohara, A., Yamamoto, K., and Tilley, R. D. (2006) The Synthesis of silicon and germanium quantum dots for biomedical applications. Proc. of SPIE 6069, 6096071-6096078.

[24] Buriak, J.M. (2002) Organometallic chemistry on silicon and germanium surfaces. Chem. Rev. 102, 1271-1308.

[25] Sato, S., and Swihart, M. T., (2006) Propionic-acid-terminated silicon nanoparticles: Synthesis and optical characterization. Chem. Mater. 18, 4083-4088.

[26] Choi, J., Wang, N. S., and Reipa, V. (2007) Photoassisted tuning of silicon nanocrystal photoluminescence. Langmuir 23, 3388-3394.

[27] Jung, K. H., Shih, S., Hsieh, T. Y., Kwong, D. L., and Lin T. L. (1991) Intense photoluminescence from laterally anodized porous Si. Appl. Phys. Lett. 59, 3264-3266.

[28] Belomoin, G., Therrien, J., Smith, A., Rao, S., Twesten, R., Chaieb, S., Nayfeh, M. H., Wagner, L., and Mitas, L. (2002) Observation of a magic discrete family of ultrabright Si nanoparticles. Appl Phys. Lett. 80, 841-843.

[29] Bradley, K., Briman, M., Star, A., and Gruner, G. (2004) Charge transfer from adsorbed proteins. Nano Lett. 4, 253-256.

[30] Hua, F.J., Erogbogbo, F., Swihart, M.T., and Ruckenstein, E. (2006) Organically capped silicon nanoparticles with blue photoluminescence prepared by hydrosilylation followed by oxidation. Langmuir 22, 4363-4370.

[31] Rodriguez, M. A., and Armstrong, D. W. (2004) Separation and analysis of colloidal/nano-particles including microorganisms by capillary electrophoresis: a fundamental review. J. Chrom. B. 800, 7-25.

[32] Yu, C., Su, C., and Tseng, W. (2006) Separation of acidic and basic proteins by nanoparticle-filled capillary electrophoresis. Anal. Chem. 78, 8004-8010.

[33] Eckhoff, D. A., Stuart, J. N., Sutin, J. D. B., Sweedler, J. V., and Gratton, E. (2006) Capillary electrophoresis of ultrasmall carboxylate functionalized silicon nanoparticles. J. Chem. Phys. 125, 0811031-0811034.

[34] Huang, X., Weng, J., Sang, F., Song, X., Cao, C., and Ren, J. (2006) Characterization of quantum dot bioconjugates by capillary electrophoresis with laser-induced fluorescent detection. J. Chrom. A. 1113, 251-254.

[35] van Oss, C. J., Giese, R. F., Bronson, P. M., Docoslis, A., Edwards, P., and Ruyechan, W. T. (2003) Macroscopic-scale surface properties of streptavidin and their influence on aspecific interactions between streptavidin and dissolved biopolymers. Colloids Surf., B 30, 25-36.

Chapter 4: Biological Responses of Silicon Nanocrystals

4.1 Introduction

Technology is now available to produce nanoparticles of uniform size and shape which may allow nanoparticles to be used in a wide range of applications from drug delivery to water purification [1]. Production and exposure of nanoparticles less than 100 nm in diameter may pose unknown risks since the responses of biological systems to novel materials of this size have not been adequately studied. The high surface area to volume ratio makes nanoparticles particularly good catalysts and such particles readily adhere to biological molecules. The size and surface charge of nanoparticles enable them to access places where larger particles may be blocked, including passage through cellular membranes [2-3]. However, the wider application of semiconductor quantum dots as biological probes has been held back by their inherent chemical toxicity, which necessitates encapsulating them in a robust inert shell which increases the diameter of the probe [3].

Although there are studies [4-5] on both known and unknown hazards of several kinds of nanoparticles (for reviews see ref. 4), many questions remain unanswered. Furthermore, there are few systematic studies dealing with both cytotoxicity and inflammatory responses of cells treated with nanoparticles. How will a biological system react when exposed to nanoparticles? What is the fate of the nanoparticles once they are presented to a population of cells? If the nanoparticles enter into the cell,

what effects do they exert internally? These questions must be answered in order to ensure safety to the patient if nanoparticles are incorporated in biomedical applications. We attempt to address these questions by studying the cytotoxicity and biological interactions of cells with silicon nanoparticles (SNs).

SNs are increasingly being studied due to their unique physicochemical properties [6], including efficient photoluminescence in the visible part of the electromagnetic spectrum and their chemical stability. A deeper understanding in related phenomena in II-VI compound semiconductor quantum dots and successful applications in bioresearch have re-energized interest in the nanoscale Si. SNs are of interest as a biomarker because they are potentially bioinert and do not require a thick protective shell.

A straightforward SN preparation procedure based on electrochemical Si wafer etching [7] closely follows the protocols developed for obtaining nano-porous Si [8]. Briefly, anodic wafer etching is followed by sonication that partially crumbles porous Si film, resulting in a nano-particle suspension. Immediately after etching, the particle surface is hydrogen passivated and can be subsequently oxidized or substituted with a variety of organic groups via post-etching functionalization [9].

Because SNs may be incorporated in future biomedical applications, we assess their cytotoxicity and biological responses of SNs in a murine macrophage cell system. Probing inflammatory responses from cells treated with nano sized materials is important to ensure that these materials will be safe in terms of cytotoxicity and cytokine stimulation [10]. Brown et al. [10c] showed that monocytic cells incubated with carbon nanotubes did not show cytotoxicity but stimulated the release of

cytokines. Polytetrafluoroethylene (PTFE) based medical devices in human body brought about severe inflammation when abrasion of the surfaces of devices made of PTFE generated small wear particles [10a, 11]. Now, PTFE is no longer considered as "an appropriate material to use as a load-bearing surface in the body" [12].

Macrophages play a pivotal role in the inflammatory process [10, 13]. They can engulf or phagocytocize foreign materials and can produce cytokines to recruit other immune cells to respond [10a]. Kim et al. [13a] reported that a rapid inflammation sensor system consisting of RAW 264.7 macrophage and HeLa cell is promising because macrophages are well known in immune responses. The ASTM developed a standard method for testing for biological responses to particles *in vitro* using murine macrophages [14]. However, it is not clear whether standard toxicity protocols written for micron-sized particles are applicable to nano-sized biomaterials and products. In addition, there is an international standard (ISO 10993, Biological Evaluation of Medical Devices) which describes various tests for assessing biological responses to medical device materials. There are many products that incorporate nanoparticles which the United States Food and Drug Administration (USFDA) must regulate and decide if they are safe and effective for their intended use. Since the use of 1-100 nm nanoparticles may result in unknown biological risks and since there is no clear confirmation that established standard test protocols are appropriate, it is important to study the potential cytotoxicity and inflammatory response of nano-sized particles *in vitro* and *in vivo* such that patient safety can be assessed.

We compare biological responses of cells to SNs with responses to commercially available silicon microparticles (SMs). Following incubation of murine macrophage

cells in SNs and SMs, we monitored cell morphology and cytotoxicity together with production of nitric oxide (NO), intereukin-6 (IL-6) and tumor necrosis factor-alpha (TNF-α), macrophage generated molecules that reflect inflammatory responses. Lipopolysaccharide (LPS) was added alone or with SN and SM. LPS is a positive control for nitric oxide and cytokine production by macrophages. Also, the addition of LPS to particles may show an additive or synergistic effect of the biological responses to particles in the macrophage. The location of SNs in cells was examined with fluorescence microscopy. We attempt to address whether the particles inside the cells induce specific cell killing and elicit inflammatory responses.

Dry-heat sterilization at 300°C of nano and micro particles renders them endotoxin-free and sterile. It is important to start with sterile and endotoxin-free nano and micro particles when studying them for biological responses, especially for inflammatory potential. It should be noted that in these experiments, the macrophage growth media contained no antibiotics, which could mask bacteria and fungi that potentially stimulate inflammatory macrophage responses and this lead an observer to conclude erroneously that a given material itself is inflammatory.

The goal of this study was to compare biological responses of macrophages to SNs with responses to silicon microparticles (SMs).

4.2 Materials and Methods

4.2.1 Thermal treatment of nano and micro particles

SNs were synthesized using an electrochemical etching of silicon wafers followed by an ultrasound treatment (Yamani et al., 1998; Choi et al., 2007; Choi et al., 2008a; 2008b). A suspension of SNs was delivered to a glass, sterile Petri dish for a thermal sterilization treatment. After a complete evaporation of ethanol through vigorous N_2 purging, we placed dried SNs in the furnace in N_2 environment at 300ºC for 20 min in order to sterilize and make them endotoxin-free. Next, SNs were redispersed in sterile, endotoxin-free water (Sigma, St. Louis, MO) at a concentration up to 2 mg/ml for incubation with macrophage cells. Nanoparticles (3~5 nm diameter) retained orange photoluminescence following this treatment. SMs were purchased (~100-3000 nm diameter, Sigma, St. Louis, MO) and were thermally treated in the same manner as SNs. SMs were redispersed in sterile, endotoxin-free water at a concentration of 2 mg/ml.

4.2.2 Characterization of nano/micro particles

Photoluminescence (PL) was recorded using a spectrofluorimeter (model LM800, SLM Inc., Urbana, IL) with an excitation filter setting of 360 nm. SNs and SMs were deposited on PTFE IR cards (ICL, Garfield, NJ) and delivered to a Fourier transform infra red (FT-IR) spectrometer (IFS 66, Bruker optics Inc., Billerica, MA) in order to evalutate the surface chemical composition. Nanoparticle suspensions were dropped on a carbon film copper grid (Ted Pella Inc., Redding, CA) and dried completely for transmission electron microscopy. High resolution transmission electron microscopy

(HrTEM) was conducted with a JEOL 2100F field emission transmission electron microscope (JEOL Ltd., Tokyo, Japan). Element composition analysis of SN-incubated cell samples were determined using energy dispersive x-ray spectroscopy (EDS, INCAx-sight, Oxford Ins., Dynamic light scattering of SNs and SMs was studied using zeta potential analyzer (ZetaPALS, Brookhaven Ins., Holtsville, NY).

4.2.3 Cell culture

RAW 264.7 murine macrophages (TIB 71, American Type Culture Collection, Manassas, VA) were grown in RPMI-1640 (Invitrogen, Irvine, CA), containing 10% fetal bovine serum (FBS; Hy-Clone, Logan, UT) and 1% L-glutamine (complete media) and seeded in two 24-well plates at a starting density of 10^5 cells/well and grown in a 37^o C, 5% CO_2-95% air, 90% relative humidity incubator prior to addition of particles, or lipopolysaccharides (LPS).

4.2.4 Nano/micro particle incubation with cells

Aliquots of either aqueous SN or SM suspensions at concentrations of 0.1 ~ 200 μg/ml were gently added to the cells in two 24-well plates. In order to ensure that the particles were in contact with the macrophages, the media was removed and the particles in solution were gently layered directly onto the macrophage surface. Then the complete media was carefully placed back into each well, and the plates were returned to the incubator. LPS (1 ng/ml; *E. coli*, 0127:B8, Sigma-Aldrich, St. Louis, MO) was added either alone to cells or to cells with SNs or SMs. After 24h and 48h incubation, we took one plate and observed the morphological changes to the cells

and measured cytotoxicity by Trypan blue dye exclusion and MTT assay. Cells were enumerated using a hemocytometer. Supernatants from each well were collected and stored at minus 80^{o}C until assayed for production of NO and the cytokines TNF-α and IL-6.

4.2.5 Trypan blue dye assay

Cells on the bottom of the plate were washed with Dulbecco's phosphate buffer without calcium and without magnesium solution (PBS; Invitrogen, Carlsbad, CA). Following washing, cells were dislodged from the plates with trypsin EDTA (0.5% trypsin and 5.3 mM EDTA, Invitrogen, Carlsbad, CA). Complete medium was added to each well in order to stop the action of trypsin. Cells were then stained with 0.2% trypan blue dye (Invitrogen, Carlsbad, CA) and viable versus non-viable cells were counted using a hemocytometer. Morphological changes of cells after 24 and 48 hours incubation with SNs and SMs were observed. Cytotoxicity was based on percentage of dead cells against controls (cells given no particles).

4.2.6 MTT assay

Macrophages were seeded in 96-well plates and grown for 24h. SNs and SMs were introduced into the wells with the concentration series of 1 to 200 μg/ml and incubated for another 24h. The media was removed and cells were washed with PBS. The dye solution (15μl, CellTiter 96® non-radioactive cell proliferation assay, Promega, Madison, WI) was added to each well. The 96-well plates were incubated in a humidified, 5% CO_2 incubator at 37^{o}C for 2h. Next, 100μl of the solubilization

solution was added to the wells and then the plates were kept in the dark for an hour at room temperature. After brief gentle mixing of contents in each well, the absorbance of each well was recorded at 570 nm using a 96-well plate reader (SpectraMax 190, Molecular Devices, Sunnyvale, CA).

4.2.7 Nitric oxide DAN assay

The amount of nitric oxide was measured in supernatants from cells treated with SNs and SMs with and without LPS. A DAN (2,3-diaminonaphthalene) fluorescent dye (Sigma, St. Louis, MO) was used to selectively detect nitric oxide produced by the cells. Serial dilutions of nitrite standard solutions were made with nitrite concentrations from 0.19 to 25 μM. Thawed supernatants from cells treated for 48h with no particles or LPS (control), SNs with and without LPS, and SMs with and without LPS were assayed. To each well, 20 μl of supernatant samples or nitrite standards was added. Deionized water (80 μl) was added to each well of a 96-well plate. After addition of all samples and the nitrite standards, 10 μl of 50 μg/ml DAN was added to each well, and then gently mixed. The plate was subsequently placed in the dark for 10 min at room temperature and then 20 μl of 2.8 M NaOH was added to each well. The plates were gently shaken to mix and then placed in the dark for another minute. The amount of nitric oxide present in each well was measured with a Spectra Max Gemini EM fluorescence plate reader (Molecular Devices, Sunnyvale, CA) with an excitation of 360 nm and an emission of 430 nm and calculated against the standard curve. Each supernatant was assayed in duplicate and all experiments were repeated 3 times.

4.2.8 IL-6 and TNF-α assays

IL-6 and TNF-α assay were measured in supernatants from cells treated with SNs and SMs for 24h. Quantikine mouse IL-6 and TNF-α immunoassay kits (R&D Systems, Minneapolis, MN) were used to measure IL-6 and TNF- α. Serial dilutions of standard amounts of murine IL-6 and TNF-α (R&D Systems, Minneapolis, MN) were prepared and pipetted into the 96-well plates pre-coated with immobilized antibodies. Supernatants from all the control and treated cells were added to the wells. After a 2h reaction time, the wells were washed and polyclonal antibodies specific for mouse IL-6 and TNF-α were added to the wells. After another 2h reaction period wells were completely washed to remove any unbound reactants. The amount of IL-6 and TNF-α present in each well was determined by measuring the proportion of fluorescence intensities in the samples. The amount produced by the cells was calculated from the standard curve of known amounts of murine IL-6 and TNF- α.

4.2.9 Fluorescence microscopy

Fluorescent SNs associated with cells were observed under a fluorescence microscope, equipped with a suitable filter set (excitation wavelength of 350 nm and emission wavelength of 600 nm). Cells were incubated with 20 μg/ml nanoparticles in a chamber slide (Nunc Lab-Tek II, Fisher Scientific, Pittsburgh, PA) for 24h in a 37ºC and 5% CO_2-95% air incubator. Following the incubation, the cells were washed 3 times with PBS to remove any nonbinding SN particles. After the final wash, cells were observed with an Olympus BX 50 fluorescence microscope (Olympus America,

Inc., Center Valley, PA). Fluorescence images were acquired with a SPOT-RT KE digital camera (Diagnostic Instruments, Sterling Heights, MI) and processed using image analysis software (SPOT, version 4.0, Diagnostic Instruments, Sterling Heights, MI).

Z stack of fluorescence images are obtained from RAW macrophages treated with SNs for 24h on the chamber slides with cover (cat#: 154526, lab-tek II chamber slide w/cover RS glass slide sterile, size 4 well, Sigma-Aldrich, MO). After 24h incubation, chamber was opened and cell's nucleus was stained with an aliquot of 4′,6-diamidino-2-phenylindole, dihydrochloride (DAPI) (cat# D1306, Invitrogen, CA).

Zeiss observer Z1, with apotome (Carl Zeiss, Jena, Germany) at National Eye Institute (NEI at National Institute of Health, Bethesda, MD) equipped with DAPI filter set was used to analyze Z axis oriented fluorescence. The stage moved up and down to take slices of high resolution fluorescence images. Obtained images are processed with AxioVision (ver. 4.7, Carl Zeiss, Jena, Germany) for analytical localization of particles inside cells.

4.2.10 Statistical analysis

All experiments were performed in duplicate and repeated at least 3 times. The statistical significance of the data was determined by the standard t-test.

4.3 Results and Discussion

4.3.1 Surface heat treatment

Dry-heat sterilization at 300°C of nano- and microparticles renders them endotoxin-free and sterile. The importance of conducting experiments with sterile and endotoxin-free nano- and microparticles when evaluating potential biological responses, in particular for examining and measuring inflammatory potential, cannot be overstated. It should be noted that in these experiments, the macrophage growth media contained no antibiotics, which could mask bacteria and fungi that may potentially stimulate inflammatory responses by macrophages and this lead an observer to conclude erroneously that a given material itself is inflammatory.

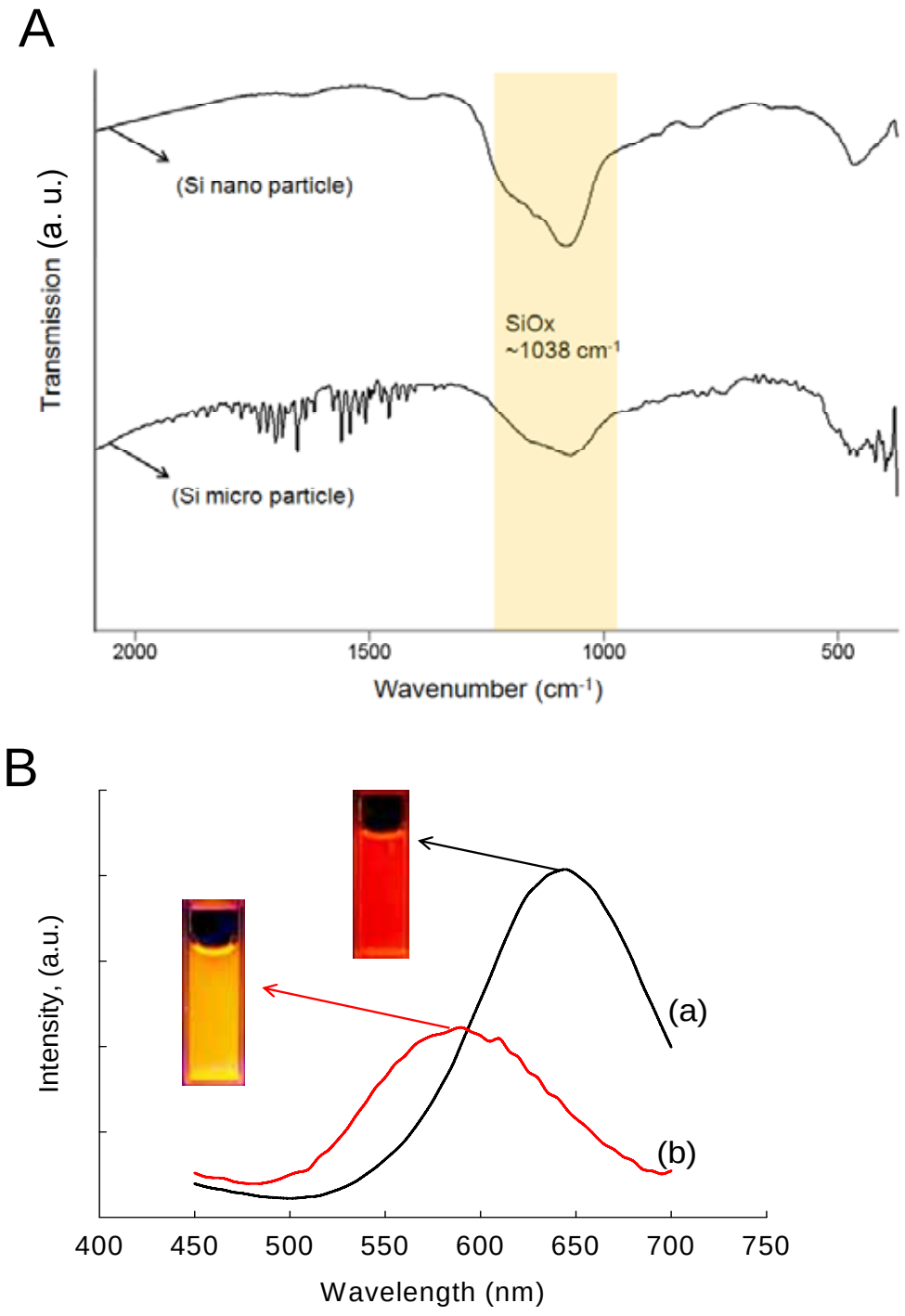

Figure 4.1 (A) FT-IR spectra of silicon nano- and microparticles. Silicon oxide band (~1038 cm^{-1}) was dominant in both nano- and microparticle spectra after thermal sterilization. (B) Photoluminescence spectra and images of silicon nanoparticles before (a) and after (b) 300 °C thermal treatment.

At the end of dry-heat sterilization, particles of both size ranges are similarly partially oxidized as evidenced by the strong vibrational feature at ~1038 cm^{-1} in the FTIR spectra (Fig. 4.1 A). A slight decrease of the fluorescence intensity and the blue-shift of the emission spectra of SNs are observed when hydrogen termination is replaced by oxide species. (Fig. 4.1 B).

4.3.2 Particle size analysis

Nanoparticle shape and size were examined under high resolution transmission electron microscopy (TEM, Fig. 4.2 A). TEM image analysis confirmed the presence of spherical 3~5 nm SNs. Energy dispersive X-ray spectra of SNs (Fig. 4.2 B) show the presence of Si and O elemental peaks. The Cu features are an artifact from the sample grid. The average sizes of SNs and SMs were acquired based on measurements from dynamic light scattering (Fig. 4.2 C). SNs suspension demonstrated a narrow size distribution with a mean diameter $d = 3.0 \pm 1.0$ nm, while SMs had a significantly broader size distribution with the diameter ranging from 100 - 3000 nm. The degree of nanoparticle aggregation in a solution was determined by dispersing thermally oxidized SNs in different solvents: sterilized water, phosphate buffered saline (PBS), and RPMI-1640 media (with 10% fetal bovine serum). While SNs in PBS and RPMI-1640 media became aggregated, precipitated, and lost their fluorescence after a week, SNs dissolved in water remained dispersed for at least three weeks.

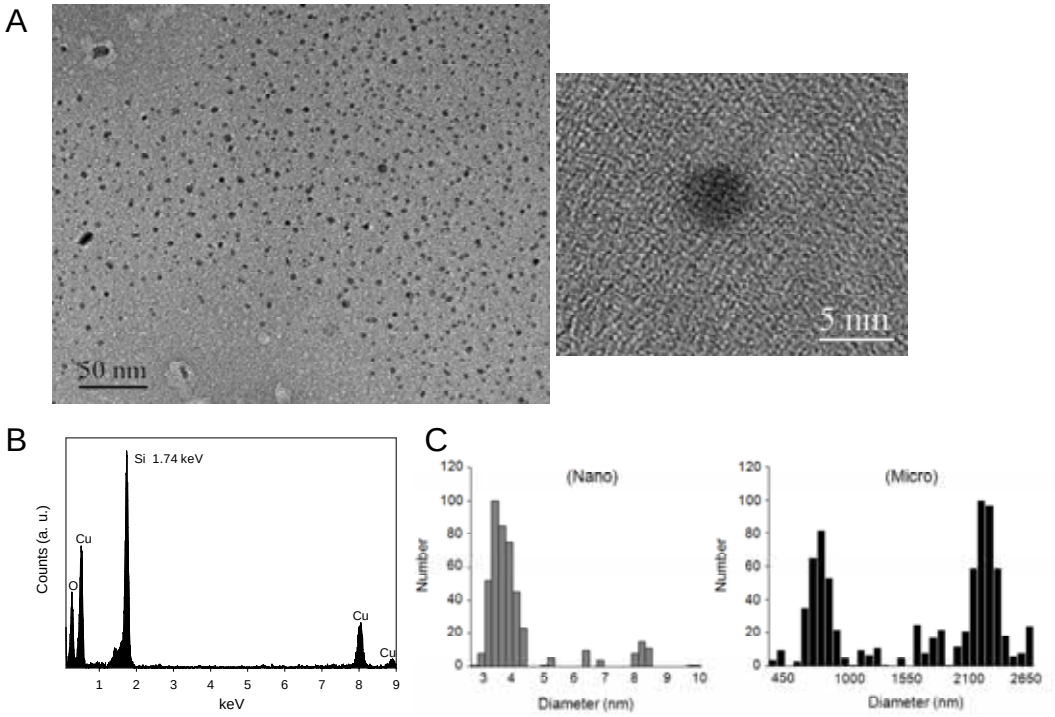

Figure 4.2 (A) High resolution transmission electron microscopy (HrTEM) of thermal treated Si nanoparticles. (B) Energy dispersive X-ray spectroscopy (EDS) of Si nanoparticles shown in (A) for an analysis of the elemental composition Spectra contained intense Si (1.74 keV), O (0.53 keV) and TEM substrate Cu (0.83, 8.05, and 8.90 keV) peaks. (C) Size distribution histograms obtained from the dynamic light scattering measurements of Si nano and microparticles.

4.3.3. Cytotoxicity of silicon nanoparticles

The morphology of cells did not change significantly after 24h and 48h incubation with nanoparticles. However, there were an increasing number of detached cells from the culture plate for cells exposed to higher nanoparticle concentrations (> 20 μg/ml). The morphology of the cells changed from a slim to a rotund shape for higher concentrations of nanoparticles. Based on these observations, the cytotoxicity of Si particles begins at particle concentrations >20μg/mL for SNs and >200μg/mL for SMs.

The qualitative observations of cytotoxicity at different concentrations of particles were confirmed with trypan blue dye exclusion and MTT assays. In this study, two different size range particles (SNs and SMs), with or without LPS, were tested under identical experimental conditions to clarify the role particle size plays in cytotoxicity. LPS is a positive inducer of NO and cytokines, and particles in the presence of LPS may exhibit a synergic or additional effect on production of NO, IL-6 and TNF-α. Figure 4.3 summarizes cell survival percentage after 24h and 48h exposures to SNs and SMs.

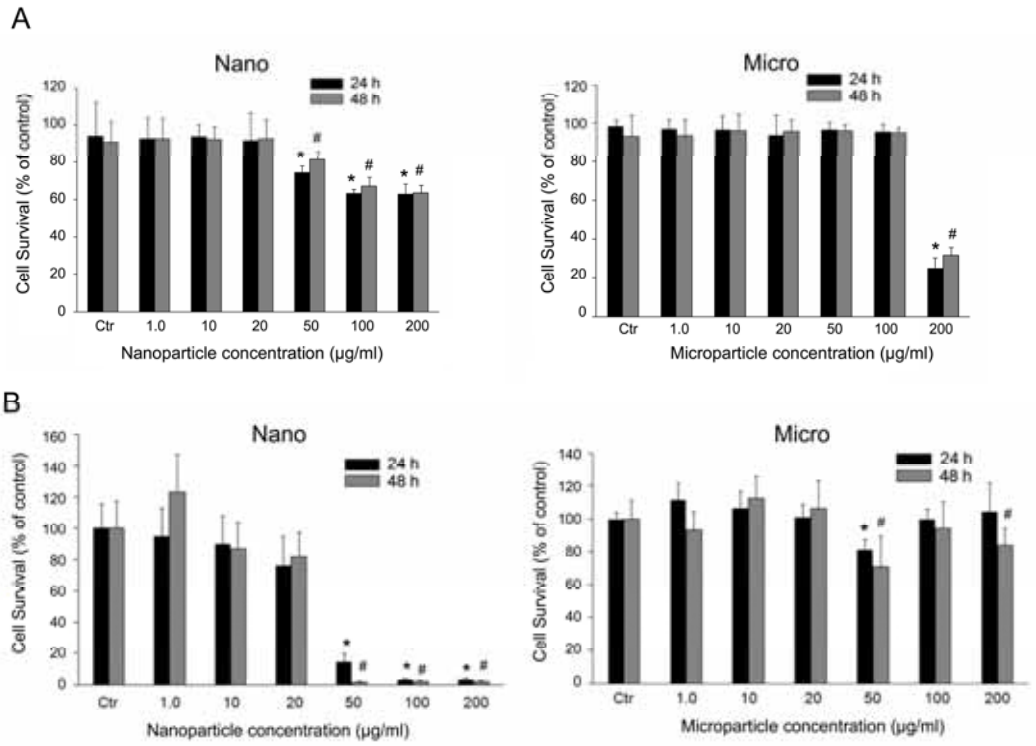

Figure 4.3 Effect of SNs and SMs on cell survival percentage in RAW 264.7 cells based on trypan blue dye exclusion (A) and MTT (B) assay. Cells were treated with different concentrations (0.1-200 µg/ml) of SNs and SMs for 24 and 48 h. At the end of exposure period, trypan blue stain was added to an aliquot of cells to assess the cell live/dead ratio (A). MTT was introduced into wells containing cells incubated for 24h or 48 hr with SNs or SMs measured with a fluorescence plate reader. * and # indicate a statistical difference from the control, $p<0.05$.

Cytotoxicity of nanoparticles starts to be pronounced at SN concentrations greater than 20 μg/ml while cytotoxicity of SMs starts at 10 times higher concentrations (200 μg/ml) (Fig. 4.3). There was no statistically significant difference in cell survival between control (no nanoparticles) and up to 20 μg/ml of nanoparticle. After 48h incubation, percent survival of RAW cells with LPS dropped only 4-5% (data not shown). A previous report demonstrated that at 1 ng/ml of LPS, a slight decrease of cell viability is observed in RAW cells (Chapekar et al, 1996). The percentage of live cells incubated in all SN concentrations studied here was within 85 ~ 92% in the absence of LPS. Therefore, the survival percentage of cells indicates that they were healthy even though there were nanoparticles around them at concentrations less than 20 μg/ml.

Macrophage exposure time to particles may not be a critical factor for cytotoxicity. Cell survival was similar for both 24h and 48h incubations (red and blue lines of Fig. 3.3 A) for both particle size ranges studied. Macrophages incubated for 24h with particles had ample time to interact with the particles. After LPS was introduced into these samples (data not shown in Fig. 4.3), cell survival was not affected. A decrease in cell survival for higher concentrations of SNs demonstrates that the toxic effect increases with increasing amounts of nanoparticle presented to the macrophage cells. A change in the morphology from normal to abnormal appearance is observed along with a decrease in the number of cells attached on the culture plate after PBS washing and an increase in the production of NO and the two cytokines IL-6 and TNF-α.

4.3.4 Inflammatory responses of silicon nanoparticles

The effect of SNs and SMs on production of inflammatory mediator NO and cytokines (IL-6 and TNF-α) in macrophage, is shown in Fig. 4.4. NO radicals are produced by three different nitric oxide synthases (NOS). While neuronal and endothelial types of NOS are expressed constitutively, the inducible NOS (iNOS) is induced by endotoxins during inflammatory processes (Moshage, 1997). NO levels in supernatants of cells incubated with SNs and SMs were not different from control (no particles, no LPS). LPS alone enhanced the production of NO but co-exposure with SNs and SMs did not alter the response in a concentration-dependent manner (Fig. 4.4 A).

In contrast to the unremarkable response of SNs and SMs on NO production, exposure to SMs produced a concentration-related increase in IL-6 and TNF-α production (Fig. 4.4 B~C). Similar responses have been demonstrated for micro-sized particles of other materials, such as polytetrafluoroethylene (Chepakar et al., 1996) and cadmium oxide (Goering et al., 2000). No changes were observed in production of TNF-α and IL-6 for SNs at concentrations ≤ 20 μg/ml. However, in contrast to the responses to SMs, the production of IL-6 and TNF-α was decreased at concentrations greater than 20 μg/ml (Fig. 4.4 B~C). The substantial decrease of IL-6 and TNF-α over controls with higher concentrations of nanoparticles may be due to a decrease in number of live cells, which was observed in the cytotoxicity assays (Fig. 4.4). It is not evident why IL-6 and TNF-α productions are slightly down-regulated; this response may be a manifestation of a latent form of nanoparticle cytotoxicity and future studies may elucidate the underlying mechanism.

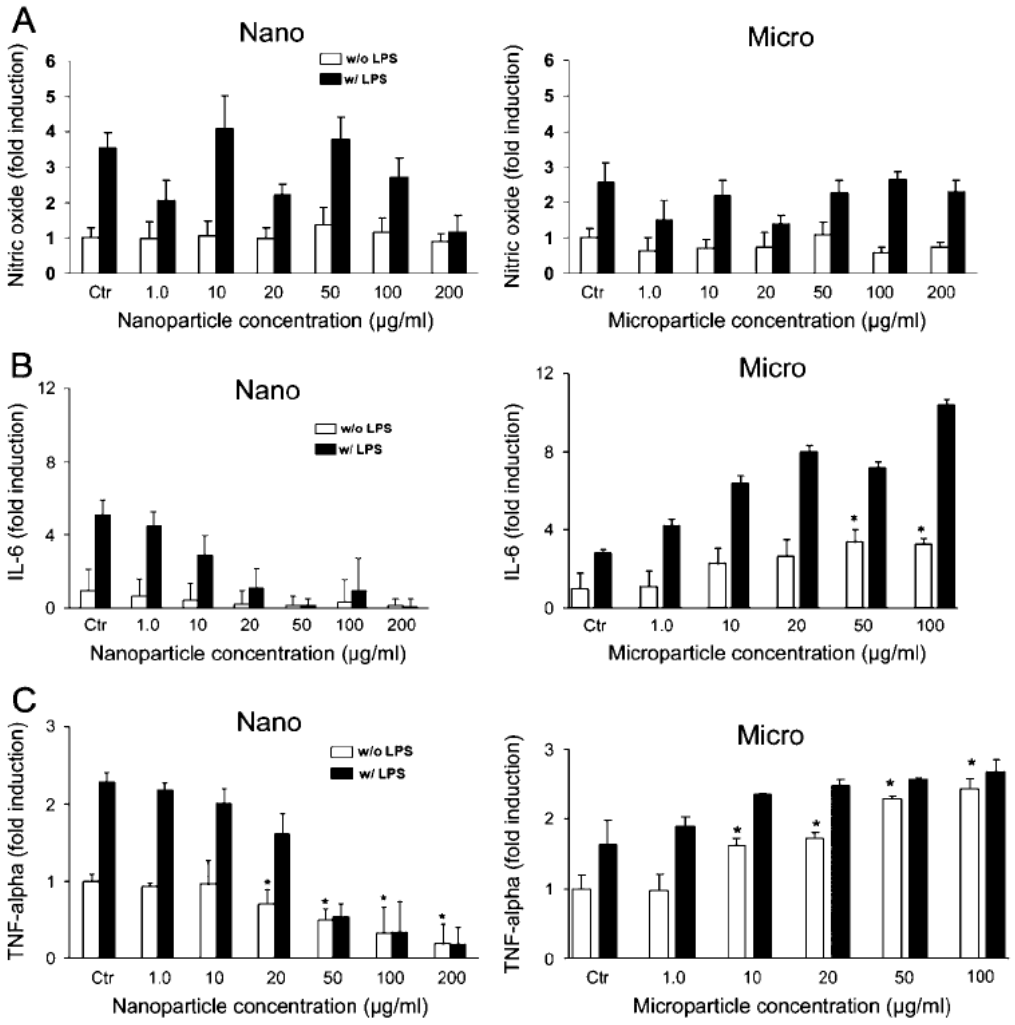

Figure 4.4 (A) NO production in RAW macrophages treated with SNs or SMs with and without LPS. NO secretion in the media was assessed using the DAN nitric oxide fluorescent assay. The white bar shows NO levels for samples without LPS injection, and black bar represents samples with SNs or SMs in the presence of 1 ng/ml LPS. (B) IL-6 and (C) TNF-α production in RAW 264.7 cells; SNs (1-200 μg/ml) and SMs (1-100 μg/ml) were incubated for 24 h. * indicates a statistical difference to the levels in the supernatants in the control, $p<0.05$.

4.3.5 Nanoparticle localization in the cell

The potential association of the photoluminescent SNs with the macrophages was assessed using fluorescent microscopy (Fig. 4.5). The RAW 264.7 macrophage is an immune cell that is known to recognize foreign materials such as microparticles and will engulf or phagocytize them as a way to destroy or remove them from the body. An overlay image (Fig. 4.5 iii) of the fluorescent image (Fig. 4.5 ii) with the bright field image (Fig. 4.5 i) demonstrates that the fluorescent SNs are associated with the macrophages. As expected, phase and fluorescence images from the control (Fig. 4.5 A) with no SNs present show no fluorescence.

Overlay of fluorescence and phase images showing association of SNs may provide an explanation of the inflammatory responses by macrophages exposed to nanoparticles (Fig. 4.4). Since some SNs do not fluoresce (quantum yield of SNs is 20-40%), there may be a sizeable fraction of non-fluorescent SNs which are positioned around as well as inside the cell but are not detected by fluorescence microscopy. More fluorescence images of RAW with SNs are shown in Figure 4.6. L929 fibroblast cells are also studied with the same condition to compare their uptake with RAW cells' results.

Figure 4.7 describes z stack of fluorescence image taken from cells exposed to the nanoparticle. Each blue dyed portion is responsible for cell's nucleus while red color is coming from silicon nanoparticles. Side view of florescence image (Fig. 4.7. A) shows clear indications of internalized SNs. 3-D rendered z stack images (Fig. 4.7. B) also clarifies red fluorescence is from particles inside the cell.

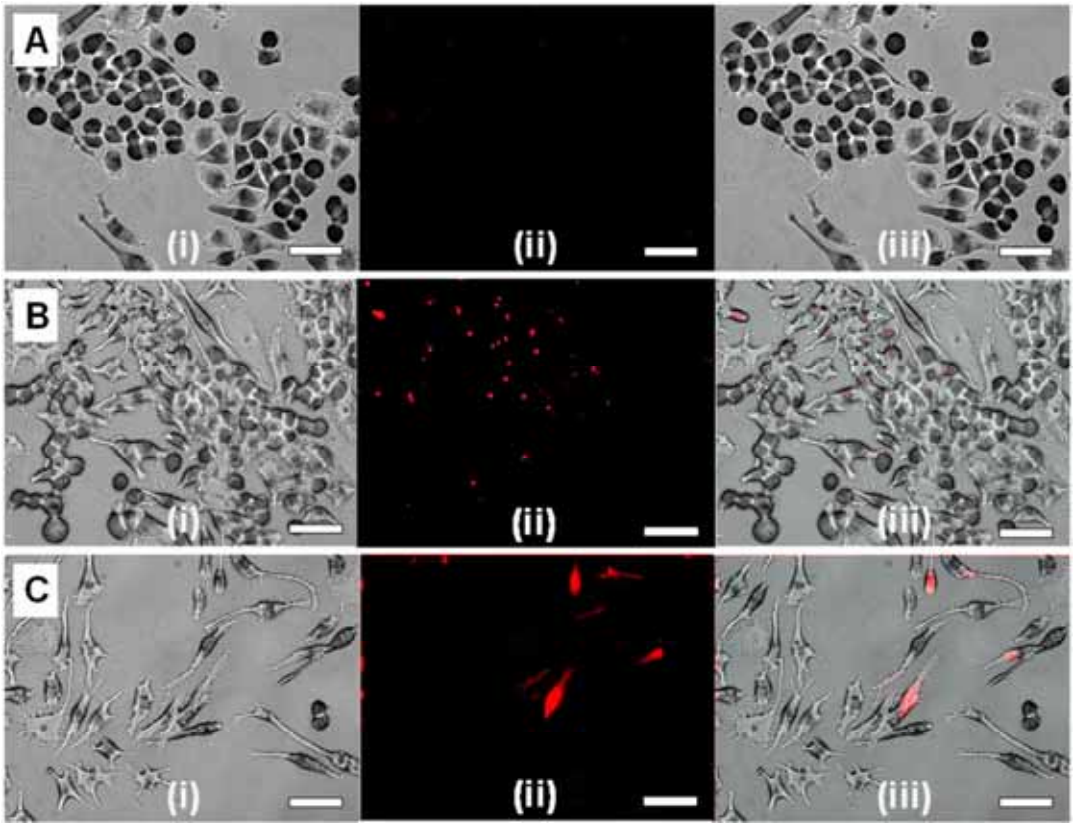

Figure 4.5 Phase (i), fluorescence (ii), and combined (iii) images of RAW 264.7 macrophages incubated (24 h) with red fluorescent (λ_{em}. 640 nm) silicon nanoparticles (<4 nm diam.). A: Control (no SNs present), B: SNs ,20 μg/ml, C: SNs, 200 μg/ml; scale bar: 30 μm.

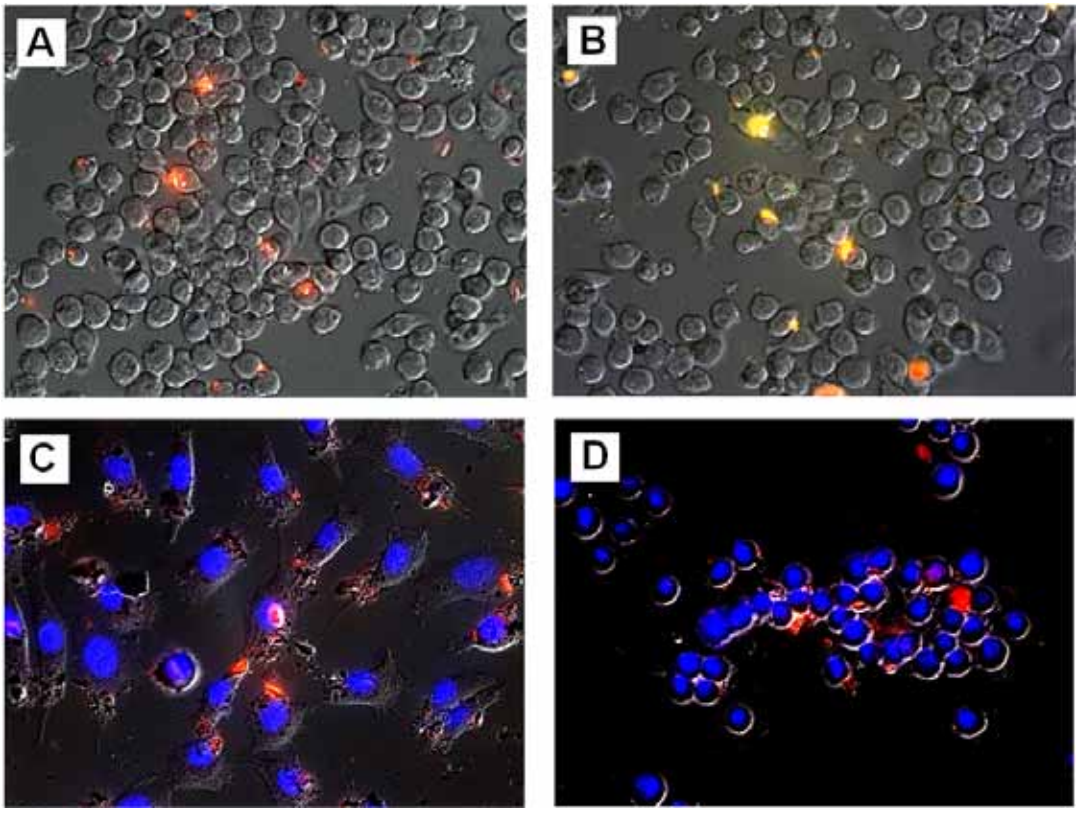

Figure 4.6 Fluorescence images of RAW and L929 Cells with silicon nanoparticles. (A) RAW cells incubated with particles for 24 h, observed with DAPI filter set (~350 nm). (B) RAW cells incubated with particles for 24h, observed with UV filter set (~270 nm). (C) L929 cells incubated with particles for 24h, nucleus stained with DAPI, and observed with DAPI filter set. (D) RAW cells incubated with particles for 1h, nucleus stained with DAPI, and observed with DAPI filter set.

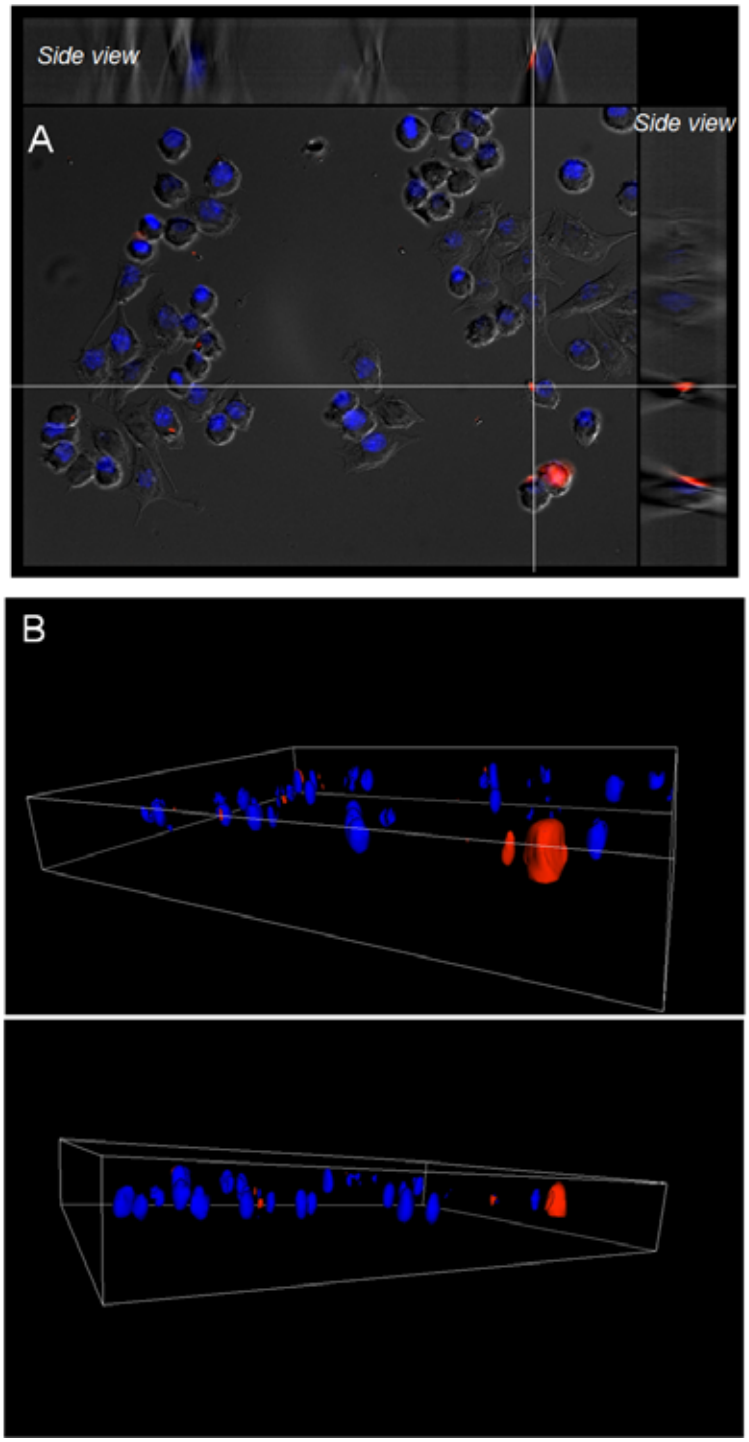

Figure 4.7 Z stack fluorescence image of RAW cells treated with 10 µg/ml Si nanoparticles for 24h. (A) Crossed section (white lines) on the red fluorescence spot is from inside the cell confirmed by side views. (B) 3D rendered images of (A) shows internal association of SNs with RAW cells.

4.4 Discussion

The objective of this study is to determine the cytotoxicity and inflammatory potential of silicon nanoparticles and silicon microparticles using an *in vitro* system (murine macrophages). Several endpoints were studied: cytotoxicity, production of nitric oxide, TNF-α, and IL-6. Si nano and microparticles can be sterilized and depyrogenated in a 300°C furnace. For *in vitro* studies and use in medical applications, it is important that nanoparticles are sterile as well as endotoxin-free.[16] Our results suggested that cytotoxicity of silicon microparticles emerges at a concentration that is about ten times higher compared to nanoparticles. Discussing possible mechanistic cytotoxicity differences between nano- and micro-sized particles, it is important to point out the considerable disparity in the particle size. The average size of the silicon nanoparticle (3 ~ 5 nm) is 100~1000 times smaller than the silicon micro-particles (100~3000 nm). Furthermore, for the same total mass present in a solution, there are at least 10^6 times higher number of nanoparticles than the number of microparticles. Therefore, at an equivalent gram concentration, a sample of nanoparticles contains from 2 to 3 orders of magnitude higher number of particles than a sample of micron-sized particles. Thus, per particle basis, cytotoxicity of silicon nano-particles is significantly lower. Furthermore, compared to II-IV based semiconductor quantum dots, which are widely advertised as bio-tags, the mass of a single silicon nanoparticle is significantly lower. A 3 nm diameter Si nanoparticle weighs ~1×10^4 g·mol^{-1}, while a commonly referenced 3 nm CdSe/ZnS quantum dot weighs ~4.4×10^4 g·mol^{-1} (core only, Evident Technologies, Troy, NY). These

estimates suggest that more Si nanoparticles interact with cells than II-VI semiconductor quantum dots in an equivalent gram concentration sample. Although the safe limit of Si nanoparticle dosages in gram concentration (20 μg/ml) is comparable to II-IV based quantum dots [5], a higher absolute number of nanoparticles available to interact with cells may be essential when using nanoparticles as fluorescent tags for imaging. In this regard, SNs are clearly preferable over binary semiconductor quantum dots.

Inflammatory responses from macrophages treated with SNs and SMs can be compared to the reported inflammatory responses of cells treated with nanoparticles of other materials [13b, 17]. Inoue et al. [17e] studied the effects of two different sized (14 and 56 nm in diameter) carbon nanoparticles on murine lung macrophages sand found that the smaller (d=14 nm) carbon nanoparticles induced more IL-2 and IL-10 compared to the larger (d = 56 nm) particles. Waldman et al. [13b] compared the effect of micro sized (d= ~1 μm) carbon particles with carbon nanoparticles (d = 14 nm) in a TNF-α induction in human macrophage and endothelial cells. They claim that nanoparticles compared to the micro sized particles are more efficient in stimulating cytokine production because of their higher specific surface area. Larger specific surface area contributes to a higher number of surface ions which help produce radicals in the cells. It is well known that reactive radical species generated by nano materials in contact with cells may be a source of cytotoxicity [4, 5d, 5h, 13b, 17c, 17d, 18]. However, nanoparticles in these studies were usually not small enough to enter inside the cell by way of endocytosis. At present, there is no consensus on the role of nanoparticle size in inducing cellular responses, as toxic effects of

nanoparticle size vary extensively among different cell types and nanoparticle materials [18, 13c, 17h]. In addition, we suspect some studies that demonstrate upregulated TNF-α and other cytokines by nanoparticles may have had endotoxin (LPS) contamination.

Rothen-Rutishauser et al. [17h] showed that among polystyrene, titanium oxide and gold nanoparticles, only gold nanoparticles (250 nm) upregulated TNF-α levels from A549 epithelial cells while TiO_2 (300 nm) and polystyrene (780 nm) nanoparticles did not. Our results showed both TNF-α and IL-6 downregulation in murine macrophages exposed to silicon nanoparticles, although gave different results with micrometer sized silicon particles, similar to results of Lucarelli et al. [13c] obtained with cobalt nanoparticles in human macrophage U-937 cells.

Although our cells were alive when exposed up to 20 μg/ml of Si nanoparticles (Fig. 3.3), these particles may have blocked one of the macrophages' functions in particular cytokine response and release. Moreover, because of their small size or atypical method of entry into the macrophage, nanoparticles are not recognized as "foreign" by the macrophages. It is likely that silicon nanoparticles entered the macrophage cell through the pores in the cell membrane, while the microparticles are large enough to be recognized as "foreign" and were phagocytozed. Several reports suggest that small particles are capable of entering the cell through membrane pores [3b, 17 a-b]. Geiser et al. [17a] has studied 780 nm titanium dioxide particle interactions with porcine lung macrophages and found that they could pass through cell membrane by "diffusion or adhesive interactions." Also, 10 nm diameter silver nanoparticles diffused into embryo chorionic space via 0.5 to 0.7 μm diameter chorion pore canals

[17b]. Therefore we cannot exclude the possibility that 3~5 nm diameter Si nanoparticles are internalized by some alternative mechanism besides phagocytosis.

More studies are needed to clarify particle uptake pathways for both nano and microparticles. The engulfment and the final location of the nano and microparticles may be different, and will lead to diverse biological responses by the macrophage cells. It is important to note that in the current study we examined effects of sterile, endotoxin-free nano- and micro-sized particles of the same chemical entity using macrophage cells to elucidate the biological effect of the particle size.

Localization of nanoparticle inside the cell may ultimately determine cells' biological response, whether it is inside along the inner or outer membrane surface or outside of the cell wall [5f, 17 g-h]. Recently, Tsoli et al. [19] studied gold nanoparticles, which ended up in the vicinity of the cell nuclei, and interacted with DNA, leading to pronounced toxicity. Therefore, mechanistic modeling of the nanoparticle cytotoxicity calls for the accurate measurement of the nanoparticle location relative to various cell parts.

In summary, we have shown that 3-5 nm diameter endotoxin free silicon nanoparticles are cytotoxic to RAW 264.7 macrophages, when incubated at concentrations exceeding 20 μg/ml. However, no inflammatory response was detected with silicon nanoparticle incubations up to 200 μg/ml using NO, TNF-alpha, and IL-6 assays. Cells, exposed to silicon micro-particles (d= 100-3000 nm), however, produced increasing amounts of TNF-a, and IL-6 at concentrations up to 100 μg/ml, but showed higher survival percentages. It is apparent that particle size was a decisive factor in determining cytotoxicity as all particles were dry heat sterilized at 300 °C

prior to incubations and attained the similar surface composition. Higher molar concentration and relative surface area as well as the enhanced intracellular access are possible reasons for the higher Si nanoparticle cytotoxicity at equivalent gram concentrations. Remarkably, Si nanoparticles stimulated macrophages to down-regulate cytokines (TNF-a, and IL-6). It is conceivable that macrophages could not identify the nanoparticles as "foreign materials" or apparent cytokine down-regulation was caused by the live cell population drop when incubated at Si nanoparticle concentrations exceeding 20 μg/ml. Fluorescent microscopy images of RAW cells incubated for 24 h with 20 g/ml Si nanoparticles show particles within the cell envelope and suggests that nanoparticles could enter the macrophage by endocytosis through the membrane pores.

4.5 Summary

In the current study, the cytotoxic and inflammatory responses of sterile, endotoxin-free nano- and micro-sized particles of the same chemical entity on macrophages were evaluated. We showed that 3-5 nm diameter endotoxin-free SNs are cytotoxic to RAW 264.7 macrophages, when incubated at concentrations exceeding 20 μg/ml. However, in contrast to SMs, no inflammatory responses, i.e., production of NO, TNF-alpha, and IL-6) were detected with SNs up to 200 μg/ml. Cells, exposed to SMs (100-3000 nm diam.), however, produced increasing amounts of TNF-a, and IL-6 at concentrations up to 100 μg/ml, but showed higher survival rates. It is apparent that particle size was a decisive factor in determining cytotoxicity as all particles were

dry-heat sterilized at 300 °C prior to incubations and attained the similar surface composition. Higher molar concentration and relative surface area as well as the enhanced intracellular access are possible reasons for the higher SN cytotoxicity at equivalent gram concentrations. Remarkably, SNs stimulated macrophages to apparently down-regulate cytokines (TNF-a, and IL-6) production. It is conceivable that macrophages could not identify the nanoparticles as "foreign materials" or apparent cytokine down-regulation was caused by the live cell population drop when incubated at Si nanoparticle concentrations exceeding 20 μg/ml. It is difficult to understand if the above cytotoxic and inflammatory responses were related to intracellular accumulation of SNs since overlay images do not distinguish whether the SNs were internalized or simply adhered to the cell membranes. Therefore, an understanding of the kinetics and intracellular localization of nanoparticles will increase our understanding of the mechanisms of nanoparticle cytotoxicity and other adverse responses.

4.6 Reference

[1] (a) Michalet, X.; Pinaud, F. F.; Bentolila, L. A.; Tsay, J. M.; Doose, S.; Li, J. J.; S undaresan, G.; Wu, A. M.; Gambhir, S. S.; Weiss, S. *Science* **2005**, *307*, 538. (b) Medintz, I. L.; Uyeda, H. T.; Goldman, E. R.; Mattoussi, H. *Nat. Mat.* **2005**, *4*, 43 5. (c) Clarke, S. J.; Hollmann, C. A.; Zhang, Z. J.; Suffern, D.; Bradforth, S. E.; D imitrijevic, N. M.; Minarik, W. G.; Nadeau, J. L. *Nat. Mat.* **2006**, *5*, 409. (d) Cha vanpatil, M. D.; Khdair, A.; Panyam, J. *Pharm. Res.* **2007**, *24*, 803. (e) Savage,

N.; Diallo, M. S. *J. Nano. Res.* **2005**, *7*, 331.

[2] (a) Duan, H. W.; Nie, S. M. *J. Am. Chem. Soc.* **2007**, *129*, 3333. (b) Lovric, J.; Ba zzi, H. S.; Cuie, Y.; Fortin, G. R. A.; Winnik, F. M.; Maysinger, D. *J. Mol. Med.-Jmm* **2005**, *83*, 377. (c) Seleverstov, O.; Zabirnyk, O.; Zscharnack, M.; Bulavina, L.; Nowicki, M.; Heinrich, J. M.; Yezhelyev, M.; Emmrich, F.; O'Regan, R.; Bad er, A. *Nano Lett.* **2006**, *6*, 2826.

[3] (a) Lin, C. A. J.; Liedl, T.; Sperling, R. A.; Fernandez-Arguelles, M. T.; Costa-Fe rnandez, J. M.; Pereiro, R.; Sanz-Medel, A.; Chang, W. H.; Parak, W. J. *J. Mat. C hem.* **2007**, *17*, 1343. (b) Smith, A. M.; Ruan, G.; Rhyner, M. N.; Nie, S. M. *Ann. Bio. Eng.* **2006**, *34*, 3.

[4] (a) Lewinski, N.; Colvin, V.; Drezek, R. *Small* **2007**, *3*, 2. (b) Hardman, R. *Env. Heal. Persp.* **2006**, *114*, 165. (c) Klostranec, J. M.; Chan, W. C. *Adv. Mat.* **2006**, *18*, 1953.

[5] (a) Derfus, A. M.; Chan, W. C. W.; Bhatia, S. N. *Nano Lett.* **2004**, *4*, 11. (b) Fisc her, H. C.; Liu, L. C.; Pang, K. S.; Chan, W. C. W. *Adv. Func. Mat.* **2006**, *16*, 129 9. (c) Panessa-Warren, B. J.; Warren, J. B.; Wong, S. S.; Misewich, J. A. *J. Phys. Con. Mat.* **2006**, *18*, s2185. (d) Tsay, J. M.; Michalet, X. *Chem. & Bio.* **2005**, *12*, 1159. (e) Zhang, T. T.; Stilwell, J. L.; Gerion, D.; Ding, L. H.; Elboudwarej, O.; Cooke, P. A.; Gray, J. W.; Alivisatos, A. P.; Chen, F. F. *Nano Lett.* **2006**, *6*, 800. (f) Kirchner, C.; Liedl, T.; Kudera, S.; Pellegrino, T.; Javier, A. M.; Gaub, H. E.; Stolzle, S.; Fertig, N.; Parak, W. J. *Nano Lett.* **2005**, *5*, 331. (g) Lin, W. S.; Huang, Y. W.; Zhou, X. D.; Ma, Y. F. *Toxic. Appl. Pharm.* **2006**, *217*, 252. (h) Hoshino, A.; Fujioka, K.; Oku, T.; Suga, M.; Sasaki, Y. F.; Ohta, T.; Yasuhara, M.; Suzuki,

K.; Yamamoto, K. *Nano Lett.* **2004**, *4*, 2163. (i) Gupta, A. K.; Gupta, M. *Biomat erials* **2005**, *26*, 1565. (j) Pan, Y.; Neuss, S.; Leifert, A.; Fischler, M.; Wen, F.; Si mon, U.; Schmid, G.; Brandau, W.; Jahnen-Dechent, W. *Small* **2007**, *3*, 1941.

[6] Cullis, A. G.; Canham, L. T.; Calcott, P. D. J. *Appl. Phys. Rev.* **1997**, *82*, 910.

[7] (a) Wang, L.; Reipa, V.; Blasic, J. *Bioconjugate Chem*. **2004**, *15*, 409. (b) Ding, Z.; Quinn, M. B.; Haram, A. K.; Pell, L. E.; Korgel, B. A.; Bard, A. L. *Science* **20 02**, *296*, 1293. (c) Yamani, Z.; Ashhab, S.; Nayfeh, A.; Thompson, W. H.; Nayfe h, M. *J. Appl. Phys*. **1998**, *83*, 3929. (d) Choi, J.; Wang, N. S.; Reipa, V. *Langmui r* **2007**, *23*, 3388. (e) Choi, J.; Niarhos, P.; Wang, N.S.; Reipa, V. *Proc. SPIE* **200 7**, *6645*, 664523. (f) Choi, J.; Zhang, Q.; Hitchins, V.M.; Wang, N.S.; Reipa, V. *P roc. SPIE* **2007,** *6645*, 66451Q.

[8] Jung, K. H.; Shih, S.; Hsieh, T. Y.; Kwong, D. L.; Lin T. L. *Appl. Phys. Lett.* **199 1**, *59*, 3264.

[9] Buriak, J.M. *Chem. Rev.* **2002**, *102*, 1271.

[10](a) Chapekar, M.S.; Zaremba, T.G.; Kuester, R.K.; Hitchins, V.M. *J. Biomed. Ma ter. Res.* **1996**, *31*, 251. (b) Mitchell, L.A.; Gao, J.;Vander Wal, R.; Gigliotti, A.; Burchiel, S.W.; McDonald, J.D. *Toxicol. Sci.* **2007**, *100*, 203. (c) Brown, D.M.; K inloch, I.A.; Bangert, U.; Windle, A.H.; Walter, D.M.; Walker, G.S.; Scotchford, C.A.; Donaldson, K.; Stone, V. *Carbon* **2007**, *45*, 1743.

[11](a) Okazaki, Y.; Katayama, Y.; Takarabe, K.; Doi, K.; Rikitake, K.; Ohtsubo, S.; Hamada, M.; Naito, K.; Natsuaki, M.; Itoh, T. *ASAIO J.* **2000**, *46*, 202. (b) Ainsli e, K.M.; Bachelder, E.M.; Borkar, S.; Zahr, A.S.; Sen, A.; Badding, J.V.; Pishko, M.V. *Langmuir* **2007,** *23*, 747.

[12]Blanchard, C.R. *Tech. today* **1995**, *Fall*, 1.

[13](a) Kim, S.B.; Ozawa, T.; Tao, H.; Umezawa, Y. *Anal. Biochem.* **2007**, *362*, 148. (b) Waldman, W.J.; Kristovich, R.; Knight, D.A.; Dutta, P.K. *Chem. Res. Toxicol.* **2007**, *20*, 1149. (c) Lucarelli, M.; Gatti, A.M.; Savarino, G.; Quattroni, P.; Marti nelli, L.; Monari, E.; Boraschi, D. *Eur. Cytokine Net.*,**2004**, *15*, 339.

[14]"Standard practice for testing for biological responses to particles in vitro." *ASTM F1903-98* (reapproved **2003**). ASTM, Intl., West Conshohocken, PA.

[15]Moshage, H. *Clin. Chem.* **1997**, *43*, 553.

[16](a) Hitchins, V.M.; Merritt, K. *J. Biomed. Mater. Res.* **1999**, *46*, 434. (b) Vallhov, H.; Qin, J.; Johansson, S.M.; Ahlborg, N.; Muhammed, M.A.; Scheynius, A.; Ga brielsson, S. *Nano Letters* **2006**, *6*, 1682.

[17](a) Geiser, M.; Rothen-Rutishauser, B.; Kapp, N.; Schürch, S.; Kreyling, W.; Sch ulz, H.; Semmler, M.; Im Hof, V.; Heyder, J.; Gehr, P. *Env. Heal.Persp.* **2005**, *11 3*, 1555. (b) Lee, K.J.; Nallathamby, P.D.; Browning, L.M.; Osgood, C.J.; Xu, X. N. *ACS NANO* **2007**, *1*, 113. (c) Brown, D.M.; Donaldson, K.; Borm, P.J.; Schins, R.P.; Dehnhardt, M.; Gilmour, P.; Jimenez, L.A.; Stone, V. *Am. J. Physiol.* **2004**, *286*, L344. (d) Dick, C.A.; Brown, D.M.; Donaldson, K.; Stone, V. *Inhalation To xicol.* **2003**, *15*, 39. (e) Inoue, K.; Takano, H.; Yanagisawa, R.; Ichinose, T.; Saku rai, M.; Yoshikawa, T. *Arch. Toxicol.* **2006**, *80*, 614. (f) Papageorgioua, I,; Brown, C.; Schins, R.; Singh, S.; Newson, R.; Davis, S.; Fisher, J.; Ingham, E.; Case, C. P. *Biomaterials* **2007**, *28*, 2946. (g) Tamura, K.; Takashi, N.; Akasaka, T.; Roska, I.D.; Uo, M.; Totsuka, Y.; Watari, F. *Key Eng. Mat.* **2004**, *254-256*, 919. (h) Rot hen-Rutishauser, B.; Mühlfeld, C.; Blank, F.; Musso, C.; Gehr, P. *Par. Fib. Toxic*

o. **2007**, *4*, 1.

[18]Sayes, C.M.; Wahi, R.; Kurian, P.A.; Liu, Y.; West, J.L.; Ausman, K.D.; Warheit, D.B.; Colvin, V.L. *Toxicol. Sci.* **2006**, *92*, 174.

[19]Tsoli, M.; Kuhn, H.; Brandau, W.; Esche, H.; Schmid, G. *Small* **2005**, *8–9*, 841.

Chapter 5: Conclusion and Perspectives

5.1 Conclusions

5.1.1 Electrochemical reduction synthesis of photoluminescent silicon nanocrystals

Single nanometer range photoluminescent silicon nanocrystals were prepared at room temperature and ambient pressure using a direct electrochemical reduction of octyltrichlorosilane from the non-aqueous electrolyte. Resulting octane termination provides a stable passivation and could serve as a platform for further particle functionalization. A simple and scalable procedure potentially could address the requirement for stable ultrasmall Si nanocrystals in optoelectronic, photovoltanics and bioassay industries.

5.1.2 Protein conjugation of silicon nanocrystals

We have covalently coupled streptavidin with the photoluminescent silicon nanoparticles using a multistep photo-assisted reaction and a bifunctional cross-linker. The characteristic blue nanoparticle photoluminescence was retained in the silicon quantum dot-protein complex. Faster elution of the nanoparticle-streptavidin complex in the native gel electrophoresis indicates extra negative charge of the conjugate due to linked silicon nanoparticles. Typically from 4 to 5 silicon nanoparticles are bound to streptavidin molecule as determined from the capillary electrophoresis analysis. Streptavidin molecules retain their binding capability to the biotin subsequent to the

conjugation protocol. Covalent attachment of small, efficient and non-toxic photoluminescent silicon quantum dots to streptavidin provides a convenient pathway for biomolecules labeling in biotin-streptavidin affinity based assays.

5.1.3 Cytotoxicity and inflammatory response of silicon nanocrystals

The cytotoxic and inflammatory responses of sterile, endotoxin-free nano- and micro-sized particles of the same chemical entity on macrophages were evaluated. We showed that 3-5 nm diameter endotoxin-free SNs are cytotoxic to RAW 264.7 macrophages, when incubated at concentrations exceeding 20 μg/ml. However, in contrast to SMs, no inflammatory responses, i.e., production of NO, TNF-alpha, and IL-6) were detected with SNs up to 200 μg/ml. Cells, exposed to SMs (100-3000 nm diam.), however, produced increasing amounts of TNF-a, and IL-6 at concentrations up to 100 μg/ml, but showed higher survival rates. It is apparent that particle size was a decisive factor in determining cytotoxicity as all particles were dry-heat sterilized at 300 °C prior to incubations and attained the similar surface composition. Higher molar concentration and relative surface area as well as the enhanced intracellular access are possible reasons for the higher SN cytotoxicity at equivalent gram concentrations. Remarkably, SNs stimulated macrophages to apparently down-regulate cytokines (TNF-a, and IL-6) production. It is conceivable that macrophages could not identify the nanoparticles as “foreign materials” or apparent cytokine down-regulation was caused by the live cell population drop when incubated at Si nanoparticle concentrations exceeding 20 μg/ml. It is difficult to understand if the above cytotoxic and inflammatory responses were related to intracellular

accumulation of SNs since overlay images do not distinguish whether the SNs were internalized or simply adhered to the cell membranes. Therefore, an understanding of the kinetics and intracellular localization of nanoparticles will increase our understanding of the mechanisms of nanoparticle cytotoxicity and other adverse responses.

5.2 Perspectives

5.2.1 Large scale, efficient synthesis of silicon nanocrystals

Since silicon nanoparticles have been utilized many areas of study, large scale synthesis is may be worth pursuing industrial applications. Current electrochemical synthesis method may be developed to produce large amount of silicon nanoparticles with well defined surface and crystalline structures. In order to achieve it, the electrochemical cell design may be updated with better sealing of inside chemicals. Purification steps may be modified to enhance purity and organic residue free surface of nanoparticles.

5.2.2 Biomolecule tagging of silicon nanocrystals

Biotagging with Si nanocrystals which have different fluorescent colors may be studied to resolve the issue of using blue Si nanocrystals which can interfere with autofluorescence from the biomolecules. Surface termination with oxide, carboxylic acid or amines can provide water solubility as well as Si core protection. Oxide

terminated Si nanoparticle surface can be further functionalized with various crosslinkers including well established silane chemistry.

Proteins as well as DNA may be tagged by surface functionalized Si nanoparticles. Tagged single strand DNA can be designed to react with a complementary strand DNA resulting a selective fluorescent biotagging to a desired DNA strand.

5.2.3 Study on the cytotoxic mechanism of silicon nanocrystals

Cytotoxic mechanism may be investigated. Macrophages' reactive oxygen species activation may be monitored and analyzed with and without nanoparticles. Assay for apoptosis and necrosis may be implemented to study if programmed cell death or sudden cell death is majority of dying cells. If the programmed death is surpassing, the signal pathways for apoptosis in the cell may be investigated to find out which signal proteins were activated by nanoparticles. In order to confirm nanoparticles localization inside the cell, electron microscopy may be used to measure Si nanoparticle content in the sectioned cells.

Bibliography

Aihara, S.; Ishii, R.; Fukuhara, M.; Kamata, N.; Terunuma, D.; Hirano, Y.; Saito, N.; Aramata, M.; Kashimura, S. Electroreductive synthesis and optical characterization of silicon nanoparticles. *J. Non-cryst. Solids* **2001**, *296*, 135-138.

Ainslie, K. M.; Bachelder, E. M.; Borkar, S.; Zahr, A. S.; Sen, A.; Badding, J. V.; Pishko, M. V. Albumin adsorption and cell adhesion on nanofibrous polytetrafluoroethylene (nPTFE). *Langmuir* **2007**, *23*, 747-754.

Alivisatos, P. The use of nanocrystals in biological detection. *Nat. Biotechnol.* **2004**, *722*, 47-52.

Baldwin, R. K.; Pettigrew, K. A.; Garno, J. C.; Power, P. P.; Liu, G.; Kauzlarich, S. M. Room Temperature Solution Synthesis of Alkyl-Capped Tetrahedral Shaped Silicon Nanocrystals. *J. Am. Chem. Soc.* **2002**, *124*, 1150-1151.

Bäumle, M.; Stamou, D.; Segura, J.; Hovius, R.; Vogel, H. Highly fluorescent streptavidin-coated CdSe nanoparticles: Preparation in water, characterization, and micropatterning. *Langmuir* **2004**, *20*, 3828-3831.

Belomoin, G.; Therrien, J.; Smith, A.; Rao, S.; Twesten, R.; Chaieb, S.; Nayfeh, M. H.; Wagner, L.; Mitas, L. Observation of a magic discrete family of ultrabright Si nanoparticles. *Appl. Phys. Lett.* **2002**, *80*, 841-843.

Bianconi, P. A.; Weidman, T. W. Poly(n-hexylsilyne): synthesis and properties of the first alkyl silicon $[RSi]_n$ network polymer. *J. Am. Chem. Soc.* **1988**, *110*, 2342-2344.

Blanchard, R. Biomaterials: Body parts of the future. *Tech. today* **1995**, *Fall*, 1. (http://www.swri.org/3pubs/ttoday/fall/implant.htm).

Bottini, M.; Cerignoli, F.; Dawson, M. I.; Magrini, A., Rosato, N., and Mustelin, T. Full-length single-walled carbon nanotubes decorated with streptavidin-conjugated quantum dots as multivalent intracellular fluorescent nanoprobes. *Biomacromolecules* **2006**, *7*, 2259-2263.

Bradley, K.; Briman, M.; Star, A.; Gruner, G. Charge transfer from adsorbed proteins. *Nano Lett.* **2004**, *4*, 253-256.

Brown, D. M.; Donaldson, K.; Borm, P. J.; Schins, R. P.; Dehnhardt, M.; Gilmour, P.; Jimenez, L. A.; Stone, V. Calcium and ROS-mediated activation of transcription factors and TNF-α cytokine gene expression in macrophages exposed to ultrafine particles. *Am. J. Physiol.* **2004**, *286,* L344-L353.

Brown, D. M.; Kinloch, I. A.; Bangert, U.; Windle, A. H.; Walter, D. M.; Walker, G. S.; Scotchford, C. A.; Donaldson, K.; Stone, V. An in vitro study of the potential of carbon nanotubes and nanofibres to induce inflammation mediators and frustrated phagocytosis. *Carbon.* **2007**, *45*, 1743-1756.

Buriak, J.M. Organometallic chemistry on silicon and germanium surfaces. Chem. Rev. **2002**, *102*, 1271-1308.

Canham, L. T. Silicon quantum wire array fabrication by electrochemical and chemical dissolution of wafers. *Appl. Phys. Lett.* **1990**, *57*, 1046-1048.

Carlisle, J. A.; Dongol, M.; Germanenko, I. N.; Pithawalla, Y. B.; El-Shall, M. S. *Chem. Phys. Lett.* **2000**, *326*, 335-340.

Chapekar MD, Zaremba TG, Kuester RK, Hitchins VM. 1996. Synergistic induction of tumor necrosis factor-α by bacterial lipopolysaccharide and lipoteichoic acid in combination with polytetrafluoroethylene particles in a murine macrophage cell line RAW 264.7. *J. Biomed. Materials Res.* **31:** 251-256.

Chavanpatil MD, Khdair A, Panyam J. 2007. Surfactant-polymer nanoparticles: A novel platform for sustained and enhanced cellular delivery of water-soluble molecules. *Pharm. Res.* **24:** 803-810.

Choi J, Tung S, Wang NS, Reipa V. 2008a. Small-angle neutron scattering measurement of silicon nanoparticle size. *Nanotechnology.* **19:** 0857151-0857158.

Choi J, Wang NS, Reipa V. 2007. Photoassisted tuning of silicon nanocrystal photoluminescence. *Langmuir.* **23:** 3388-3394.

Choi J., Wang NS, Reipa V. 2008b. Conjugation of the photoluminescent silicon nanoparticles to streptavidin. *Bioconjugate Chem.* **19:** 680-685.

Clarke, S. J., Hollmann, C. A., Zhang, Z., Suffern, D., Bradforth, S. E., Dimitrijevic, N. M., Minarik, W. G., and Nadeau, J. L. (2006) Photophysics of dopamine-modified quantum dots and effects on biological systems. Nat. Mat. 5, 409-417.

Cullis AG, Canham LT, Calcott PD. 1997. The structural and luminescence properties of porous silicon. *J. Appl. Phys.* **82:** 909-965.

Derfus AM, Chan WCW, Bhatia SN. 2004. Probing the cytotoxicity of semiconductor quantum dots. *Nano Lett.* **4:** 11-18.

Dick CA, Brown DM, Donaldson K, Stone V. 2003. The role of free radicals in the toxic and inflammatory effects of four different ultrafine particle types. *Inhalation Toxicol.* **15:** 39-52.

Ding, Z., Quinn, M. B., Haram, A. K., Pell, L. E., Korgel, B. A., and Bard, A. L. (2002) Electrochemistry and electrogenerated chemiluminescence from silicon nanocrystal quantum dots. Science 296, 1293-1297.

Duan HW, Nie SM. 2007. Cell-penetrating quantum dots based on multivalent and endosome-disrupting surface coatings. *J. Am. Chem. Soc.***129:** 3333-3338.

Eckhoff, D. A., Stuart, J. N., Sutin, J. D. B., Sweedler, J. V., and Gratton, E. (2006) Capillary electrophoresis of ultrasmall carboxylate functionalized silicon nanoparticles. J. Chem. Phys. 125, 0811031-0811034.

Fischer, H. C., Liu, L. C., Pang, K. S., and Chan, W. C. W. (2006) Pharmacokinetics of nanoscale quantum dots: In vivo distribution, sequestration, and clearance in the rat. Adv. Func. Mat. 16, 1299-1305.

Gao, X, Cui, Y., Levenson, R. M., Chung, L. W. K., and Nie, S. (2004) In vivo cancer targeting and imaging with semiconductor quantum dots. Nat. Biotechnol. 22, 969-977.

Geiser M, Rothen-Rutishauser B, Kapp N, Schürch S, Kreyling W, Schulz H, Semmler M, Im Hof V, Heyder J, Gehr P. 2005. Ultrafine particles cross cellular membranes by nonphagocytic mechanisms in lungs and in cultured cells. *Env. Health. Persp.* **113:** 1555-1560.

Goering PL, Kuester RK, Neale AR, Chapekar MS, Zaremba TG, Gordon EA, Hitchins VM. 2000. Effects of particulate and soluble cadmium species on biochemical and functional parameters in cultured murine macrophages. *In Vitro & Mol. Toxicol.* **13**: 125-136.

Guo, W., Li, J. J., Wang, Y. A., and Peng, X. (2003) Conjugation chemistry and bioapplications of semiconductor box nanocrystals prepared via dendrimer bridging. Chem. Mater. 15, 3125-3133.

Gupta AK, Gupta M. 2005. Cytotoxicity suppression and cellular uptake enhancement of surface modified magnetic nanoparticles. *Biomaterials.* **26:** 1565-1573.

Hardman R. 2006. A toxicologic review of quantum dots: Toxicity depends on physicochemical and environmental factors. *Env. Heath Persp.* **114:** 165-172.

Heath, J. R. *Science* 1992, **258**, 1131-1133.

Hengge, E.; Firgoi, H. *J. Organomet. Chem.* **1981**, *212*, 155-161.

Hengge, E.; Litscher, G. *Angew. Chem.* **1976**, *88*, 414-414.

Hitchins VM, Neale AR, Merritt K. 1999. Induction of TNF-alpha, IL-6 and nitric oxide by LPS in combination with Al_2O_3 and with polystyrene in RAW 264.7 murine macrophages. Trans. Soc. Biomaterial. 22: 128.

Hitchins VM, Merritt K. 1999. Decontaminating particles exposed to bacterial endotoxin (LPS). *J. Biomed. Mater. Res.* **46:** 434-437.

Hua, F.J., Erogbogbo, F., Swihart, M.T., and Ruckenstein, E. (2006) Organically capped silicon nanoparticles with blue photoluminescence prepared by hydrosilylation followed by oxidation. Langmuir 22, 4363-4370.

Huang, X., Weng, J., Sang, F., Song, X., Cao, C., and Ren, J. (2006) Characterization of quantum dot bioconjugates by capillary electrophoresis with laser-induced fluorescent detection. J. Chrom. A. 1113, 251-254.

Inoue K, Takano H, Yanagisawa R, Ichinose T, Sakurai M, Yoshikawa T. 2006. Effects of nano particles on cytokine expression in murine lung in the absence or presence of allergen. *Arch. Toxicol.* **80:** 614-619.

Ishifune, M.; Kashimura, S.; Kogai, Y.; Fukuhara, Y.; Kato, T.; Bu, H.; Yamashita, N.; Murai, Y.; Murase, H.; Nishida, R. *J. Organomet. Chem.* **2000**, *611*, 26-31.

Jung, K. H., Shih, S., Hsieh, T. Y., Kwong, D. L., and Lin T. L. (1991) Intense photoluminescence from laterally anodized porous Si. Appl. Phys. Lett. 59, 3264-3266.

Kirchner, C., Liedl, T., Kudera, S., Pellegrino, T., Javier, A. M., Gaub, H. E., Stolzle, S., Fertig, N., and Parak, W. J. (2005) Cytotoxicity of colloidal CdSe and CdSe/ZnS nanoparticles. Nano Lett. 5, 331-338.

Klostranec JM, Chan WCW. 2006. Quantum dots in biological and biomedical research: recent progress and present challenges. *Adv. Mat.* **18:** 1953-1964.

Kogai, Y.; Ishifune, M.; Uchida, K.; Kashimura, S. *Electrochemistry* **2005**, 73, 419-423.

Lee KJ, Nallathamby PD, Browning LM, Osgood CJ, Xu XN. 2007. In vivo imaging of transport and biocompatibility of single silver nanoparticles in early development of zebrafish embryos. *ACS NANO* **1:** 133-143.

Lewinski N, Colvin V, Drezek R. 2008. Cytotoxicity of nanoparticles. *Small* **4**, 26-49.

Lin WS, Huang YW, Zhou XD, Ma YF. 2006. In vitro toxicity of silica nanoparticles in human lung cancer cells. *Toxic. Appl. Pharm.* **217:** 252-259.

Lin CAJ, Liedl T, Sperling RA, Fernandez-Arguelles MT, Costa-Fernandez JM, Pereiro R, Sanz-Medel A, Chang WH, Parak WJ. 2007. Bioanalytics and biolabeling with semiconductor nanoparticles (quantum dots). *J. Mat. Chem.* **17:** 1343-1346.

Lockwood, D. J. *Light emission in silicon from physics to devices*; Academic Press: San Diego, CA, **1998**; p. 253-284.

Lucarelli M, Gatti AM, Savarino G, Quattroni P, Martinelli L, Monari E, Boraschi D. 2004. Innate defense functions of macrophages can be biased by nano-sized ceramic and metallic particles. *Eur. Cytokine Netw.* **15:** 339-346.

Mangolini, L.; Thimsen, E.; Kortshagen, U. *Nano Lett.* **2005**, *5*, 655-659.

Medintz, I. L., Uyeda, H. T., Goldman, E. R., and Mattoussi, H. (2005) Quantum dot bioconjugates for imaging, labelling and sensing. Nat. Mat. 4, 435-446.

Michalet X, Pinaud FF, Bentolila LA, Tsay JM, Doose S, Li JJ, Sundaresan G, Wu, Gambhir SS, Weiss S. 2005. Quantum dots for live cells and in vivo imaging, diagnostics and beyond. *Science.* **307:** 538-544.

Miller, R. D.; Michl, J. *Chem. Rev.* **1989**, *89*, 1359-1410.

Mitchell LA, Gao J, Vander Wal R, Gigliotti A, Burchiel SW, McDonald JD. 2007. Pulmonary and systemic immune response to inhaled multiwalled carbon nanotubes. *Toxicol. Sci.* **100**: 203-214.

Moshage H. 1997. Nitric oxide determinations: Much ado about NO•-thing? *Clin. Chem.* **43:** 553-556.

Nishimura, Y.; Fukunaka Y. *Electrochim. Acta.* **2007**, *53*, 111-116.

O'Farrell, N.; Houlton, A.; Horrocks, B. R. *Int. J. Nanomedicine*. **2006**, *1*, 451-472.

Brus, L. *Adv. Mater.* **1993**, *5*, 286-288.

Okazaki Y, Katayama Y, Takarabe K, Doi K, Rikitake K, Ohtsubo S, Hamada M, Naito K, Natsuaki M, Itoh T. 2000. Torn polytetrafluoroethylene suture used as artificial mitral chordate tendinae. *ASAIO J.* **46:** 202.

Pan Y, Neuss S, Leifert A, Fischler M, Wen F, Simon U, Schmid G, Brandau W, Jahnen-Dechent W. 2007. Size dependent cytotoxicity of gold nanoparticles. *Small* **3:** 1941-1949.

Pathak, S., Choi, S., Arnheim, N., and Thompson, M. E. (2001) Hydroxylated quantum dots as luminescent probes for in situ hybridization. J. Am. Chem. Soc. 123, 4103-4104.

Pawlenko, S. *Organosilicon Chemistry*; de Gruyter: New York, NY, **1986**; p 8.

Pellegrino, T., Manna, L., Kudera, S., Liedl, T., Koktysh, D., Rogach, A. L., Keller, S., Radler, J., Natile, G., and Parak, W. J. (2004) Hydrophobic nanocrystals coated with an amphiphilic polymer shell: A general route to water soluble nanocrystals. Nano Lett. 4, 703-707.

Rodriguez, M. A., and Armstrong, D. W. (2004) Separation and analysis of colloidal/nano-particles including microorganisms by capillary electrophoresis: a fundamental review. J. Chrom. B. 800, 7-25.

Rothen-Rutishauser B, Mühlfeld C, Blank F, Musso C, Gehr P. 2007. Translocation of particles and inflammatory responses after exposure to fine particles and nanoparticles in an epithelial airway model. *Part. Fibre Toxico*. **4:** 1-14.

Sato, S., and Swihart, M. T., (2006) Propionic-acid-terminated silicon nanoparticles: Synthesis and optical characterization. Chem. Mater. 18, 4083-4088.

Savage N, Diallo MS. 2005. Nanomaterials and water purification: Opportunities and challenges. *J. Nano. Res.* **7:** 331-342.

Sayes CM, Wahi R, Kurian PA, Liu Y, West JL, Ausman KD, Warheit DB, Colvin VL. 2006. Correlating nanoscale titania structure with toxicity: A cytotoxicity and inflammatory response study with human dermal fibroblasts and human lung epithelial cells. *Toxicol. Sci.* **92:** 174-185.

Shono, T.; Kashimura, S.; Ishifune, M.; Nishida, R. *J. Chem. Soc. Chem. Commu.* **1990**, 1160-1161.

Skebo JE, Grabinski CM, Schrand AM, Schlager JJ, Hussain SM. 2007. Assessment of metal nanoparticle agglomeration, uptake, and interaction using high-illuminating system. *Intl. J. Toxicol.* **26**: 135-141.

Smith AM, Ruan G, Rhyner MN, Nie SM. 2006. Engineering luminescent quantum dots for in vivo molecular and cellular imaging. *Ann. Biomed. Eng.* **34:** 3-14.

Sperry, J. B.; Wright, D. L. *Chem. Soc. Rev.* **2006**, *35*, 605-621.

Stupca, M.; Alsalhi, M.; Al Saud, T.; Almuhanna, A.; Nayfeh, M. H. *Applied Physics Letters* **2007**, *91*, 0631071-0631073.

Tamura K, Takashi N, Akasaka T, Roska ID, Uo M, Totsuka Y, Watari F. 2004. Effects of micro/nano particle size on cell function and morphology. *Key Eng. Mat.* **254-256:** 919-922.

Tsay, J. M., and Michalet, X., (2005) New light on quantum dot cytotoxicity. Chem. & Bio. 12, 1159-1161.

Tsoli M, Kuhn H, Brandau W, Esche H, Schmid G. 2005. Cellular uptake and toxicity of AU(55) clusters. *Small.* **8-9:** 841-844.

Vallhov H, Qin J, Johansson SM, Ahlborg N, Muhammed MA, Scheynius A, Gabrielsson S. 2006. The importance of an endotoxin-free environment during the production of nanoparticles used in medical applications. *Nano Lett.* **6:** 1682-1686.

van Oss, C. J., Giese, R. F., Bronson, P. M., Docoslis, A., Edwards, P., and Ruyechan, W. T. (2003) Macroscopic-scale surface properties of streptavidin and their influence on aspecific interactions between streptavidin and dissolved biopolymers. Colloids Surf., B 30, 25-36.

Vrček, V.; Slaoui, A.; Muller, J.C. *Thin Solid Films* **2004**, *384*, 451-452.

Waldman WJ, Kristovich R, Knight DA, Dutta PK. 2007. Inflammatory properties of iron-containing carbon nanoparticles. *Chem. Res. Toxicol.* **20:** 1149-1154.

Wang, L., Reipa, V., and Blasic, J. (2004) Silicon nanoparticles as a luminescent label to DNA. Bioconjugate Chem. 15, 409-412.

Warner J. H., Hoshino, A., Yamamoto, K., and Tilley, R. D. (2005) Water-soluble photoluminescent silicon quantum dots. Angew. Chem. Int. Ed. 44, 4550-4554.

Warner J. H., Hoshino, A., Shiohara, A., Yamamoto, K., and Tilley, R. D. (2006) The Synthesis of silicon and germanium quantum dots for biomedical applications. Proc. of SPIE 6069, 6096071-6096078.

Wilcoxon, J. P.; Samara, G. A.; Provencio, P. N. *Phys. Rev. B.* **1999**, 60, 2704-2714.

Wolcott, A., Gerion, D., Visconte, M., Sun, J., Schwartzberg, A., Chen, S., and Zhang, J. Z. (2006) Silica-coated CdTe quantum dots functionalized with thiols for bioconjugation to IgG proteins. J. Phys. Chem. B 110, 5779-5789.

Wu, S., Zhao, X., Zhang, Z., Xie, H., Tian, Z., Peng, J., Lu, Z., Pang, D., and Xie, Z. (2006) Quantum-dot labeled DNA probes for fluorescence in situ hybridization (FISH) in the microorganism Escherichia coli. ChemPhysChem 7, 1062-1067.

Yamani Z, Ashhab S, Nayfeh A, Thompson WH, Nayfeh M. 1998. Red to green rainbow photoluminescence from unoxidized silicon nanocrystallites. *J. Appl. Phys*. **83:** 3929-3931.

Yu, C., Su, C., and Tseng, W. (2006) Separation of acidic and basic proteins by nanoparticle-filled capillary electrophoresis. Anal. Chem. 78, 8004-8010.

Zou, J.; Baldwin, R. K.; Pettigrew, K. A.; Kauzlarich, S.M. *Nano Lett.* **2004**, *4*, 1181-1186.